

(NASA-CR-134039) NONEQUILIBRIUM CHEMISTRY
BOUNDARY LAYER INTEGRAL METHOD PROCEDURE
Final Report (Acurex Corp., Mountain
View, Calif.) 165 p HC \$10.25 CSCL 20M

N73-31835

Unclas
G3/33 14063



**ACUREX
Corporation**

Aerotherm Project 6099

July 1973

Aerotherm Final Report No. 73-67

NONEQUILIBRIUM CHEMISTRY
BOUNDARY LAYER INTEGRAL
MATRIX PROCEDURE

by

Henry Tong
Alfred Buckingham
Howard L. Morse

Prepared for

National Aeronautics and Space Administration
Johnson Space Center
Houston, Texas
Structures and Mechanics Division
Donald W. Curry

Extension to Contract NAS9-9494

FORWARD

This report was prepared by the Aerotherm Division of Acurex Corporation for the NASA Johnson Spacecraft Center under an extension to NASA contract NAS 9-9494. The codes and computational procedures described in this report were developed by the authors with technical support from Dr. R. M. Kendall, Mr. E. P. Bartlett, Mr. W. E. Nicolet and Mr. M. J. Abbett.

The developmental effort described in this report was performed for the NASA Structures and Mechanics Division with Dr. Donald M. Curry as Technical Monitor.

ABSTRACT

This report describes the development of an analytic procedure for the calculation of nonequilibrium boundary layer flows over surfaces of arbitrary catalycities. An existing equilibrium boundary layer integral matrix code was extended to include nonequilibrium chemistry while retaining all of the general boundary condition features built into the original code. For particular application to the pitch-plane of shuttle type vehicles an approximate procedure was developed to estimate the nonequilibrium and nonisentropic state at the edge of the boundary layer.

The nonequilibrium code (BLIMP/KINET) was used to calculate catalycities of typical shuttle thermal protection materials which were exposed to an arc jet environment. Sufficient data was available to predict the simultaneous catalytic efficiencies for atomic oxygen and atomic nitrogen recombination. These catalycities and appropriate nonequilibrium edge conditions were used to predict the boundary layer behavior on the pitch-plane of a typical shuttle vehicle over a trajectory range which included both laminar and turbulent flows. These calculations show a small reduction in heat transfer when compared to catalytic surfaces; however, substantial reductions are demonstrated for noncatalytic surfaces. These calculations also demonstrate the significance of including entropy layer effects.

TABLE OF CONTENTS

<u>Section</u>		<u>Page</u>
1	INTRODUCTION	1-1
2	NONEQUILIBRIUM BOUNDARY LAYER CODE - BLIMP/KINET	2-1
	2.1 Mathematical Model	2-2
	2.1.1 Conservation Equations	2-2
	2.2 Turbulent Flow Considerations	2-7
	2.3 Coordinate Transformations	2-15
	2.4 Boundary Conditions	2-23
	2.5 Homogeneous Chemistry	2-28
	2.6 Heterogeneous Chemistry	2-29
	2.7 Nodal Point Distribution Refit Option	2-30
3	INTEGRAL MATRIX SOLUTION PROCEDURE	3-1
	3.1 Integral Strip Equations with Splined Interpolation Functions	3-1
	3.2 Solution of the Mixing Length Equation	3-8
	3.3 Newton-Raphson Iteration for a Solution	3-10
4	CONSIDERATIONS FOR SHUTTLE APPLICATIONS	4-1
	4.1 Transition to Turbulent Flow	4-1
	4.2 Surface Catalyzed Reactions	4-4
	4.3 Homogeneous Kinetics	4-7
5	TYPICAL RESULTS BASED ON EQUILIBRIUM EDGE BOUNDARY CONDITIONS	5-1
	5.1 Effect of Homogeneous Kinetics	5-1
	5.2 Effect of Number of Nodal Point	5-6
	5.3 Effect of Surface Catalycity	5-6
	5.4 Effect of Pressure	5-12
	5.5 Comparison of Current Predictions with Reference 61	5-12
	5.6 Analysis of Arc Jet Data	5-17
6	APPROXIMATION OF NONEQUILIBRIUM CONDITIONS AT EDGE OF BOUNDARY LAYER	6-1
	6.1 Correlation of Inviscid Shock Layer Flow Field	6-1
	6.2 Geometry	6-2
	6.3 Cases	6-7
	6.4 Equation of State	6-8
	6.5 Body Surface and Shock Surface Representations	6-9
	6.6 Computation of Shock Transition Variables	6-13
	6.7 Streamtube Chemical Relaxation	6-20
7	CALCULATIONS FOR REPRESENTATIVE SHUTTLE VEHICLE	7-1
	7.1 Surface Pressure Distributions and Approximate Boundary Layer Mass Flow Rate	7-5
	7.2 Viscous Shock Layer Solutions in the Stagnation Region	7-5
	7.3 Streamline Pressure and Enthalpy Calculations	7-5
	7.4 Chemical Relaxation Along Streamlines	7-21
	7.5 Heat Transfer on Shuttle Vehicle	7-27
	7.6 Applicability of Boundary Layer Assumptions at Low Densities	7-29
8	SUMMARY AND CONCLUSIONS	8-1
	REFERENCES	R-1
	APPENDIX A	A-1

SYMBOLS

A	parameter used in the solution of the mixing length equation (defined by Equation (126));
\bar{A}	radial offset of the generator axis at angle of attack, Figure 6-4
\bar{A}_0	caloric enthalpy deviation associated with equilibrium dissociation
B	parameter used in the solution of the mixing length equation (defined by Equation (127))
a, b, c	coefficients in polynomial body surface equation
\vec{b}_b	binormal direction unit vector, body oriented coordinates
c	constant introduced in the α_H constraint (Equation (44))
γ_t	constant introduced in the approximation for multicomponent thermal diffusion coefficients embodied in Equation (8). Tentatively established by correlation of data to be -0.5
C	product of density and viscosity normalized by their reference values (defined by Equation (52))
\tilde{C}	tangent shock surface metric, Equation 178
\bar{C}_p	frozen specific heat of the gas mixture
\tilde{C}_p	property of the gas mixture which reduces to \bar{C}_p when diffusion coefficients are assumed equal for all species (defined by Equation (8))
C_{p_i}	specific heat of species i

SYMBOLS
(continued)

d_0, d_1, d_2	coefficients defined in finite-difference representation of streamwise derivatives (defined in Equations (107) and (108) for two- and three-point difference relations, respectively)
\bar{D}	a reference binary diffusion coefficient introduced by the approximation for binary diffusion coefficients embodied in Equation (7)
D_1	square of ratio of tangent to normal shock surface metrics, $(\tilde{C}/\tilde{N})^2$
D_i^T	multicomponent thermal diffusion coefficient for species i
D_{ij}	multicomponent diffusion coefficient for species i and j
\bar{D}	diffusion coefficient for all species when all \bar{D}_{ij} are equal
\bar{D}_{ij}	binary diffusion coefficient for species i and j
\hat{e}_j	unit direction cosines, jth principal axis
ERROR	errors for the various equations during Newton-Raphson iteration (driven toward zero in the iteration)
f	stream function (defined by Equation (45))
F_i	diffusion factor for species i introduced by the approximation for binary diffusion coefficients embodied in Equation (7)
G_2	ratio of effective polytropic exponents in equation of state, $\gamma/(\gamma-1)$
G_j^0	Gibbs free energy for j-th specie
h	static enthalpy of the gas (defined by Equation (5))

SYMBOLS
(continued)

T	static temperature
u	velocity component parallel to body surface
\bar{u}	local dimensionless tangential velocity component
u_τ	shear velocity, defined in Equation (33)
\bar{U}_∞	free stream velocity
v	velocity component normal to body surface
\bar{v}	local dimensionless normal velocity component
x_i	mole fraction of species i
\bar{x}	dimensionless axial measure with origin at nose intercept of body generator axis
\tilde{x}	dimensionless axial trace of shock wave with origin at generator axis intercept
XP_1, XP_2, \dots	truncated series obtained in Taylor series expansion of $\int_{i-1}^i f'p \, d\eta \text{ (defined by Equation (112))}$
y	distance from surface into the boundary layer, measured normal to the surface
\bar{y}	dimensionless normal measure above body surface
y^+	dimensionless y -coordinate defined by Equation (33))

SYMBOLS
(continued)

K	total number of elements; also mixing length constant
K_i	mass fraction of molecular species i
\tilde{K}_{C_k}	total mass fraction of element (or base gas) k contained in surface material (e.g., char) removed by combustion, sublimation, or vaporization
\tilde{K}_{g_k}	total mass fraction of element (or base gas) k contained in gas which enters boundary layer without phase change <u>at the surface</u> (e.g., pyrolysis gases)
\tilde{K}_k	total mass fraction of element (or base gas) k irrespective of molecular configuration (defined by Equation (11))
K_{P_m}	partial pressure equilibrium constant for m -th chemical reaction
l	mixing length (defined by Equation (39))
\tilde{l}	dimensionless mixing length (defined by Equation (57))
L	parameter used in mixing length formulation (defined by Equation (123))
m	mass flow rate per unit area
\dot{m}_c	mass removal rate per unit area of surface material (e.g., char) by combustion, sublimation, or vaporization
\dot{m}_i	dimensionless mass flow associated with the i th streamline
\dot{m}_g	mass flow rate per unit area of gas which enters boundary layer without phase change at the surface (e.g., pyrolysis gases)
\dot{m}_{r_l}	mass removal rate per unit area of l^{th} component surface material (e.g., silica) in the condensed phase (e.g., by melting with subsequent liquid runoff or by spallation)
M	molecular weight of the gas mixture

SYMBOLS
(continued)

M_i	molecular weight of species i
M	Mach number
M^*	effective shock Mach number, Equation 162 -
N	number of nodal points across the boundary layer selected for the purpose of the numerical solution procedure
n_b	normal direction unit vector, body oriented coordinates
\tilde{N}	normal shock surface metric, Equation 178
p	dummy variable representing f' , H_T , or \tilde{K}_k
\bar{p}	dimensionless pressure, i th region
\bar{p}_T	dimensionless total pressure
P	pressure, also a parameter used in the mixing length formulation (defined by Equation (120))
P_i	partial pressure of species i
Pr	frozen Prandtl number of the gas mixture (defined by Equation (71))
Pr_t	turbulent Prandtl number (defined by Equation (55))
q_a	diffusional heat flux per unit area away from the surface
q_{cond}	heat conduction per unit area into the surface material
q_r	one-dimensional radiant heat flux (toward the surface), that is, the <u>net</u> rate per unit area at which radiant energy is transferred across a plane in the boundary layer parallel to the surface

SYMBOLS
(continued)

r	metric coefficient for streamline spreading (equal to local radius in the boundary layer in a meridian plane for axisymmetric flow)
r_o	surface value of r
\bar{r}	dimensionless radial displacement measured from generator axis
R	universal gas constant
Re	Reynolds number; subscripted with the length scale if other than s
R_{eff}	effective nose radius for Newtonian flow
\bar{R}_m	reaction rate for m -th reaction (Equation 91)
R_o	nose radius of curvature
s	distance along body from stagnation point or leading edge
s_o	initial streamline arc measure, Equation 199
\bar{Sc}	reference system Schmidt number (defined by Equation (74))
Sc_t	turbulent Schmidt number (defined by Equation (54))
\bar{s}_o	radial offset of forward stagnation point from generator axis, Figure 6-4
SP_i	mass fraction of i -th specie
t	parameter defined to simplify problems with transverse curvature; see Equation (41)
\hat{t}_b	tangential direction unit vector, body oriented coordinates

SYMBOLS
(continued)

T	static temperature
u	velocity component parallel to body surface
\bar{u}	local dimensionless tangential velocity component
u_τ	shear velocity, defined in Equation (33)
\bar{u}_∞	free stream velocity
v	velocity component normal to body surface
\bar{v}	local dimensionless normal velocity component
x_i	mole fraction of species i
\bar{x}	dimensionless axial measure with origin at nose intercept of body generator axis
\bar{x}	dimensionless axial trace of shock wave with origin at generator axis intercept
XP_1, XP_2, \dots	truncated series obtained in Taylor series expansion of $\int_{i-1}^i f'p \, d\eta \text{ (defined by Equation (112))}$
y	distance from surface into the boundary layer, measured normal to the surface
\bar{y}	dimensionless normal measure above body surface
y^+	dimensionless y -coordinate defined by Equation (33))

SYMBOLS (continued)

y_a^+	constant in the mixing length differential equation (see Equation (29))
Y	principal normal coordinate of body
Z	principal binormal coordinate of body
Z_i	a quantity for species i which is introduced as a result of the approximation for binary diffusion coefficients and reduces to K_i when all diffusion coefficients are assumed equal (defined by Equation (8))
\hat{Z}	angle of attack annular radius of shock wave surface, Figure 6-4
\tilde{Z}_k	a quantity for element (or base species) k which is introduced as a result of the approximation for binary diffusion coefficients and reduces to K_k when all diffusion coefficients are assumed equal (defined by Equation (12))
ZP_1, ZP_2, \dots	truncated series obtained in Taylor series expansion of integrals involving nonsimilar terms (defined by Equation (118))
ω	angle of attack of body generator axis
α^*	flux normalizing parameter (defined by Equation (67))
α_H	normalizing parameter used in definition of \bar{n} (see Equation (43)) defined implicitly by use of a constraint such as Equation (46)
α_{ki}	mass fraction of element (or base species) k in species i
β	streamwise pressure-gradient parameter (defined by Equation (53))
γ	effective polytropic exponent, equation of state
γ	catalytic efficiency
δ	y -dimension normalizing parameter (defined by Equation (56))

SYMBOLS
(continued)

δ_i	dimensionless shock standoff at ith station
Δ_{l-1}	logarithmic distance between two streamwise positions denoted by the subscripts l and $l-1$ (defined by Equation (109))
$\Delta f_i, \Delta f'_i, \dots$	corrections for f_i, f'_i, \dots , during Newton-Raphson iteration
ΔG_j^0	change in free energy for j-th chemical reaction
δ^*	displacement thickness (defined by Equation (36))
δ_i^*	incompressible or velocity displacement thickness (defined by Equation (37))
$\delta\eta$	distance between two boundary layer nodal points (defined by Equation (100))
ϵ_j	inverse density jump at shock front j-th station
$\eta, \hat{\eta}$	transformed coordinate in a direction normal to the surface (defined by Equation (47)). Note: the hat is dropped from $\hat{\eta}$ throughout most of the report
θ	angle between a surface normal and a normal to the body centerline; also time in discussions of the charring ablation program
θ	angle measured clockwise from normal to body generator axis, Figure 6-3
λ	thermal conductivity
$\bar{\kappa}$	dimensionless curvature
μ	shear viscosity

SYMBOLS
(continued)

$\mu_1, \mu_2, \mu_3, \mu_4$	properties of the gas mixture (defined by Equation (8)) which reduce to unity, to M , to $1/M$, and to $\ln M$, respectively, for assumed equal diffusion coefficients
$\mu_{j,m}^R$	stoichiometric coefficient of j -th reactant in m -th chemical reaction (Equation 90)
$\mu_{j,m}^P$	stoichiometric coefficient of j -th product in m -th chemical reaction (Equation 90)
ν	kinematic viscosity
ξ	dimensionless streamline distance, origin at shock intercept
$\xi, \hat{\xi}$	transformed streamwise coordinate (defined by Equation (47)). Note: the hat is dropped from $\hat{\xi}$ throughout most of the report
ρ	density
$\bar{\rho}$	dimensionless density
$\rho_w v_w$	total mass flux per unit area into the boundary layer
$\rho \epsilon_{D_i}$	individual species turbulent eddy diffusivity
$\rho \epsilon_D$	average turbulent eddy diffusivity, where it is assumed that all $\rho \epsilon_{D_i} = \rho \epsilon_D$
$\rho \epsilon_H$	turbulent eddy conductivity
$\rho \epsilon_M$	turbulent eddy viscosity
$\tilde{\rho \epsilon}_M$	dimensionless eddy viscosity (defined by Equation (59))

SYMBOLS
(continued)

σ	Stefan-Boltzmann constant
τ	local shear stress
Γ_{m_i}	third body efficiency of i -th specie in m -th chemical reaction
ϕ_k	elemental production rate (Equation 12)
ψ_i	rate of mass generation of species i per unit volume due to chemical reaction

Subscripts

B	refers to baseline trajectory case, $\alpha = 30^\circ$, $M_\infty = 9.61$, Altitude = 164 Kft
cat	refers to a catalytic surface
edge	pertains to boundary-layer edge
equil	pertains to surface equilibrium requirement
i	pertains to the i^{th} species or to the i^{th} nodal point in the boundary layer, starting with $i = 1$ at the surface
j	pertains to j^{th} species
k	pertains to k^{th} element (or base species)
l	pertains to l^{th} streamwise position
m	pertains to m^{th} iteration during the Newton-Raphson iteration process
n	pertains to the n^{th} nodal points, corresponding to the outer edge of the boundary layer solution

SYMBOLS
(concluded)

o	generator axis conditions
sp	pertains to the stagnation point
s.s.	pertains to the steady state energy balance requirement
w	pertains to wall
l	reference condition, usually taken as zero streamline from inviscid solution (synonymous with boundary-layer edge in the absence of an entropy layer)

Superscripts

δ	refers to conditions at shock wave
K	equal to unity for axisymmetric bodies and zero for two-dimensional bodies
*	signifies that quantity is normalized by α^* (e.g., $j_k^* = j_k/\alpha^*$)
'	represents partial differentiation with respect to η or $\hat{\eta}$ (usually $\hat{\eta}$ unless otherwise noted)

SECTION 1

INTRODUCTION

One of the basic features of the space shuttle vehicle is the reusable thermal protection system which, depending upon the number of flights between refurbishments, strongly affects the economics of transporting men and equipment into space. Because of the restrictions imposed by current high temperature materials technology, equilibrium radiation surface temperatures must be held to relatively low values compared to surface temperatures on a typical RV. For the space shuttle vehicle, low surface temperatures will be achieved by aerodynamic deceleration at high altitudes. However, the low densities associated with high altitudes raises questions about the effects of nonequilibrium chemistry and the validity of boundary layer assumptions, especially in the stagnation region. The size of the proposed shuttle vehicle and its complex geometry poses questions about the effects of entropy gradients and shock interference heating. In addition the designers must be concerned about transition and turbulent flow, gap heating, and discontinuities in surface chemistry due to the tile-like assembly of the TPS.

This report describes the development of analytic procedures to calculate the effects of nonequilibrium chemistry in laminar and turbulent boundary layers over surfaces of arbitrary catalycities. In order to effectively address this problem, however, it was also necessary to establish a procedure for estimating the chemical state of the air at the edge of the boundary layer. This state is determined from the inviscid streamline history which therefore also accounts for entropy layers.

The computational procedure has been used to predict surface heating rates on the windward pitch plane of a typical shuttle vehicle and was compared with the more normal equilibrium boundary layer predictions. The procedure has also been used to examine the effects of chemical reaction rates, surface catalcity and stagnation pressure as well as to predict catalycities of candidate shuttle TPS materials in simulated reentry environments.

SECTION 2

NONEQUILIBRIUM BOUNDARY LAYER CODE - BLIMP/KINET

The development of the governing boundary layer equations and computational procedure for the simultaneous solution of these equations were presented in Reference 1. The procedure described in Reference 1 is applicable to nonsimilar multicomponent laminar boundary layers with arbitrary equilibrium or nonequilibrium chemistry, unequal concentration and thermal diffusion, radiation absorption and emission, second order transverse curvature effects, and a general set of surface boundary conditions which includes an intimate coupling with transient charring-ablation energy and mass balances. A turbulent eddy viscosity model is presented in Reference 2. The resulting Fortran IV computer code which was developed in accordance with the analyses of References 1 and 2 is designated by the code name BLIMP (Boundary Layer Integral Matrix Procedure) but does not include the radiation-emission model and, although permitting selected surface rate-controlled reactions, is restricted to equilibrium chemistry in the boundary layer. The radiation version is code named RABLE and is described in Reference 3. In the following, the extension of BLIMP to include nonequilibrium chemistry in the boundary layer is discussed. (Kinetically controlled surface reactions were already included in the BLIMP code as an input option.)

Since the analysis and computational procedure has been presented in References 1 and 2 the following will be only a brief reiteration of these references with an emphasis on those features which are germane to homogeneous chemistry and surface catalyzed rate controlled reactions. It should be emphasized that none of the generalized procedures and capabilities developed in BLIMP have been destroyed or altered in the process of extending BLIMP to BLIMP/KINET. BLIMP/KINET is currently limited to 7 nonequilibrium species controlled by a maximum of 20 stoichiometric chemical reactions, exclusive of different third body efficiencies. Kinetic rates are calculated in accordance with the development in Reference 4.

2.1 MATHEMATICAL MODEL

2.1.1 Conservation Equations

Omitting radiation transport, the global conservation of mass, momentum and energy, and the specie conservation equations are respectively

$$\frac{\partial \rho u r^K}{\partial s} + \frac{\partial \rho v r^K}{\partial y} = 0 \quad (1)$$

$$\rho u \frac{\partial u}{\partial s} + \rho v \frac{\partial u}{\partial y} = \frac{1}{r^K} \frac{\partial}{\partial y} \left[\rho r^K (v + \epsilon_M) \frac{\partial u}{\partial y} \right] - \frac{\partial P}{\partial s} \quad (2)$$

$$\rho u \frac{\partial H_T}{\partial s} + \rho v \frac{\partial H_T}{\partial y} = \frac{1}{r^K} \frac{\partial}{\partial y} \left[\rho r^K (\epsilon_M + v) \frac{\partial u^2/2}{\partial y} + \right. \quad (3)$$

$$\left. r^K (\lambda + \rho \epsilon_H \bar{C}_P) \frac{\partial T}{\partial y} + r^K \sum_i \left(\rho \epsilon_D \frac{\partial K_i}{\partial y} - j_i \right) h_i - \right.$$

$$\left. \frac{r^K RT}{\rho} \sum_i \sum_j \frac{x_j D_{ij}^T}{x_i D_{ij}} \left(\frac{j_i}{K_i} - \frac{j_j}{K_j} \right) + r^K q_r \right]$$

$$\rho u \frac{\partial K_i}{\partial s} + \rho v \frac{\partial K_i}{\partial y} = \frac{1}{r^K} \frac{\partial}{\partial y} \left[r^K \left(\rho \epsilon_{D_i} \frac{\partial K_i}{\partial y} - j_i \right) \right] + \psi_i \quad (4)$$

$$H_T = h + \frac{u^2}{2} \quad (5)$$

$$h = \sum_i K_i h_i$$

$$h_i = \int_{T^0}^T C_{P_i} dT + h_i^0$$

and the coordinates z , s , and y are shown in Figure 2-1. The flux j_i for multi-component diffusion is obtained from the Stefan-Maxwell relation

$$\frac{\partial x_i}{\partial y} = \sum_j \frac{x_i x_j}{\rho D_{ij}} \left[\frac{j_j + D_j^T \frac{\partial \ln T}{\partial y}}{K_j} - \frac{j_i + D_i^T \frac{\partial \ln T}{\partial y}}{K_i} \right] \quad (6)$$

using the bifurcation approximation of References 5 and 6. In this procedure, the binary diffusion coefficient D_{ij} is approximated by the function

$$D_{ij} \approx \frac{\bar{D}(T, P)}{F_i F_j} \quad (7)$$

where \bar{D} is a reference diffusion coefficient and F_i is a diffusion factor for specie i . Then with a few of the following definitions

$$\begin{aligned} z_i &\equiv \frac{m_i x_i}{F_i \mu_2} & \mu_4 &\equiv \ln(\mu_2 T^{c_t}) \\ \mu_1 &\equiv \sum_j x_j F_j & c_t &\approx -0.5 \\ \mu_2 &\equiv \sum_j \frac{m_j x_j}{F_j} & \tilde{c}_p &\equiv \sum_i z_i c_{p_i} \\ \mu_3 &\equiv \sum_i \frac{z_i}{m_i} & \tilde{h} &\equiv \sum_i z_i h_i \end{aligned} \quad (8)$$

the Stefan-Maxwell equations can be solved explicitly for the diffusive flux, i.e.,

$$j_i = - \frac{\rho \bar{D} \mu_2}{\mu_1 m_i} \left[\frac{\partial z_i}{\partial y} + (z_i - K_i) \frac{\partial \mu_4}{\partial y} \right] \quad (9)$$

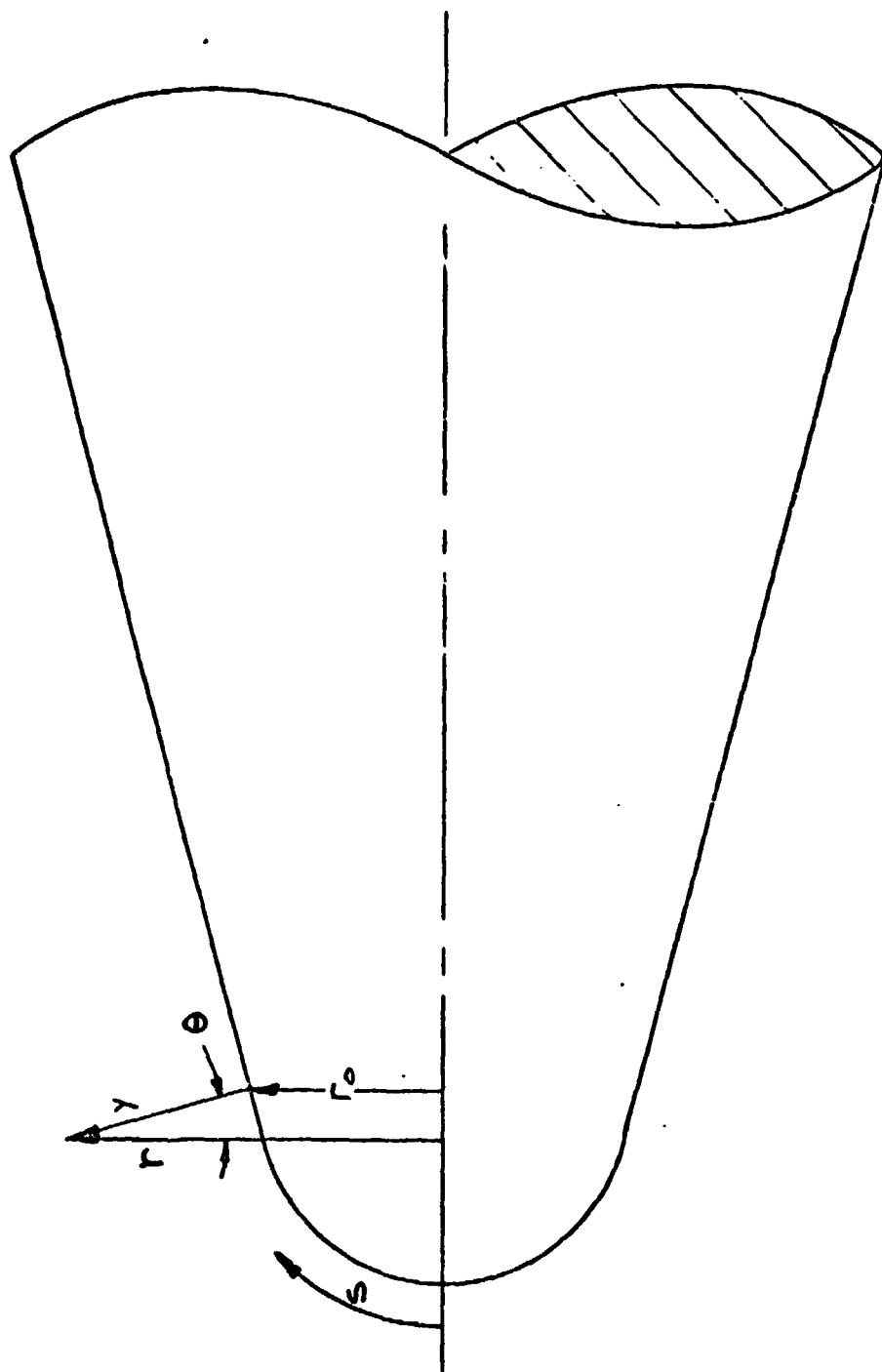


Figure 2-1 Definition of the Coordinate Nomenclature

In addition the diffusive energy flux can be expressed as

$$q_a = - \left\{ \rho (\epsilon_M + v) \frac{\partial \left(\frac{u^2}{2} \right)}{\partial y} + (\lambda + \rho \epsilon_H \bar{C}_p) \frac{\partial T}{\partial y} + \rho \epsilon_D \left(\frac{\partial h}{\partial y} - \bar{C}_p \frac{\partial T}{\partial y} \right) + \frac{\rho \bar{D} \mu_2}{\mu_1 \mathcal{M}} \left[\frac{\partial \tilde{h}}{\partial y} - \left(\tilde{C}_p + \frac{c_t^2 R}{\mu_1 \mu_2} \right) \frac{\partial T}{\partial y} + c_{tRT} \frac{\partial \mu_3}{\partial y} + (\tilde{h} - h + c_{tRT} \mu_3) \frac{\partial \mu_4}{\partial y} \right] \right\} \quad (10)$$

For some problems (e.g., equilibrium chemistry) the number of differential equations to be solved can be substantially reduced if conservation of "elements" rather than conservation of species is used. Thus by defining the elemental mass fraction by

$$\tilde{K}_k = \sum \alpha_{ki} K_i \quad (11)$$

and

$$\tilde{z}_k \equiv \sum_i \alpha_{ki} z_i \quad (12)$$

$$\phi_k \equiv \sum_i \alpha_{ki} \psi_i$$

the diffusive flux will be represented by

$$j_k = - \frac{\rho \bar{D} \mu_2}{\mu_1 \mathcal{M}} \left[\frac{\partial \tilde{z}_k}{\partial y} + (\tilde{z}_k - \tilde{K}_k) \frac{\partial \mu_4}{\partial y} \right] \quad (13)$$

and the "elemental" species conservation equation becomes

$$\rho u \frac{\partial \tilde{K}_k}{\partial s} + \rho v \frac{\partial \tilde{K}_k}{\partial y} = \frac{1}{r^k} \frac{\partial}{\partial y} \left[r^k \left(\rho \epsilon_{Dk} \frac{\partial \tilde{K}_k}{\partial y} - j_k \right) \right] \quad (14)$$

Since elements are conserved, $\sum \alpha_{ij} \psi_j = 0$ so that this formulation would not be appropriate for nonequilibrium chemistry since the production terms vanish. However by reintroducing the production term into this conservation equation, the same formulation can be used for equilibrium or nonequilibrium chemistry by the simple expedient of setting the production terms to zero for equilibrium conditions. In addition, for nonequilibrium chemistry each specie is considered as an element and the "elemental" specie conservation equation serves to alter the elemental composition of the gas mixture. The conservation equations to be solved are therefore

$$\frac{\partial \rho u r^k}{\partial s} + \frac{\partial \rho v r^k}{\partial y} = 0 \quad \text{global mass} \quad (15)$$

$$\rho u \frac{\partial u}{\partial s} + \rho v \frac{\partial u}{\partial y} = \frac{1}{r^k} \frac{\partial}{\partial y} \left[\rho r^k (v + \epsilon_M) \frac{\partial u}{\partial y} \right] - \frac{\partial P}{\partial s} \quad \text{streamwise momentum} \quad (16)$$

$$\rho u \frac{\partial H_T}{\partial s} + \rho v \frac{\partial H_T}{\partial y} = \frac{1}{r^k} \frac{\partial}{\partial y} \left[r^k (-q_a +) \right] \quad \text{energy} \quad (17)$$

$$\rho u \frac{\partial \tilde{K}_k}{\partial s} + \rho v \frac{\partial \tilde{K}_k}{\partial y} = \frac{1}{r^k} \frac{\partial}{\partial y} \left[r^k \left(\rho \epsilon_D \frac{\partial \tilde{K}_k}{\partial y} - j_k \right) \right] + \phi_k \quad \text{"elemental" specie} \quad (18)$$

where

$$\phi_k \equiv \sum_i \alpha_{ki} \psi_i$$

For nonequilibrium chemistry,

$$\alpha_{ki} = 0, \quad k \neq i$$

$$\alpha_{ki} = 1.0, \quad k = i$$

These equations, which include the approximations for unequal thermal and multicomponent diffusion coefficients of Reference 6, are parabolic in nature and therefore requiring specifications of the dependent variables, their derivatives, or a linear combination thereof along the wall ($y = 0$), edge of the boundary layer, and at the initial body station. Typical sets of boundary conditions will be discussed later in this report. Also necessary in the mathematical formulation of the problem is the specification of the molecular transport properties, equation of state and equilibrium relations for the multicomponent gas, and a description of the eddy viscosity, conductivity and diffusivity. The molecular transport properties, equation of state, and equilibrium relations are discussed in references 2 and 4.

2.2 TURBULENT FLOW CONSIDERATIONS

In the conservation equations developed above, the concepts of eddy viscosity, eddy diffusivity, and eddy conductivity were used to express the correlations of fluctuating velocity, species, and enthalpy fields in terms of mean field quantities. This is only one of several possible techniques of closing the set of equations (assuming satisfactory expressions for the eddy parameters are available), and it does not provide any information regarding the evolution of the turbulent correlations as the flow progresses downstream. Admittedly, it would be more desirable to describe the turbulent fluctuations in a more complete manner such as with an entrainment relation, turbulent kinetic energy relation, or a local turbulent constitutive equation (Reference 7). However, these techniques are still in early stages of development even for incompressible single component flows, therefore a more proven approach was selected for the present analysis. The Boussinesq description of turbulent boundary layers has proved to be very useful, particularly for complex reacting flows such as are being described here, and will be used exclusively in the present analysis.

There is a wide amount of latitude possible even within the eddy viscosity framework of turbulence, particularly in applying classical incompressible models to compressible flows. The following two subsections describe how the turbulence model described in Reference 8 was applied to the present compressible flow problem.

a. Wall Region

Following the work of Clauser (Reference 9) the boundary layer is divided into a law of the wall region and a wake region. The relatively thin wall region of the turbulent boundary layer is characterized by very steep gradients in the turbulent transport and mean field properties. Turbulent stress varies from zero at the wall to near its maximum value at the outer edge of the wall region. There is a vast amount of empirical evidence that these turbulent stresses and also the mean flow field properties can be described entirely in terms of the wall state, wall fluxes, thermodynamic and transport properties of the fluid, and the normal coordinate y . Since the streamwise coordinate does not enter the solution for this region, the problem becomes a one-dimensional initial value problem. Eliminating s derivatives from the continuity equation and neglecting variations in r due to the thinness of the layer results in

$$\frac{d(\rho v)}{dy} = 0 \quad (19)$$

or

$$\rho v = \rho_w v_w \quad (20)$$

where the subscript w refers to the wall value. Thus the wall injection rate, $\rho_w v_w$, which may be a function of s , determines the transverse mass flux through the entire wall region. Using the same technique for the momentum equation and substituting equation (20)

$$\rho_w v_w u = \rho(v + \epsilon_M) \frac{du}{dy} - \tau_w \quad (21)$$

where the wall shear, τ_w , is also typically a function of s . For flows over an impermeable wall with constant properties, this equation reduces to

$$\rho(v + \epsilon_M) \frac{du}{dy} = \tau_w \quad (22)$$

or

$$\tau = \tau_w \quad (23)$$

indicating that shear can be considered constant in the wall region. For flows with injection or ablation, it is seen that shear varies with the mass injection rate and local velocity, that is,

$$\tau = \tau_w + \rho_w v_w u \quad (24)$$

This one-dimensional description of turbulence in the wall region will be useful in formulating a mixing length model for eddy viscosity as described in the following paragraphs. It should be made clear however, that only the wall region turbulent shear stress is assumed to behave in a one-dimensional fashion. In the solution procedure, the complete two-dimensional equations of motion are solved over the entire boundary layer.

A complete investigation of the validity of the mixing length postulate for flows with injection has been reported in Reference 10. The analysis used in this investigation is an extension of that work; therefore, the reader should refer to Reference 10 for more details.

Because of the current lack of understanding of turbulent mechanisms, "theoretical" predictions of the variation of turbulence near the wall must rely on empirical input into relations based on some phenomenological dependence. The generality of the ultimate goals of this analysis and the desire to approximate the physical situation dictated certain prerequisites for the turbulent transport relations. These were:

- a) The relations must indicate a continuous variation of the turbulent transport properties from the wall to the fully turbulent region.
- b) The relations must be generally applicable to mass, momentum, and energy transport.
- c) The relations must be applicable to compressible or incompressible flows with real gas properties.
- d) The relations should be suitable for transpired and untranspired boundary layers without any, or a minimum, modification of form.

Two basic variations of the eddy viscosity hypothesis have been proposed in the past. The first type predicts the variation of turbulent viscosity from the wall to the fully turbulent region. The second type of hypothesis involves a variation of mixing length from the wall into the fully turbulent portion of the boundary layer. Data indicate that surface mass addition strongly affects the eddy viscosity profile, and it was found that the first type of hypothesis could not be simply modified to predict this variation. On the other hand, success of the mixing length theory in predicting profiles in the fully turbulent portion of the boundary layer with surface mass addition has been noted, for example, in Reference 11 and 12. It has generally been concluded that the slope of the linear relation between mixing length and distance from the wall is insensitive to surface mass addition. As a consequence of this apparent generality of the mixing length approach, it was adopted for the present studies.

The basic mixing length postulate can be expressed as

$$\overline{(\rho v)' u'} = \rho l^2 \left(\frac{du}{dy} \right)^2 = \rho \epsilon_M \frac{du}{dy} \quad (25)$$

where the mixing length, l , is a combination of various correlations, but retains some relationship to the scale of turbulence. Prandtl proposed that this length will, in its simplest form, be related to the distance from a wall, at least in the region of development of turbulence. His proposition that

$$\frac{dl}{dy} = \text{constant}, K \quad (26)$$

has been tested under a variety of conditions and found to be quite adequate in the fully turbulent portion of the wall region.

As the wall is approached however, this simple relation is no longer appropriate, and, in fact, it can be shown theoretically that

$$\left. \begin{aligned} \lim_{y \rightarrow 0} l &= 0 \\ \lim_{y \rightarrow 0} \frac{dl}{dy} &= 0 \end{aligned} \right\} \quad (27)$$

This is a consequence of the Reichardt-Elrod criterion (see Reference 10). Thus, two criteria are specified, namely, Prandtl's hypothesis which is appropriate in the fully turbulent portion of the wall region and the Reichardt-Elrod wall criterion as expressed by Equation (27).

Several means of expressing a relation covering the full range of y and including these limiting criteria have been used by other investigators. It is advantageous in considering extensions of mixing length theory to establish some physical logic for the selected relation. Unfortunately, the understanding of transition from the laminar to the turbulent portions of the layer has not reached a state permitting any quantitative specification. Therefore, the selected model can be based only on qualitative understanding of the process, dimensional considerations, and the above limiting criteria. These criteria are satisfied for incompressible flows by a simple implicit relation of the form

$$\frac{dl}{dy} \propto (Ky - l) \quad (28)$$

which implies that the rate of increase of the mixing length is proportional to the difference between the value postulated by Prandtl (Ky) and its actual value. This rate of increase is assumed to be augmented by the local shear and retarded by the local viscosity. Using these parameters to nondimensionalize the above relation yields

$$\frac{dl}{dy} = (Ky - l) \frac{\sqrt{\tau/\rho}}{y_a^+ v} \quad (29)$$

where y_a^+ is the constant of proportionality. The coefficients K and y_a^+ were shown in Reference 10 to be invariant for a wide variety of flow conditions at values of 0.44 and 11.83, respectively.

For compressible flows, the physical arguments must be changed somewhat. Rather than describing the scale of a turbulent eddy, it seems appropriate to describe the mass of the eddy, ρl , with respect to the mass available, $\int \rho dy$.

Thus, by analogy to Equation (29), the rate of increase of the mass of an eddy will be taken to be proportional to the difference between the mass available between the wall and the point of interest (times an appropriate constant) and the mass of the eddy:

$$\frac{1}{\rho} \frac{d\rho l}{dy} = K \int_0^y \rho dy - \rho l \quad (30)$$

Nondimensionalizing as above,

$$\frac{1}{\rho} \frac{d\rho l}{dy} = \left(K \int_0^y \rho dy - \rho l \right) \frac{\sqrt{\tau/\rho}}{y_a^+ v} \quad (31)$$

The constants K and y_a^+ are left at their incompressible values of 0.44 and 11.83 for the time being. The integral-differential character of this mixing length equation indicates a difficult solution procedure in the physical coordinate plane. However, in the (η, ξ) coordinates introduced by the Levy-Lees transformation, the mixing length equation simplifies somewhat. This will be discussed further in Section 2.3.

For the special case of constant properties and zero injection (constant shear), Equation (31) can be integrated to yield

$$l = \frac{Kv}{u_\tau} \left\{ y^+ - y_a^+ \left[1 - \exp\left(-\frac{y^+}{y_a^+}\right) \right] \right\} \quad (32)$$

where

$$u_\tau = \sqrt{\frac{\tau_w}{\rho}} \quad (33)$$

$$y^+ = \frac{yu_\tau}{v}$$

It can be seen that the Reichardt-Elrod criteria is satisfied at the wall. For large y , the expression

$$l = \frac{Kv}{u_\tau} (y^+ - y_a^+) \quad (3)$$

is obtained. This special case result for constant property zero injection flows is not used in the general analysis technique presented here.

b. Wake Region

The wake region of a turbulent boundary layer is so named because the flow in this region tends to have a wake-like character. In particular, the outer 80 to 90 percent of the boundary layer combined with the local turbulent eddies dominates the mixing processes within the flow, and the viscous effects become second order. Gradients in the wake region are typically much smaller than those of the wall region. Since the pressure gradient and streamwise derivative terms are important in the wake region, the two-dimensional character of the turbulence must be considered in its entirety, as opposed to the approximations of the wall region.

A fortunate feature of the wake portion of the boundary layer is that eddy viscosity is nearly constant across this region, at least for equilibrium[†] incompressible flows. In particular, Clauser (Reference 9) was able to relate the eddy viscosity to edge velocity and a length scale δ^*

$$\epsilon_M = 0.018 u_1 \delta^* \quad (35)$$

for a great quantity of experimental data taken in equilibrium flows.

The quantity δ^* in this relation is the displacement thickness

$$\delta^* = \int_0^\infty \left(1 - \frac{\rho u}{\rho_1 u_1} \right) dy \quad (36)$$

[†]Equilibrium as used here refers to a particular pressure gradient, $(\delta^*/\tau_w)(dP/dx)$, which results in self-similar velocity profiles (Reference 9).

in which the densities cancel out for incompressible flows. For compressible flows, this length scale is inappropriate since under some conditions δ^* can be negative. Defining a velocity defect thickness as

$$\delta_1^* = \int_0^\infty \left(1 - \frac{u}{u_1}\right) dy \quad (37)$$

the eddy viscosity in the wake portion of the flow will be taken as

$$\epsilon_M = 0.018 u_1 \delta_1^* \quad (38)$$

a satisfactory technique for choosing the correct ϵ_M expression at any particular body station is to use the wall region expression

$$\epsilon_M = l^2 \frac{du}{dy} \quad (39)$$

until ϵ_M exceeds the wake value, Equation (38), at which point ϵ_M is held constant at the wake value for the remainder of the boundary layer thickness.

c. Boundary Layer Transition

As can be seen from the form of the conservation equation, both the molecular and turbulent transport terms are considered simultaneously. This is necessary since an accurate description of the turbulent boundary layer requires that the time-averaged fluctuation terms disappear near the wall. Another reason for the inclusion of these terms is the description of laminar or transitional flows. From the form of Equation (38), it can be seen that for very small δ_1^* the turbulent stresses will be small compared to the laminar ones. Without any constraints on the equations as stated above, kinematic and eddy viscosities are equal at a velocity displacement thickness Reynolds number of 56:

$$1 = \frac{\epsilon_M}{\nu} = \frac{0.018 u_1 \delta_1^*}{\nu}$$

$$\therefore Re_{\delta_1^*} = 56$$

This "natural" transition Reynolds number is too low for most situations, therefore ϵ_M is artificially set to zero until some other criterion is satisfied. A Reynolds number on momentum thickness, Re_θ , is currently used to trigger transition. When a user prescribed Re_θ is exceeded turbulent transport properties are introduced into the calculations; however they are reduced by a scale factor varying between 0 and 1 to simulate a transition zone. The scaling factor, often referred to as an intermittency factor, has been reviewed in Reference 13 and a quadratic variation with streamwise coordinate has been recommended. However, due to the current state of transition data, a simple linear relation (Reference 14) was used. Thus

$$\epsilon_M = I(s) \epsilon_M(\text{ref}) \quad (40)$$

where $\epsilon_M(\text{ref})$ is calculated as if the flow were fully turbulent and

$$\begin{aligned} I(s) &= \frac{s}{s_t} - 1.0 & s_t &\leq s \leq 2 s_t \\ I(s) &= 0 & s &\leq s_t \\ I(s) &= 1 & s &\geq 2s_t \end{aligned} \quad (41)$$

2.3 COORDINATE TRANSFORMATIONS

The equations of motion for a boundary layer flow can be solved in the physical (s,y) plane by numerous techniques, however it is generally advantageous to transform the problem to another coordinate system. The transformed coordinates offer the advantages of nondimensionalizing the solution, confining the solution to a narrower region, minimizing changes in the dependent variables, simplifying boundary conditions and occasionally result in the deletion of streamwise derivative terms. This latter possibility occurs only under very restrictive sets of boundary conditions. The coordinate transformation in the present analysis is a variation of the Levy-Lees transformation and is derived in its entirety in Reference 1. The standard Levy-Lees transformation takes the form

$$\xi = \int_0^s \rho_1 u_1 \mu_1 r_0^{2K} ds \quad (42)$$

$$\eta = \frac{r_0^K u_1}{\sqrt{2\xi}} \int_0^y \rho dy$$

The first alteration of this transformation is actually a mathematical convenience for carrying out the numerical solution. Introducing a stretching parameter α_H in the normal coordinate, a new coordinate system is defined by

$$\bar{\xi} = \xi \quad (43)$$

$$\bar{\eta} = \frac{\eta}{\alpha_H}$$

The parameter α_H is taken as a function of $\bar{\xi}$ only and is determined implicitly during the solution. Its purpose is to stretch the η coordinate such that the boundary layer remains of constant thickness in the $\bar{\eta}$ coordinates.

Since a new variable $\alpha_H(\bar{\xi})$ is introduced, an additional relation is required. This is conveniently supplied by constraining some arbitrary point near the boundary-layer edge, $\bar{\eta}_c$, to have a specified streamwise velocity, c , near (but something less than) the edge value:

$$f' \Big|_{\bar{\eta}_c} = c f' \Big|_{\bar{\eta}_{\text{edge}}} \quad (44)$$

where f is the transformed stream function defined as

$$f - f_w = \int_0^{\bar{\eta}} \frac{u}{u_1} d\bar{\eta} = \alpha_H \int_0^{\bar{\eta}} \frac{u}{u_1} d\bar{\eta} \quad (45)$$

and the prime denotes differentiation with respect to $\bar{\eta}$ so that

$$f' = \alpha_H \frac{u}{u_1} \quad (46)$$

Examples of the utility of the stretching parameter α_H are contained in Reference 1.

The second change in the Levy-Lees transformation has to do with the transverse curvature effect. For very thin axisymmetric bodies, it is possible to have boundary layer thicknesses on the order of the body radius r_0 . In this instance, it is necessary to treat r as a function of y , thereby including its variation through the boundary layer. The coordinate transformations become

$$\hat{\xi} = \int_0^s \rho_1 u_1 \mu_1 r_0^{2K} ds \quad (47)$$

$$\hat{\eta} = \frac{v_1}{\alpha_H \sqrt{2\xi}} \int_0^y \rho r^K dy$$

Utilization of the above coordinate transformation relations results in a new set of governing equations in the $(\hat{\xi}, \hat{\eta})$ coordinate plane which will be given below. The hat (^) notation will be dropped for the remainder of the text for simplicity, however ξ and η are given by Equation (47). Primes will refer to derivatives with respect to η except when noted otherwise.

The global continuity equation is automatically satisfied by the definition of a transformed stream function $f(\xi, \eta)$, shown in Equation (45), and re-defined here in the final coordinate system:

$$f - f_w = \alpha_H \int_0^\eta \frac{u}{u_1} d\eta \quad (48)$$

$$f_w = - \frac{1}{\sqrt{2\xi}} \int_0^\xi \frac{\rho_w v_w}{\rho_1 u_1 \mu_1 r_o^\kappa} d\xi \quad (49)$$

The governing equations will be discussed separately.

Streamwise momentum equation

$$\begin{aligned} ff'' + \left[\frac{tC \left(1 + \frac{\epsilon_M}{v}\right)}{a_H} f'' \right] + \beta \left(a_H^2 \frac{\rho_1}{\rho} - f'^2 \right) \\ = 2 \left(f' \frac{\partial f'}{\partial \ln \xi} - f'^2 \frac{\partial \ln a_H}{\partial \ln \xi} - f'' \frac{\partial f}{\partial \ln \xi} \right) \end{aligned} \quad (50)$$

In this equation, utilizing the technique of Reference 15, the transverse curvature effect is included entirely in the coordinate transformation and in the definition of t :

$$t \equiv \left(\frac{r}{r_o} \right)^2 = 1 + \frac{2a_H \sqrt{2\xi} \cos \theta}{u_1 r_o^2} \int_0^\eta \frac{1}{\rho} d\eta \quad (51)$$

where θ is the angle between the surface normal and a plane normal to the body centerline (see Figure 2-1). Other definitions of interest are:

$$C \equiv \frac{\rho \mu}{\rho_1 \mu_1} \quad (52)$$

$$\beta \equiv 2 \frac{\partial \ln u_1}{\partial \ln \xi} \quad (53)$$

For solutions without consideration of transverse curvature, t is set to 1.0 throughout the boundary layer.

Turbulent model equations

The turbulent fluctuations are related to the mean field through the eddy models described in Reference 2. Eddy viscosity is described by a wall law and wake law, while eddy diffusivity and conductivity are related to eddy viscosity by turbulent Schmidt and Prandtl numbers:

$$Sc_t \equiv \frac{\epsilon_M}{\epsilon_D} \quad (54)$$

$$Pr_t \equiv \frac{\epsilon_M}{\epsilon_H} \quad (55)$$

Defining

$$\delta \equiv \frac{\sqrt{2\xi}}{\rho_1 u_1 r_c^{\kappa}} \quad (56)$$

$$\tilde{l} \equiv \frac{\rho l}{\rho_1 \delta} \quad (57)$$

$$Re_\delta \equiv \frac{\rho_1 u_1 \delta}{\mu_1} \quad (58)$$

$$\tilde{\epsilon}_M \equiv \frac{\rho^2 \epsilon_M}{\rho_1 \mu_1} \quad (59)$$

The wall region eddy viscosity relation becomes

$$\tilde{\epsilon}_M = \frac{\rho (Re_\delta)}{\rho_1 \alpha_H^2} \tilde{l}^2 f^n \quad (\text{wall region}) \quad (60)$$

$$\tilde{\epsilon}_M = 0.019 \left(\frac{\rho}{\rho_1} \right)^2 Re_{\delta_1^*} \quad (\text{wake region}) \quad (61)$$

where

$$\delta_1^* = \delta \alpha_H \int_0^\infty \left(1 - \frac{\xi'}{\alpha_H} \right) \frac{\rho_1}{\rho} d\eta \quad (62)$$

Transverse curvature is not considered in determining the wake region length scale δ_1^* . The governing equation for mixing length, which must be solved for the entire boundary layer although it is used only in the wall region, is

$$\frac{d\tilde{l}}{d\eta} = \frac{\alpha_H \rho_1 \delta \sqrt{\tau/\eta}}{y_a^+ \mu} \left(K \alpha_H \eta - \tilde{l} \right) \quad (63)$$

Since mixing length is used only in the wall region, it is valid to use the one-dimensional expression for shear stress, Equation (24). In transformed coordinates, this becomes

$$\frac{\tau}{\rho} = \frac{u_1^2}{\alpha_H} \frac{\rho_1}{\rho} \left[\frac{C_w}{\alpha_H} \frac{f_w^*}{Re_\delta} + \frac{\rho_w v_w}{\rho_1 u_1} f' \right] \quad (64)$$

Energy equation

$$f H_T' + \left[t(-q_a^* + q_r^*) \right]' = 2 \left(f' \frac{\partial H_T}{\partial \ln \xi} - H_T' \frac{\partial f}{\partial \ln \xi} \right) \quad (65)$$

where q_a^* is the normalized diffusive energy flux away from the surface including turbulent fluxes

$$q_a^* = q_a / \alpha^* \quad (66)$$

The flux normalizing parameter α^* is defined by

$$\alpha^* \equiv \frac{\rho_1 u_1 \mu_1 r_o^k}{\sqrt{2\xi}} = \frac{\mu_1}{\delta} \quad (67)$$

Diffusive energy flux q_a in the transformed coordinates is defined later in this section.

"Elemental" species equations

$$\begin{aligned} f \tilde{K}_k' + \left[t \left(\frac{\tilde{e}_M}{\alpha_H Sc_t} \tilde{K}_k' - j_k^* \right) \right]' + \left(\frac{\phi_k}{\rho} \right) \left(\frac{\rho_e \mu_e \alpha_H}{\alpha^{*2}} \right) \\ = 2 \left(f' \frac{\partial \tilde{K}_k}{\partial \ln \xi} - \tilde{K}_k' \frac{\partial f}{\partial \ln \xi} \right) \end{aligned} \quad (68)$$

where j_k^* is the normalized diffusive flux of "element" k:

$$j_k = j_k^* \alpha^* \quad (69)$$

Diffusive fluxes

The normalized diffusive energy flux is given by

$$\begin{aligned} q_a^* = - \frac{C}{\alpha_H} & \left[\frac{f' f''}{\alpha_H^2} u_1^2 + \frac{\bar{C}_p}{Pr} T' + \frac{1}{Sc} \left(\bar{h}' - \left(\bar{C}_p + \frac{c_t^2 R}{\mu_1 \mu_2} \right) T' \right. \right. \\ & \left. \left. + c_t R T \mu_3' + (\bar{h} - h + c_t R T \mu_3) \mu_4' \right) \right] \\ & - \frac{\tilde{\epsilon}_M}{\alpha_H} \left[\frac{f' f''}{\alpha_H^2} u_1^2 + \frac{\bar{C}_p}{Pr_t} T' + \frac{1}{Sc_t} (h' - \bar{C}_p T') \right] \end{aligned} \quad (70)$$

where Pr is the Prandtl number based on the frozen specific heat

$$Pr \equiv \frac{\bar{C}_p u}{\lambda} \quad (71)$$

The turbulent contribution to the diffusive energy flux is contained in the last bracketed term, which is left uncombined with the other terms for clarity. The fact that the gross simplifications of the turbulent model are included in the same equation with the rather sophisticated unequal molecular diffusion model is merely a mathematical convenience stimulated by the requirement for calculations in all types of flow situations, including both laminar and turbulent flows. Unequal molecular diffusion and thermal diffusion effects may be important in the laminar sublayer region of a turbulent boundary layer, however.

Normalized molecular diffusive flux of species i is

$$j_i^* = - \frac{C}{\alpha_H Sc} \left[\tilde{z}_i' + (\tilde{z}_i - \tilde{K}_i) \mu_4' \right] \quad (73)$$

where \overline{Sc} is a system property defined by

$$\overline{Sc} \equiv \frac{\mu_1 \mu_2}{\rho \bar{D} \mu_2} \quad (74)$$

The \overline{Sc} is a Schmidt number based on the self-diffusion coefficient for a fictitious species representative of the system as a whole. The normalized molecular diffusive flux of the k^{th} "elemental" species is

$$j_k^* = - \frac{C}{\alpha_H \overline{Sc}} \left[\tilde{z}_k' + (\tilde{z}_k - \tilde{K}_k) \mu_4' \right] \quad (75)$$

When certain groupings of parameters are constant so that the flow similarity assumption is valid, the terms on the right-hand side of the conservation equations (Equations 50, 65, and 68) vanish, in which case the conservation equations become ordinary differential equations. It should be emphasized that the equations as presented herein are equivalent to the corresponding boundary-layer equations presented in Section 2.1. That is, no similarity assumptions have been made in their development.

Equations 67, 53, and 49 for α^* , β , and f_w , respectively, are indeterminate at the stagnation point of a blunt body. Special forms for these equations valid at the stagnation point are shown in Reference 1 to be given by

$$\alpha_{sp}^* = \left(\rho_1 \mu_1 \frac{du_1}{ds} / \beta \right)_{sp}^{1/2} \quad (76)$$

$$f_{w,sp} = - \left(\rho_w v_w / \alpha^* \right)_{sp} \quad (77)$$

where for Newtonian flow

$$\beta_{sp} = 1/(i\kappa + 1) \quad (78)$$

where i is the ratio of the crosswise to pitch-plane stagnation-point velocity gradients ($i = \kappa$ for axisymmetric or planar flow), and

$$\left. \frac{du_1}{ds} \right|_{sp} = (2P/\rho)_{sp}^{1/2} / R_{eff} \quad (79)$$

With R_{eff} an effective nose radius taking into account the shock shape. Alternatively, β_{sp} and $(du_1/ds)_{\text{sp}}$ can be computed from curve fits of the inviscid pressure distribution. The transverse curvature parameter t also requires some special treatment at a stagnation point. The troublesome term is $\cos \theta/r_0$ which is evaluated at a stagnation point by

$$\left(\frac{\cos \theta}{r_0} \right)_{\text{sp}} = \left[6 \frac{d^2(1 - \frac{r_0}{s})}{ds^2} \right]^{1/2} \quad (80)$$

In addition, to improve the accuracy of numerical integration procedures in the nose region, ξ and f_w can be computed by the following relations

$$\xi = \frac{1}{2(\kappa + 1)} \int_0^{s^{2\kappa+2}} \left[\rho_{\perp 1} \left(\frac{u_1}{s} \right) \left(\frac{r_0}{s} \right)^{2\kappa} \right] d(s^{2\kappa+2}) \quad (81)$$

$$f_w = - \frac{(2\xi)^{-1/2}}{(\kappa + 1)} \int_0^{s^{\kappa+1}} \left[\rho_w v_w \left(\frac{c}{s} \right) \right] d(s^{\kappa+1})$$

which take advantage of the fact that u_1/s and $r_0/s^{\frac{1}{2}}$ vary more nearly linearly in the stagnation region than do u_1 and r_0 . The basic approach is discussed more thoroughly in Reference 1 while the parameter i is discussed in Reference 16.

2.4 BOUNDARY CONDITIONS

The usual set of boundary conditions for the boundary layer flow problem consists of the specification of initial profiles for the dependent variables f' , H_T , and K_k , plus additional specifications of these quantities along the wall and at the edge of the boundary layer, and the specification of f_w along the wall. However, since the main utilization for the analytical technique presented here is to compute boundary layer properties for flows over ablating or transpired surfaces (heat shields, rocket nozzles, etc.), these boundary conditions have been greatly generalized. The numerous options resulting from this generalization are discussed below.

The boundary layer edge conditions typically are found from an isentropic expansion from known elemental gas composition and stagnation conditions. Thus, given a set of stagnation conditions and a description of local static pressure along the surface of interest, the techniques of Reference 4 may be used to establish the entropy of the gaseous mixture which, when combined with the specified pressures, can be used to establish the complete equilibrium edge gas state at each body station. Edge boundary conditions then would consist of

$$\begin{aligned} f'_{\text{edge}} &= \alpha_H \\ H_{T_{\text{edge}}} &= H_{T_{\text{edge}}} \bigg|_{\text{actual}} \\ \tilde{K}_{k_{\text{edge}}} &= \tilde{K}_{k_{\text{edge}}} \bigg|_{\text{actual}} \end{aligned} \quad (82)$$

where the subscript "edge" refers to conditions specified at η_{edge} , chosen to be outside the boundary layer (see Section 2.3). An additional constraint at the boundary layer edge which is necessary only when cubics are used is the requirement of zero slope, i.e.,

$$\begin{aligned} f''_{\text{edge}} &= 0 \\ H'_{\text{edge}} &= 0 \\ \tilde{K}'_{k_{\text{edge}}} &= 0 \end{aligned} \quad (83)$$

In addition to the specification of edge pressure, it is also possible to specify edge entropy and edge specie mass fractions to simulate the effects of entropy layer swallowing and nonequilibrium chemistry in the inviscid field. The techniques of Reference 4 are then used to establish the complete thermochemical gas state for nonisentropic, nonequilibrium expansions around a body of interest.

Initial profiles of f'' , H_T , and \tilde{K}_k are more difficult to establish for the general problem, therefore calculations are often started with reasonable assumed profiles far upstream of the region of interest so that effects of erroneous assumptions will die out. Another possibility for initially laminar problems is to assume a similar solution as a starting profile. This assumption reduces the

equations to ordinary differential equations at the starting point, which may be solved simultaneously for a set of profiles unique to the assumed edge and wall state. The similar solution is exact at a body stagnation point, therefore this option is particularly valuable for blunt body problems.

The wall boundary conditions allow the widest selection of options. The simplest combination is the straightforward assignment of velocities, enthalpy, and elemental concentrations at the wall:

$$\begin{array}{ll}
 f'_w = 0 & \text{no slip} \\
 f_w = f_w(\xi) & \text{specified } \rho_w v_w \\
 H_{T_w} = h_w(\xi) & \text{specified enthalpy of gas at the wall} \\
 \tilde{K}_{k_w} = \tilde{K}_{k_w}(\xi) & \text{specified wall gas elemental composition*}
 \end{array} \tag{84}$$

Wall temperatures may be used to find wall enthalpy in the above formulation. Also, wall mass diffusive fluxes of up to three individual injectants may be assigned in lieu of \tilde{K}_{k_w} and $\rho_w v_w$. With the values of the dependent variables all directly assigned in this manner, the boundary layer problem is uncoupled from the surface chemistry interaction.

The inclusion of surface material/boundary layer gas interaction chemistry in the boundary layer problem forms the second major set of wall boundary condition options. Using the surface thermochemistry techniques of Reference 4, it is possible to specify given mass fluxes of the (up to) three injectants at the wall and require chemical equilibrium between the injectants, the wall material, and the adjacent gas stream. In this instance, the values of H_{T_w} (i.e., T_w) and \tilde{K}_{k_w} are found by simultaneous solution of the local surface chemical equilibrium equations, surface mass balances, and the no-slip velocity boundary conditions. Alternatively, selected chemical reactions at the wall can be kinetically controlled

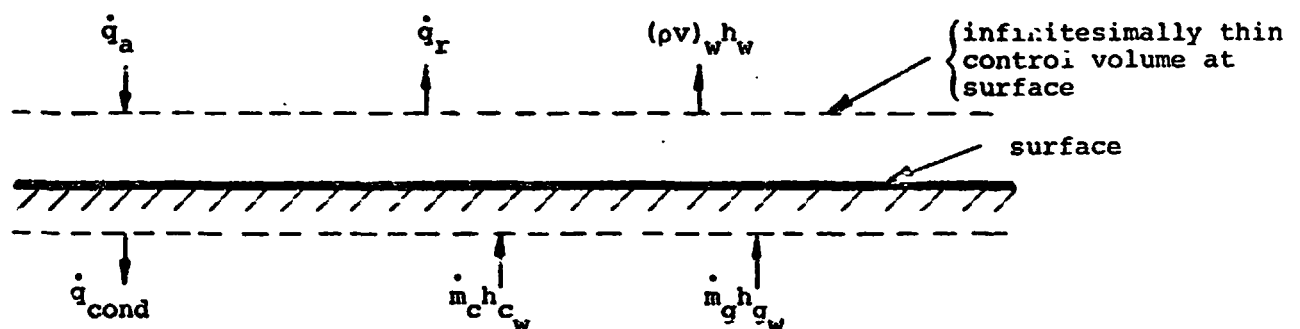
* It is physically unrealistic in most cases to assign \tilde{K}_{k_w} when diffusion coefficients are unequal since the contribution to \tilde{K}_{k_w} by $\rho_w v_w$ preferential diffusion of the various "elements" to the surface is not known a priori.

through Arrhenius-type rate law formulations (see sections 2.5 and 2.6) and included in the surface chemistry description.

In the use of this boundary layer technique in conjunction with in-depth charring ablation analyses, the chemically active injectants might result from the pyrolysis of an internally decomposing material, surface material combustion or phase change, and mechanical removal. A variation of this type of wall boundary condition is to specify the wall temperature or enthalpy and allow the surface chemistry calculations to compute the necessary $\rho_w v_w$ and \tilde{K}_w . In summary, the surface equilibrium wall boundary condition is

$$\begin{aligned} f'_w &= 0 && \text{no slip} \\ f_w &= f_w(\xi) && \text{specified } \rho_w v_w \\ H_{T_w} &= H_{T_w \text{ equil}} && \text{from surface equilibrium requirement} \\ \tilde{K}_w &= \tilde{K}_w \text{ equil} \end{aligned} \tag{85}$$

The final wall boundary condition category involves the use of a steady state energy balance at the surface. A general surface energy balance can best be understood by examination of a schematic representation of the energy fluxes to an ablating or nonablating ($\dot{m}_c = 0$) surface:



Summing terms,

$$\dot{m}_g h_{g_w} + \dot{m}_c h_{c_w} + \dot{q}_a - \dot{q}_r - (\rho v)_w h_w - \dot{q}_{\text{cond}} = 0 \quad (86)$$

which is valid in either a transient or steady-state situation. In general, an in-depth charring ablation solution would be needed to provide the conduction term \dot{q}_{cond} and the pyrolysis gas rate, \dot{m}_g . Under steady state conditions, the internal pyrolysis "front" and the charred surface are assumed to be receding at the same rate, therefore requiring that the energy conducted into the wall material must equal the enthalpy rise of the wall material and pyrolysis gases. In equation form

$$\dot{q}_{\text{cond}} - \dot{m}_c (h_{c_w} - h_c^0) - \dot{m}_g (h_{g_w} - h_g^0) = 0 \quad (87)$$

Substituting into Equation (86), the steady state energy balance becomes

$$\dot{q}_{a_w} - \dot{q}_{r_w} - (\rho v)_w h_w + \dot{m}_c h_c^0 + \dot{m}_g h_g^0 = 0 \quad (88)$$

In this equation, \dot{q}_{a_w} is the wall value of the energy flux defined in Equation (70), and is found in the course of the boundary layer solution. The surface equilibrium requirement is always used in conjunction with the steady state energy balance. Therefore, if one specifies the compositions and heats of formation of the pyrolysis gas and char materials, the simultaneous solution of the energy equation above and the surface chemistry relations mentioned earlier completely couples the boundary layer flow to the surface response. The steady state assumption is good even in transient situations for large ablation rates or small thermal diffusivity of the ablation material (Reference 17). In summary, the use of the steady state energy balance results in the following:

$$\begin{array}{ll} f'_w = 0 & \text{no slip} \\ H_{T_w} = H_{T_{w \text{ s.s.}}} & \text{steady state energy balance} \\ \left. \begin{array}{l} f_w = f_{w \text{ equil}} \\ \tilde{K}_{k_w} = \tilde{K}_{k_w \text{ equil}} \end{array} \right\} & \text{surface equilibrium requirement} \end{array} \quad (89)$$

2.5 HOMOGENEOUS CHEMISTRY

Chemical reaction rates are calculated using the procedures described in Reference 4. The m-th stoichiometric chemical reaction is written as

$$\sum_j \mu_{jm}^R N_j \rightleftharpoons \sum_j \mu_{jm}^P N_j \quad (90)$$

and its reaction rate can be expressed generally by

$$\bar{R}_m = k_{Fm} \left[\prod_j p_j^{\mu_{jm}^R} - \frac{1}{K_{Pm}} \prod_j p_j^{\mu_{jm}^P} \right] \quad (91)$$

The equilibrium constant K_p can be determined from the standard state free energy change, ΔG_m^O , to be

$$\ln K_{Pm} = - \frac{\Delta G_m^O}{RT} \equiv - \frac{1}{RT} \left[\sum_j (\mu_{jm}^P - \mu_{jm}^R) G_j^O \right] \quad (92)$$

and the reaction rate constant can be expressed in the Arrhenius form

$$k_{Fm} = B_m T^{A_m} \exp \left[- \frac{E_{am}}{RT} \right] \quad (93)$$

The standard state free energy is a function of temperature only and is obtained for each molecular species from

$$G_j^O = H_j^O - TS_j^O \quad (94)$$

where enthalpies are obtained relative to some chemical base state, often the elements in their most natural form at 298°K and one atmosphere (JANAF base state). If any other base state is consistently adopted, the ΔG_j^O will be unaffected.

The molar production rate of the specie i is then

$$r_i = \sum_m \left(\nu_{im}^P - \nu_{im}^R \right) \bar{R}_m \quad (95)$$

and the mass production rate is

$$\phi_i = r_i \mathcal{M}_i \quad (96)$$

For the third body chemical reactions, the particular third body specie influences the production rate however in many cases, only the probability coefficient B_m is different. In these cases, some reduction in the number of equations can be achieved by specifying a reference value of B_m and the relative efficiencies Γ_{m_i} of each third body. Then by omitting the third body from the stoichiometric reaction an effective reaction rate k'_F can be specified in terms of the molar concentrations n_i of the third bodies, i.e.,

$$k'_{F_m} = \left(\sum_i \Gamma_{m_i} n_i \right) B_{m_r} T_m^A \exp \left(-E_{a_m} / RT \right) \quad (97)$$

2.6 HETEROGENEOUS CHEMISTRY

Heterogeneous chemical reactions are specified in a form analogous to homogeneous reactions noting that the surface, on which the reactions take place, is a third body. The calculation procedure is then similar to that for homogeneous chemistry. Of particular interest are surface catalyzed recombination reactions. There are two popular forms for specifying the effectiveness of a surface as a catalyst for atomic recombination, namely, the catalytic efficiency and the catalycity k_w and is discussed in Section 4.2. The latter definition was chosen because it could be related to the reaction rate k_F and would therefore be consistent with the generalized surface chemistry calculation procedure. For instance, it is shown in the Appendix that for first order surface recombination

$$k_F = \frac{k_w}{RT} \quad (98)$$

2.7 NODAL POINT DISTRIBUTION REFIT OPTION

As will be shown in Section 5, nodal point distributions which are applicable to equilibrium boundary layers are generally also applicable to nonequilibrium boundary layers. However, because of the increase number of "elements" that must be considered in nonequilibrium calculations and the attendently large matrix that must be inverted in the Newton-Raphson calculation procedure, substantial reductions in machine time can be realized by reducing the number of nodes to a minimum. This is especially true when a lengthy laminar flow region is followed by transition to turbulent flow. In the laminar region, typically seven nodes are sufficient but in the turbulent region twelve to fourteen nodes are required. In addition a nodal distribution suitable for, say, the stagnation region may not be ideal for solutions far from the stagnation point. Thus a procedure was developed for adjusting the nodal point distribution and/or changing the number of nodal points to suit the local conditions where a solution is being sought.

The purpose of this procedure is to provide a means for maintaining an optimum nodal distribution for problems which include nonsimilar effects including transition to turbulence, blowing, entropy layer, pressure gradients, long stream-wise running lengths, etc. This readjustment is accomplished while preserving the fundamental characteristics of each profile, namely, basic profile shape, wall and edge derivatives, and integral properties. Potentially a number of bases may be identified for selecting nodal distributions and for making decisions relative to changing the existing distribution, e.g. mapping of any one of the velocity, temperature, and specie profiles. However, since adequate mapping of the velocity profile is the most commonly encountered problem, a selection criterion based on this parameter has been implemented, and the identification, evaluation and implementation of any other possible criteria has not been pursued at this time. Initially the selection criterion has been based upon maintaining a desired (specified) velocity ratio distribution across the layer; for nonsimilar turbulent flows then, for example, the nodal distribution will change as a function of distance to account for the changes in velocity profile shape as the turbulent layer develops. The decision to refit is made following a converged solution and is based on whether or not the newly calculated velocities vary by more than a selected ratio from the desired values.

The REFIT procedure is currently valid for all allowed curve fitting options across the boundary layer, i.e., all quadratics, quadratics with a final cubic and all cubics. It is also compatible with all of the entropy layer options. Finally as a result of the basic features of the REFIT option, it is possible to change the number of nodes used to describe the boundary layer. This latter capability has been programmed only for the case of transition from laminar to turbulent flow, as a means for eliminating the unnecessary and expensive extra nodes from laminar calculations. As such this option is limited to this application; however, potentially it may be programmed for more general application. The REFIT option is limited to a maximum of 15 nodes; however, as might be anticipated, the ability to maintain a more optimum distribution of nodes makes it possible to solve most problems using fewer nodes than normally required without REFIT. For example, for some long streamwise length, turbulent flows, it is either very difficult or impossible to estimate in advance the best distribution for the entire length using all 15 nodes. With REFIT, it is possible to achieve good results with minimal selection of desired velocity ratios using 12 nodes. Since solution times vary roughly as the number of nodes squared, this represents a saving of 40 percent in computer time, some of which is used in the refitting operation.

SECTION 3

INTEGRAL MATRIX SOLUTION PROCEDURE

The solution of the transformed boundary layer equations presented in Section 2 uses an integral matrix method which has been developed specifically for the solution of chemically reacting, nonsimilar, coupled boundary layers. A complete presentation of the integral matrix procedure was included in Reference 1, where solution of laminar flow problems was discussed. In the present effort, this technique has remained essentially unchanged, however new variables and equations have been added to describe the nonequilibrium aspects of the flow. The present discussion will therefore review only the highlights of the method, and the reader may refer to Reference 1 for more details.

In the integral matrix procedure, the primary dependent variables and their derivatives with respect to η are related by Taylor series expansions such that these dependent variables are represented by connected quadratics or cubics (either option is available). That is, f' , H_T , and \tilde{K}_k are expanded in Taylor series form and the series are truncated to reflect the proper polynomial representation. A nodal network is defined through the boundary layer and the Taylor series expansions are assumed valid between each set of nodes, with an additional requirement of continuous first and second derivatives (a spline fit). Primarily for convenience, the conservation equations are integrated across each "strip" (between nodal points) using a unity weighting function. The linear Taylor series expansions together with linear boundary conditions form a very sparse matrix which has to be inverted only once for a given problem. The nonlinear boundary layer equations and nonlinear boundary conditions are then linearized, the errors being driven to zero using Newton-Raphson iteration.

3.1 INTEGRAL STRIP EQUATIONS WITH SPLINED INTERPOLATION FUNCTIONS

Consider the boundary layer in the region of a given streamwise station s as being divided into $N-1$ strips connecting N nodal points. These nodal points

are designated by η_i where $i = 1$ at the wall and N at the edge of the boundary layer. Consider a function $p(\eta)$ which with all its derivatives is continuous in the neighborhood of the point $\eta = \eta_i$. Then, for any value of η in this neighborhood, $p(\eta)$ may be expressed in a Taylor series expansion as

$$p_{i+1} = p_i + p'_i \delta\eta + p''_i \frac{(\delta\eta)^2}{2} + p'''_i \frac{(\delta\eta)^3}{6} + p''''_i \frac{(\delta\eta)^4}{24} + \dots$$

where

$$\delta\eta = \eta_{i+1} - \eta_i \quad (100)$$

Conventional finite difference schemes, in effect, typically truncate the Taylor series after the first term and use the resulting expression to relate p' to p , etc., that is

$$p'_i = \frac{p_{i+1} - p_i}{\delta\eta} \quad (101)$$

Round-off error is then of order $(\delta\eta)^2$ and many nodes must be chosen to bring this value down to acceptable limits. One can achieve a reduction in the number of nodes for a given accuracy by employing a quadratic or cubic relation representing the function p over the interval of interest. This can be achieved by truncating the Taylor series after the third or fourth term. The cubic approximation will be used for the remainder of this discussion. The p_i can be considered to be any of f_i , f'_i , f''_i , f'''_i , $H_{T,i}$, $H'_{T,i}$, $H''_{T,i}$, $\tilde{K}_{k,i}$, $\tilde{K}'_{k,i}$, or $\tilde{K}''_{k,i}$. Since the highest derivatives of the dependent variables which appear in the boundary layer equations are f'''_i , $H''_{T,i}$ and $\tilde{K}''_{k,i}$, it is reasonable to truncate the series at the next highest derivative and to consider that derivative as being constant between η_i and η_{i+1} , that is,

$$\begin{aligned} {}_i f'''_{i+1} &= \frac{f'''_{i+1} - f'''_i}{\delta\eta} \\ {}_i H''_{T,i+1} &= \frac{H''_{T,i+1} - H''_{T,i}}{\delta\eta} \\ {}_i \tilde{K}''_{k,i+1} &= \frac{\tilde{K}''_{k,i+1} - \tilde{K}''_{k,i}}{\delta\eta} \end{aligned} \quad (102)$$

Thus, rather than using finite difference approximations similar to Equation (101) which are substituted directly into the governing differential equations, a set of linear relations between the dependent variables and their derivatives is obtained and is solved simultaneously with the governing differential equations. These linear relations are of the form

$$- f_{i+1} + f_i + f'_i \delta\eta + f''_i \frac{(\delta\eta)^2}{2} + f'''_i \frac{(\delta\eta)^3}{6} + f_{i+1} \frac{(\delta\eta)^3}{24} = 0 \quad (103)$$

$$- p_{i+1} + p_i + p'_i \delta\eta + p''_i \frac{(\delta\eta)^2}{2} + p_{i+1} \frac{(\delta\eta)^2}{6} = 0 \quad (104)$$

$$- p'_{i+1} + p'_i + p''_i \frac{\delta\eta}{2} + p'_{i+1} \frac{\delta\eta}{2} = 0 \quad (105)$$

where in Equations (104) and (105) the p_i represents f'_i , H_{T_i} , and each of the K sets of \tilde{K}_{k_i} .

Notice that f' has been taken to be a cubic over each strip, rather than the stream function, f , since it was desired to represent velocity ($u = u_1 f' / \alpha_H$) with the cubic. Equations (103) through (105) above, when written for each adjacent pair of nodes, give $(3 + 2K)(N - 1)$ simultaneous algebraic equations for the $N(4 + 3K) + 1$ unknowns, f_n , f'_n , f''_n , f'''_n , α_H , H_T , H'_T , H''_T , \tilde{K}_k , \tilde{K}'_k , \tilde{K}''_k at each streamwise station, where K is the number of elemental species.* The Taylor series equations are written for only $K-1$ species since the overall mass balance equation supplies the remaining elemental concentration. Additional relations must come from the governing differential equations and the boundary conditions. It is important to note that the f , f' , etc., are treated as individual variables related by algebraic equations. It is also important to note that the coefficients in Equations (103) through (105) are functions of $\delta\eta$ only; therefore, this portion of the resulting matrix need be inverted only once for a given problem.

*The mixing length is not included in this variables count since mixing length (as well as ϵ_M in the wake region) is treated as a state property.

The conservation Equations (50), (65), and (68) contain streamwise derivative or "nonsimilar" terms. In the present solution technique, two or three point finite difference formulas are considered sufficient to express these derivatives, since gradients in this direction are not severe. As in Reference 1

$$2 \left[\frac{d(\)}{d(\ln \xi)} \right]_l = d_0(\)_l + d_1(\)_{l-1} + d_2(\)_{l-2} \quad (106)$$

where $(\)_{l-1}$ refers to the previous streamwise station,

$$d_0 = \frac{2}{\Delta_{l-1}}, \quad d_1 = -\frac{2}{\Delta_{l-1}}, \quad d_2 = 0 \quad (107)$$

for two-point difference and

$$d_0 = 2 \frac{\Delta_{l-1} + \Delta_{l-2}}{\Delta_{l-1} \Delta_{l-2}}, \quad d_1 = -2 \frac{\Delta_{l-2}}{\Delta_{l-1} \Delta_{l-2}}, \quad d_2 = 2 \frac{\Delta_{l-1}}{\Delta_{l-2} \Delta_{l-1} \Delta_{l-2}} \quad (108)$$

for three-point difference where typically

$$\Delta_{l-1} = \ln \xi_l - \ln \xi_{l-1} = \ln(\xi_l / \xi_{l-1}) \quad (109)$$

The three-point difference relation is generally used unless a similar solution is desired (in which case $d_0 = d_1 = d_2 = 0$) or unless the point in question is the first point after either (1) a similar solution or (2) a discontinuity (e.g., where the body changes shape abruptly, or where mass injection is suddenly terminated).

The next step in the treatment of the conservation equations is their integration across the boundary layer "strips". The primary reason for this integration is to simplify the η -derivative terms in the energy and species conservation equations, since it is not convenient to express the complex q_k^* and j_k^* terms in derivative form. The solution can actually proceed very nicely without integrating across strips (see Reference 8) without any noticeable change

in speed, accuracy, or stability for simplified problems such as incompressible, nonreacting flows. The weighting function for integration between nodes in this integral method is unity. In the terminology of the general method of integral relations, where integrals are carried from 0 to ∞ in η (Reference 18), a square wave weighting function is used which is unity across the strip in question and zero elsewhere. The equations are then integrated N-1 times with the square wave applied to each strip in succession. Using the momentum equation as an example, the integration from i-1 to i results in

$$\begin{aligned} \int_{i-1}^i f f'' d\eta + \left[\frac{t(C + \bar{\epsilon}_M)}{\alpha_H} f'' \right]_{i-1}^i + \beta \alpha_H^2 \int_{i-1}^i \frac{p_1}{\rho} d\eta - \beta \int_{i-1}^i f'^2 d\eta \\ = \int_{i-1}^i f' (d_0 f' + d_1 f'_{l-1} + d_2 f'_{l-2}) d\eta - \int_{i-1}^i f'^2 \left[d_0 \ln \alpha_H \right. \\ \left. + d_1 (\ln \alpha_H)_{l-1} + d_2 (\ln \alpha_H)_{l-2} \right] d\eta - \int_{i-1}^i f'' (d_0 f + d_1 f_{l-1} \\ + d_2 f_{l-2}) d\eta \end{aligned} \quad (110)$$

The Taylor series approximations introduced earlier can also be used to express the integral terms above. As demonstrated in Reference 1, the term $\int_{i-1}^i f' p d\eta$ becomes

$$\int_{i-1}^i f' p d\eta = f'_i X P_1 + f''_i X P_2 + f'''_i X P_3 + f^{(4)}_i X P_4 \quad (111)$$

where

$$\begin{aligned} X P_1 &= \delta\eta \left(p_i - p'_i \frac{\delta\eta}{2} + p''_i \frac{(\delta\eta)^2}{8} + p'''_i \frac{(\delta\eta)^3}{24} \right) \\ X P_2 &= -(\delta\eta)^2 \left(\frac{p_i}{2} - p'_i \frac{\delta\eta}{3} + p''_i \frac{11(\delta\eta)^2}{120} + p'''_i \frac{(\delta\eta)^3}{30} \right) \\ X P_3 &= (\delta\eta)^3 \left(\frac{p_i}{8} - p'_i \frac{11(\delta\eta)}{120} + p''_i \frac{11(\delta\eta)^2}{420} + p'''_i \frac{5(\delta\eta)^3}{504} \right) \\ X P_4 &= (\delta\eta)^4 \left(\frac{p_i}{24} - p'_i \frac{\delta\eta}{30} + p''_i \frac{5(\delta\eta)^2}{504} + p'''_i \frac{(\delta\eta)^3}{252} \right) \end{aligned} \quad (112)$$

This technique is used to rewrite each of the integral terms in Equation (110) above of the form $\int_{i-1}^i f' p \, d\eta$. The remaining integral term in the momentum equation, $\int_{i-1}^i (\rho_1/\rho) d\eta$ is evaluated by approximating these functions as cubics over the strip and integrating directly. This yields

$$\int_{i-1}^i \frac{\rho_1}{\rho} d\eta = \left(\frac{\rho_1}{\rho} + \frac{\rho_1}{\rho_{i-1}} \right) \frac{\delta\eta}{2} + \left(\frac{\rho_1 \rho_1'}{\rho_1^2} - \frac{\rho_1 \rho_{i-1}'}{\rho_{i-1}^2} \right) \frac{\delta\eta^2}{12} \quad (113)$$

The production term is assumed to vary linearly across the strip so that the integral of ϕ_K/ρ is

$$\int_{i-1}^i \frac{\phi_K}{\rho} dy = \left[\left(\frac{\phi_K}{\rho} \right)_i + \left(\frac{\phi_K}{\rho} \right)_{i-1} \right] \frac{\delta\eta}{2} \quad (114)$$

These approximations are not quite as good as the approximations for f' , H_T and \tilde{K}_K since continuity of derivatives is not guaranteed at the nodal point.

Direct substitution of these approximations for integral terms into the governing equations results in the following forms.

Momentum

$$\begin{aligned} & \left[\frac{t(C + \tilde{E}_M)}{a_H} f'' + f' \left((1 + d_0) f + d_1 f_{\ell-1} + d_2 f_{\ell-2} \right) \right]_{i-1}^i \\ & + \beta a_H^2 \left[\left(\frac{\rho_1}{\rho_i} + \frac{\rho_1}{\rho_{i-1}} \right) \frac{\delta\eta}{2} + \left(\frac{\rho_1 \rho_1'}{\rho_i^2} - \frac{\rho_1 \rho_{i-1}'}{\rho_{i-1}^2} \right) \frac{(\delta\eta)^2}{12} \right] \\ & - \left(1 + \beta + d_0 - \frac{d_1 a_{H_{\ell-1}} + d_2 a_{H_{\ell-2}}}{a_H} \right) \left[f_i' X P_1 + f_i'' X P_2 \right. \\ & \left. + f_i''' X P_3 + f_{i-1}''' X P_4 \right]_{p_i=f_i'} - 2 \left[f_i' Z P_1 + f_i'' Z P_2 + f_i''' Z P_3 \right. \\ & \left. + f_{i-1}''' Z P_4 \right]_{p_i=f_i'} = 0 \end{aligned} \quad (115)$$

Energy

$$\begin{aligned}
 & \left[t(-q_a^* + q_r^*) + H_T \left((1 + d_0) f + d_1 f_{l-1} + d_2 f_{l-2} \right) \right]_{i-1}^i \\
 & - (1 + 2d_0) \left[f_i^I X P_1 + f_i^{II} X P_2 + f_i^{III} X P_3 + f_{i-1}^{IV} X P_4 \right]_{P_i = H_{T_i}} \\
 & - \left[f_i^I Z P_1 + f_i^{II} Z P_2 + f_i^{III} Z P_3 + f_{i-1}^{IV} Z P_4 \right]_{P_i = H_{T_i}} \\
 & - \left[H_{T_i} Z P_1 + H_{T_i}^I Z P_2 + H_{T_i}^{II} Z P_3 + H_{T_{i-1}}^{IV} Z P_4 \right]_{P_i = f_i^I} = 0 \quad (116)
 \end{aligned}$$

"Elemental" Species

$$\begin{aligned}
 & \left[t \left(\frac{\tilde{\epsilon}_M}{\alpha_H S c_t} \tilde{K}_k^I - j_k^* \right) + \tilde{K}_k \left((1 + d_0) f + d_1 f_{l-1} + d_2 f_{l-2} \right) \right]_{i-1}^i \\
 & + \alpha_H \left[\left(\phi_{k_i} + \phi_{k_{i-1}} \right) \frac{\delta \eta}{2} - \left(\phi_{k_i}^I - \phi_{k_{i-1}}^I \right) \frac{(\delta \eta)^2}{12} \right] \\
 & - (1 + 2d_0) \left[f_i^I X P_1 + f_i^{II} X P_2 + f_i^{III} X P_3 + f_{i-1}^{IV} X P_4 \right]_{P_i = \tilde{K}_{k_i}} \\
 & - \left[f_i^I Z P_1 + f_i^{II} Z P_2 + f_i^{III} Z P_3 + f_{i-1}^{IV} Z P_4 \right]_{P_i = \tilde{K}_{k_i}} \\
 & - \left[\tilde{K}_{k_i} Z P_1 + \tilde{K}_{k_i}^I Z P_2 + \tilde{K}_{k_i}^{II} Z P_3 + \tilde{K}_{k_{i-1}}^{IV} Z P_4 \right]_{P_i = f_i^I} = 0 \quad (117)
 \end{aligned}$$

The following definitions are necessary:

$$\begin{aligned}
 Z P_1 &= \delta \eta \left(Y P_1 - Y P_2 \frac{\delta \eta}{2} + Y P_3 \frac{(\delta \eta)^2}{8} + Y P_4 \frac{(\delta \eta)^2}{24} \right) \\
 Z P_2 &= -(\delta \eta)^2 \left(\frac{Y P_1}{2} - Y P_2 \frac{\delta \eta}{3} + Y P_3 \frac{11(\delta \eta)^2}{120} + Y P_4 \frac{(\delta \eta)^2}{30} \right) \\
 Z P_3 &= (\delta \eta)^3 \left(\frac{Y P_1}{8} - Y P_2 \frac{11\delta \eta}{120} + Y P_3 \frac{11(\delta \eta)^2}{420} + Y P_4 \frac{5(\delta \eta)^2}{504} \right) \\
 Z P_4 &= (\delta \eta)^3 \left(\frac{Y P_1}{24} - Y P_2 \frac{\delta \eta}{30} + Y P_3 \frac{5(\delta \eta)^2}{504} + Y P_4 \frac{(\delta \eta)^2}{252} \right) \quad (118)
 \end{aligned}$$

with

$$\begin{aligned}
 YP_1 &= d_1 p_{l-1,i} + d_2 p_{l-2,i} \\
 YP_2 &= d_1 p'_{l-1,i} + d_2 p'_{l-2,i} \\
 YP_3 &= d_1 p''_{l-1,i} + d_2 p''_{l-2,i} \\
 YP_4 &= d_1 p'''_{l-1,i-1} + d_2 p'''_{l-2,i-1}
 \end{aligned}
 \tag{119}$$

and p_i is defined adjacent to the brackets in each term that uses these definitions.

The conservation equations provide $(K+1)(N-1)$ more equations for the $N(3K+4)+1$ unknowns, thereby closing the problem. However, before discussing how this set of algebraic equations is solved, Section 3.2 describes in detail how the mixing length differential equation is solved.

3.2 SOLUTION OF THE MIXING LENGTH EQUATION

The mixing length equation is a first order linear differential equation whose solution can be written directly in general terms. The differential equation is

$$\frac{d\tilde{l}}{d\eta} = \frac{\alpha_H \rho_1 \delta \sqrt{\tau/\rho}}{y_a^+ \mu} (K\alpha_H \eta - \tilde{l})
 \tag{63}$$

Defining

$$P(\eta) \equiv \frac{\alpha_H \rho_1 \delta \sqrt{\tau/\rho}}{y_a^+ \mu}
 \tag{120}$$

results in

$$\frac{d\tilde{l}}{d\eta} = (K\alpha_H \eta - \tilde{l})P
 \tag{121}$$

The solution to this equation is

$$\tilde{L} = K\alpha_H \left[\eta - \frac{\int_0^\eta e^{\int_0^{\eta'} P d\eta'} d\eta'}{e^{\int_0^\eta P d\eta'}} \right] \quad (122)$$

The remaining problem is to evaluate the integral terms. Defining

$$L(\eta) \equiv \frac{\int_0^\eta e^{\int_0^{\eta'} P d\eta'} d\eta'}{e^{\int_0^\eta P d\eta'}} \quad (123)$$

yields

$$\tilde{L} = K\alpha_H (\eta - L) \quad (124)$$

Reference 2 presents a complete description of the technique used to evaluate $L(\eta)$. In essence, $P(\eta)$ is assumed to vary linearly over the interval η_{i-1} to η_i , and the integrals are expressed in a more tractable form. The final expression is

$$L_i = BL_{i-1} + A \left\{ D_w \left(\frac{AP_i}{2} \right) - BD_w \left(\frac{AP_{i-1}}{2} \right) \right\} \quad (125)$$

where

$$A \equiv \left[\frac{2\Delta\eta_i}{P_i - P_{i-1}} \right]^{\frac{1}{2}} \quad (126)$$

$$B \equiv e^{-\Delta\eta_i \left[\frac{P_i + P_{i-1}}{2} \right]} \quad (127)$$

$$\Delta\eta_i \equiv \eta_i - \eta_{i-1} \quad (128)$$

$$D_w(\cdot) = e^{-(\cdot)^2} \int_0^{(\cdot)} e^{+y^2} dy \quad (129)$$

The Dawson Integral, $D_w(\)$, can be evaluated from tables (Reference 19) or by a series method. A series evaluation method is used in the present analysis. Thus, combining Equations (124) and (125), an explicit recursion formula for mixing length at each node is obtained. This mixing length is a function of local shear, viscosity, and density through the variation of $P(\)$, and is re-evaluated at each node on each iteration during the course of a solution.

3.3 NEWTON-RAPHSON ITERATION FOR A SOLUTION

A complete description of the Newton-Raphson iteration procedure as applied to the laminar equations of motion was given in Reference 1. Since the procedure is basically unchanged with the addition of nonequilibrium chemistry it will be reviewed only briefly here, with emphasis on the recent additions.

To illustrate the Newton-Raphson method, consider two simultaneous non-linear algebraic equations

$$F(x, y) = 0 \quad G(x, y) = 0 \quad (130)$$

the solution for which is given by $x = \bar{x}$, $y = \bar{y}$. Define x_m and y_m as the values of x and y for the m^{th} iteration. The desired solution $f(\bar{x}, \bar{y})$ can be expressed in a Taylor series expansion

$$\begin{aligned} 0 = F(\bar{x}, \bar{y}) &= F(x_m, y_m) + (\bar{x} - x_m) \frac{\partial F(x_m, y_m)}{\partial x} \\ &+ (\bar{y} - y_m) \frac{\partial F(x_m, y_m)}{\partial y} + \dots \\ 0 = G(\bar{x}, \bar{y}) &= G(x_m, y_m) + (\bar{x} - x_m) \frac{\partial G(x_m, y_m)}{\partial x} \\ &+ (\bar{y} - y_m) \frac{\partial G(x_m, y_m)}{\partial y} + \dots \end{aligned} \quad (131)$$

The Newton-Raphson method consists of replacing (x, y) by (x_{m+1}, y_{m+1}) on the hand side of these expressions and neglecting nonlinear terms in $x_{m+1} - x_m$ and

$y_{m+1} - y_m$. This yields the set of simultaneous equations

$$\begin{aligned} \Delta x_m \frac{\partial F(x_m, y_m)}{\partial x} + \Delta y_m \frac{\partial F(x_m, y_m)}{\partial y} &= -F(x_m, y_m) \\ \Delta x_m \frac{\partial G(x_m, y_m)}{\partial x} + \Delta y_m \frac{\partial G(x_m, y_m)}{\partial y} &= -G(x_m, y_m) \end{aligned} \quad (132)$$

or in matrix form

$$\begin{bmatrix} \frac{\partial F(x_m, y_m)}{\partial x} & \frac{\partial F(x_m, y_m)}{\partial y} \\ \frac{\partial G(x_m, y_m)}{\partial x} & \frac{\partial G(x_m, y_m)}{\partial y} \end{bmatrix} \begin{bmatrix} \Delta x_m \\ \Delta y_m \end{bmatrix} = \begin{bmatrix} -F(x_m, y_m) \\ -G(x_m, y_m) \end{bmatrix} \quad (133)$$

where

$$\Delta x_m \equiv x_{m+1} - x_m \quad \Delta y_m \equiv y_{m+1} - y_m \quad (134)$$

The Δx_m and Δy_m are the corrections to be added to x_m and y_m , respectively, to yield the values of the dependent variables for the $m + 1^{\text{th}}$ iteration. Here $F(x_m, y_m)$ and $G(x_m, y_m)$ are values of the original functions $F(x, y)$ and $G(x, y)$ evaluated for $x = x_m$ and $y = y_m$. As the corrections approach zero, the $F(x_m, y_m)$ and $G(x_m, y_m)$ approach zero. Hence, it is appropriate to look upon these as errors associated with the original Equation (130). It is apparent that this procedure can be extended to an arbitrary number of functions and a corresponding number of primary variables.

For the purpose of the present analysis, it has been found most convenient to consider the primary variables as $f_i, f'_i, f''_i, f'''_i, H_{T_i}, H'_{T_i}, q''_{T_i}, \tilde{K}_{k_i}, \tilde{K}'_{k_i}, \tilde{K}''_{k_i}$, and α_H . This amounts to $(3K + 4)N + 1$ unknowns where N is the number of nodes and K is the number of elemental species to be considered in the boundary layer. Recounting the number of equations, we have

	<u>Eqn. Numbers</u>	<u>No. of Equations</u>
Taylor series expansions	(103) - (105)	$(N - 1) [5 + 2(K - 1)]$
Boundary layer equations	(115) - (117)	$(N - 1) (K + 1)$
Boundary conditions	(82), (83), (84) or equivalent	$3K + 4$
α_H definition	(44)	$\frac{1}{N(3K + 4) + 1}$
Total		

Other secondary variables such as ϵ , ρ , T , etc. are expressed in terms of those listed above. The corrections in these secondary variables are therefore found in terms of the corrections to the primary variables.

The use of the Newton-Raphson technique for the current set of equations requires the evaluation of the partial derivatives of each equation with respect to each variable. The partial derivatives of the Taylor series equations and linear boundary conditions are exactly the same as in Reference 1. The derivatives of the conservation equations are:

Momentum

$$\begin{aligned}
 & \left[\frac{t(C + \bar{\epsilon}_M) f''}{\alpha_H} \left(\frac{\Delta f''}{f''} + \frac{\Delta C}{C} + \frac{\Delta \bar{\epsilon}_M}{\bar{\epsilon}_M} - \frac{\Delta \alpha_H}{\alpha_H} + \frac{\Delta t}{t} \right) + \left[(1 + d_0) f + d_1 f_{\ell-1} + d_2 f_{\ell-2} \right] f' \right. \\
 & \quad \left. + f' (1 + d_0) \Delta f \right]_{i-1}^i - \beta \alpha_H^2 \frac{\rho_1}{\rho_i^2} \frac{\delta \eta}{2} \left\{ \left(1 + \frac{\delta \eta}{3} \frac{\rho_1'}{\rho_i} \right) \Delta \rho_i - \frac{\delta \eta}{6} \Delta \rho_i' \right. \\
 & \quad \left. + \left(\frac{\rho_i}{\rho_{i-1}} \right)^2 \left[\left(1 - \frac{\delta \eta}{3} \frac{\rho_{i-1}'}{\rho_{i-1}} \right) \Delta \rho_{i-1} + \frac{\delta \eta}{6} \Delta \rho_{i-1}' \right] \right\} + \beta \alpha_H \delta \eta \frac{\rho_1}{\rho_i} \left[1 + \frac{\rho_i}{\rho_{i-1}} \right. \\
 & \quad \left. + \frac{\delta \eta}{6} \left(\frac{\rho_i'}{\rho_i} - \frac{\rho_i}{\rho_{i-1}} \frac{\rho_{i-1}'}{\rho_{i-1}} \right) \right] \Delta \alpha_H - \left[1 + \beta + d_0 - \left(\frac{d_1 \alpha_{H \ell-1} + d_2 \alpha_{H \ell-2}}{\alpha_H} \right) \right]
 \end{aligned}$$

$$\begin{aligned}
& \times \left[f_1' \Delta XP_1 + f_1'' \Delta XP_2 + f_1''' \Delta XP_3 + f_{1-1}''' \Delta XP_4 + XP_1 \Delta f_1' + XP_2 \Delta f_1'' \right. \\
& \left. + XP_3 \Delta f_1''' + XP_4 \Delta f_{1-1}''' \right]_{P_i=f_1'} - \left(\frac{d_1 \alpha_{H_{l-1}} + d_2 \alpha_{H_{l-2}}}{\alpha_H^2} \right) \left[f_1' XP_1 + f_1'' XP_2 \right. \\
& \left. + f_1''' XP_3 + f_{1-1}''' XP_4 \right]_{P_i=f_1'} \Delta \alpha_H - 2 \left[ZP_1 \Delta f_1' + ZP_2 \Delta f_1'' + ZP_3 \Delta f_1''' \right. \\
& \left. + ZP_4 \Delta f_{1-1}''' \right]_{P_i=f_1'} = - \text{ERROR} \quad (135)
\end{aligned}$$

where the ERROR is given by the left-hand side of Equation (115) evaluated for m^{th} iteration.

Energy

$$\begin{aligned}
& \left[t(-\Delta q_a^* + \Delta q_r^*) + (-q_a^* + q_r^*) \Delta t + \left((1 + d_0) f + d_1 f_{l-1} + d_2 f_{l-2} \right) \Delta H_T \right. \\
& \left. + H_T (1 + d_0) \Delta f \right]_{i-1}^i - (1 + 2d_0) \left[f_i' \Delta XP_1 + f_i'' \Delta XP_2 + f_i''' \Delta XP_3 \right. \\
& \left. + f_{i-1}''' \Delta XP_4 + XP_1 \Delta f_i' + XP_2 \Delta f_i'' + XP_3 \Delta f_i''' + XP_4 \Delta f_{i-1}''' \right]_{P_i=H_{T_i}} - \left[ZP_1 \Delta f_i' \right. \\
& \left. + ZP_2 \Delta f_i'' + ZP_3 \Delta f_i''' + ZP_4 \Delta f_{i-1}''' \right]_{P_i=H_{T_i}} - \left[ZP_1 \Delta H_{T_i} + ZP_2 \Delta H_{T_i} \right. \\
& \left. + ZP_3 \Delta H_{T_i}'' + ZP_4 \Delta H_{T_i-1}'' \right]_{P_i=f_i'} = - \text{ERROR} \quad (136)
\end{aligned}$$

where the ERROR is given by the left-hand side of Equation (116) for the m^{th} iteration and Δq_a^* is given by

$$\begin{aligned} \Delta q_a^* = - \left\{ \frac{(C + \tilde{\epsilon}_M) f' f'' u_1^2}{\alpha_H^3} \left(\frac{\Delta C}{C} + \frac{\Delta \tilde{\epsilon}_M}{\tilde{\epsilon}_M} + \frac{\Delta f'}{f'} + \frac{\Delta f''}{f''} - 3 \frac{\Delta \alpha_H}{\alpha_H} \right) + \frac{C C_P T'}{\alpha_H P_r} \left(\frac{\Delta C}{C} \right. \right. \\ \left. \left. + \frac{\Delta \bar{C}_P}{C} + \frac{\Delta T'}{T'} - \frac{\Delta \alpha_H}{\alpha_H} - \frac{\Delta P_r}{P_r} \right) + \frac{\tilde{\epsilon}_M \bar{C}_P T'}{\alpha_H P_r t} \left(\frac{\Delta \tilde{\epsilon}_M}{\tilde{\epsilon}_M} + \frac{\Delta C_P}{\bar{C}_P} + \frac{\Delta T'}{T'} - \frac{\Delta \alpha_H}{\alpha_H} \right) \right. \\ \left. + \frac{C}{\alpha_H \bar{S} C} \left[\tilde{h}' - \left(\bar{C}_P + \frac{c_t^2 R}{\mu_1 \mu_2} \right) T' + c_t R T \mu_3' + (\tilde{h} - h + c_t R T \mu_3) \mu_4' \right] \left[\frac{\Delta C}{C} \right. \right. \\ \left. \left. - \frac{\Delta \alpha_H}{\alpha_H} - \frac{\Delta \bar{S} C}{\bar{S} C} \right] + \frac{\tilde{\epsilon}_M}{\alpha_H \bar{S} C t} \left(h' - \bar{C}_P T' \right) \left[\frac{\Delta \tilde{\epsilon}_M}{\tilde{\epsilon}_M} - \frac{\Delta \alpha_H}{\alpha_H} \right] + \frac{C}{\alpha_H \bar{S} C} \left[\Delta \tilde{h}' \right. \right. \\ \left. \left. - \left(\bar{C}_P + \frac{c_t^2 R}{\mu_1 \mu_2} \right) \Delta T' - T' \Delta \bar{C}_P + \frac{c_t^2 R T}{(\mu_1 \mu_2)^2} \Delta (\mu_1 \mu_2) + c_t R T \mu_3' \left(\frac{\Delta T}{T} \right. \right. \right. \\ \left. \left. + \frac{\Delta \mu_3'}{\mu_3'} \right) + (\tilde{h} - h + c_t R T \mu_3) \Delta \mu_4' + \mu_4' \left(\Delta \tilde{h} - \Delta h + c_t R T \mu_3 \left(\frac{\Delta \mu_3}{\mu_3} \right. \right. \right. \\ \left. \left. + \frac{\Delta T}{T} \right) \right) \right] + \frac{\tilde{\epsilon}_M}{\alpha_H \bar{S} C t} \left[\Delta h' - \bar{C}_P \Delta T' - T' \Delta \bar{C}_P \right] \left. \right\} \quad (137) \end{aligned}$$

"Elemental" Species

$$\begin{aligned} \left[-t \Delta j_k^* - j_k^* \Delta t + \frac{\tilde{\epsilon}_M \tilde{K}_k t}{\alpha_H \bar{S} C t} \left(\frac{\Delta \tilde{K}_k}{\tilde{K}_k} - \frac{\Delta \alpha_H}{\alpha_H} + \frac{\Delta \tilde{\epsilon}_M}{\tilde{\epsilon}_M} + \frac{\Delta t}{t} \right) + \left((1 + d_0) f + d_1 f_{l-1} \right. \right. \\ \left. \left. + d_2 f_{l-2} \right) \Delta \tilde{K}_k + \tilde{K}_k (1 + d_0) \Delta f \right]_{i-1}^i \end{aligned}$$

$$\begin{aligned}
& + \alpha_H \frac{\delta \eta}{2} \left[\Delta \left(\frac{\phi_K}{\rho} \right)_i + \Delta \left(\frac{\phi_K}{\rho} \right)_{i-1} \right] + \frac{\delta \eta}{2} \left[\left(\frac{\phi_K}{\rho} \right)_i + \left(\frac{\phi_K}{\rho} \right)_{i-1} \right] \Delta \alpha_H \\
& - (1 + 2d_0) \left[f_i' \Delta XP_1 + f_i'' \Delta XP_2 + f_i''' \Delta XP_3 + f_{i-1}''' \Delta XP_4 + XP_1 \Delta f_i' \right. \\
& \left. + XP_2 \Delta f_i'' + XP_3 \Delta f_i''' + XP_4 \Delta f_{i-1}''' \right]_{p_i = \tilde{K}_{k_i}} - \left[ZP_1 \Delta f_i' + ZP_2 \Delta f_i'' \right. \\
& \left. + ZP_3 \Delta f_i''' + ZP_4 \Delta f_{i-1}''' \right]_{p_i = \tilde{K}_{k_i}} - \left[ZP_1 \Delta \tilde{K}_{k_i} + ZP_2 \Delta \tilde{K}_{k_i}' + ZP_3 \Delta \tilde{K}_{k_i}'' \right. \\
& \left. + ZP_4 \Delta \tilde{K}_{k_{i-1}}''' \right]_{p_i = f_i'} = - \text{ERROR} \tag{138}
\end{aligned}$$

where the ERROR is given by the left-hand side of Equation (117) evaluated for the m^{th} iteration and Δj_k^* 's given by

$$\begin{aligned}
\Delta j_k^* = & - \frac{C}{\alpha_H \overline{Sc}} \left[\left(\tilde{z}_k' + (\tilde{z}_k - \tilde{K}_k) \mu_4' \right) \left(\frac{\Delta C}{C} - \frac{\Delta \alpha_H}{\alpha_H} - \frac{\Delta \overline{Sc}}{\overline{Sc}} \right) \right. \\
& \left. + \Delta \tilde{z}_k' + (\tilde{z}_k - \tilde{K}_k) \Delta \mu_4' + \mu_4' (\Delta \tilde{z}_k - \Delta \tilde{K}_k) \right] \tag{139}
\end{aligned}$$

The technique of relating corrections on secondary variables such as C , O , T , Pr , etc., to corrections in primary variables was fully explained in Reference 1. The same techniques are used for the corrections Δt and $\Delta \tilde{\epsilon}_M$ and $\Delta(\phi_K/\rho)$.

Once the correction coefficients (partial derivatives with respect to each primary variable) for each equation at each nodal point are found, they are arranged in matrix form for further manipulation. The order of the primary variables and the order of the equations is of some importance in the matrix formulation. It is most convenient to divide the variables into "linear" (symbol L) and "nonlinear" (symbol NL) sets, namely

$$\begin{bmatrix} \overline{AL} & \overline{BL} \\ \overline{ANL} & \overline{BNL} \end{bmatrix} \begin{bmatrix} \overline{\Delta VL} \\ \overline{\Delta VNL} \end{bmatrix} = - \begin{bmatrix} \overline{EL} \\ \overline{ENL} \end{bmatrix} \tag{140}$$

where the linear equations are the Taylor series equations and some of the boundary conditions. The purpose of the partitioning is to allow operations on sections of the coefficient matrix which result in significant simplification of the overall inversion. In particular, since the coefficients of the linear equations are all constant or functions of the fixed nodal spacing, this portion of the matrix (the AL portion) can be diagonalized once and for all in any given problem. In essence, the corrections on the linear variables ΔV_L are always expressed in terms of the nonlinear variable corrections ΔV_{NL} . The choice of linear and nonlinear labels for the variables is somewhat arbitrary, but care must be taken that the AL matrix not be singular. It has been found convenient to arrange the variables into the linear and nonlinear groups as follows:

$\Delta V_{L_F} (\Delta f_2, \Delta f_3, \dots, \Delta f_n, \Delta f_2'', \Delta f_3'', \dots, \Delta f_n'', \Delta f_1', \Delta f_2', \dots, \Delta f_n')$; $\Delta V_{L_H} (\Delta H_T, \Delta H_T', \dots, \Delta H_T'', \Delta H_T''', \dots, \Delta H_T^{(n)})$; and $K-1$ sets of $\Delta V_{L_K} (\Delta \tilde{K}_k, \Delta \tilde{K}_k', \Delta \tilde{K}_k'', \dots, \Delta \tilde{K}_k^{(n)})$. The nonlinear variables are then arranged in the following order: $\Delta V_{NL_F} (\Delta \alpha_H, \Delta f_w, \Delta f_w'', \Delta f_1', \Delta f_2', \dots, \Delta f_n')$; $\Delta V_{NL_H} (\Delta H_T', \Delta H_T'', \dots, \Delta H_T^{(n)})$; and $K-1$ sets of $\Delta V_{NL_K} (\Delta \tilde{K}_k', \Delta \tilde{K}_k'', \Delta \tilde{K}_k''', \dots, \Delta \tilde{K}_k^{(n)})$. The order of the linear equations in the present matrix procedure is:

<u>No. of Equations</u>	<u>Description of Equations</u>
3N-2	Linear Boundary conditions and Taylor series for f, f', f'', f'''
2N	Linear boundary conditions and Taylor series for H_T, H_T', H_T''
(K - 1) (2N)	Linear boundary conditions and Taylor series for K_k, K_k', K_k''

The nonlinear equations are sequenced as follows:

<u>No. of Equations</u>	<u>Description of Equations</u>
4	Nonlinear boundary conditions and α_H constraint
N - 1	Momentum equation for each pair of nodes
N	Energy equation for each pair of nodes plus wall enthalpy equation
(K - 1) (N)	K-1 sets of "elemental" species equations for each pair of nodes plus wall species equation

Special logic has been written for the matrix inversion, taking advantage of the regular sparseness of the matrix. Once the corrections for the linear and nonlinear variables are found, these corrections are added to the variables to form the new guesses. The magnitude of the errors for each equation are checked and the procedure advances to the next iteration if the absolute values of the errors exceed prescribed upper limits. If the errors are acceptable, iteration is completed for the current streamwise position ξ . Typically, three to six iterations are required to reach a satisfactory solution.

SECTION 4

CONSIDERATIONS FOR SHUTTLE APPLICATIONS

4.1 TRANSITION TO TURBULENT FLOW

For the shuttle vehicle, transition influences not only the choice of TPS material but also sizing of the TPS. Because transition criteria are not well established, many studies have been conducted to assess the affect of various transition onset criteria on peak temperatures and TPS weights. For instance, Reference 20 considered the RI 134B vehicle for both constant and variable angle-of attack entry trajectories and found that 95 to 99 percent of the TPS weight is determined by laminar flow heating. The remainder is due to transition and turbulent heating. This 1 to 5 percent requirement for turbulent flow appears small, however for an RCI system, the total TPS weight may be 20,000 pounds resulting in a 1,000 pound variance depending on when turbulent flow will occur.

The reentry heating conditions determine the peak temperatures experienced by an equilibrium radiation surface which in turn influences the width of the entry flight corridor (References 21-24) (along with equilibrium glide and maximum force constraints). Not only are the conditions which influence transition onset not well established, but the length of the transition zone is not clearly defined. Current best estimates place the ratio Re_t/Re_l at between 2 and 3. Thus a large portion of the vehicle may be in neither laminar nor turbulent heating but rather an in-limbo transitional state.

The question of what constitutes transition has been discussed by several authors (for example, References 13, 25-28). Clearly a general knowledge of turbulence and the transition from laminar to turbulence is not available. However the intermittancy concept, which envisions local flow conditions which are intermittantly laminar and turbulent (References 13, 26, 29, 30) (an average condition being the transition state) has received favorable analytical attention. In effect, an

intermittancy factor is employed which scales the turbulent eddy viscosity between 0.0 and 1.0 of its fully developed value. Both linear as well as nonlinear dependences on flow length from the onset of transition have been considered.

Many possible variables or parameters can affect transition onset. The fact that surface roughness, gaps, discontinuities or external trips can influence transition onset is classical; also heat transfer to surfaces have been known to have a stabilizing effect on the boundary layer. Other variables which have been shown to induce transition include nose bluntness (Ref. 25, 29, 31, 33) mass injection (Ref. 29, 33), entropy swallowing (Ref. 25), adverse pressure gradients (Ref. 27, 34) boundary layer edge conditions (Ref. 25, 34) free stream unit Reynolds numbers (Ref. 25, 27, 33), and vehicle angle-of-attack (Ref. 25, 33). In addition, in wind tunnel experiments, tunnel size, wall effects and noise (Ref. 33) must also be considered.

Because of the large number of variables that apparently have an influence on transition onset, a fundamental theory which encompasses all of these variables is not available. Many correlations of flight and wind tunnel data have been attempted and for shuttle applications, the correlations of References 25 and 35 appear to agree that the boundary layer edge conditions, free stream unit Reynolds number and momentum thickness are good correlation parameters. Similar conclusions were obtained in the Philco-Ford (Ref. 36) correlations presented in Reference 29. Reference 29 showed that both the Philco-Ford and the McDonnell-Douglas (Ref. 35) correlations follow the trend of a large number of flight data. However, most of the data was for slender cones with ablating nosetips and a separate, more involved correlation was obtained by Martellucci (Ref. 29) which includes the effects of nose bluntness and mass addition. For shuttle applications, the amount of mass addition will be small; in addition no significant shape change is expected so that the simpler correlations of References 25, 35 and 36 are recommended.

Reference 25 presents a correlation of the form

$$Re_t = f (M_e \sqrt{Re/ft}) \quad 141$$

Where Re_t is the transition Reynolds number based on edge properties and running length from the stagnation point, M_e is the edge Mach number and Re/ft is the local unit Reynolds number also based on edge properties. This correlation was obtained for a simulated shuttle configuration under wind tunnel conditions ($M_\infty = 10$, $1.0 \times 10^6 \leq Re_\infty/ft \leq 2.4 \times 10^6$) for angles-of-attack between 5 and 35°. From the

data in Reference 25 the functional relationship (141) can be approximated by the expression

$$Re_t \approx (M_e / \sqrt{Re_T / ft})^{1.95} \quad (142)$$

Note, however that the above correlation was obtained for a prescribed vehicle configuration at $M_\infty = 1$ for a particular wind tunnel.

The correlations of Reference 35 are for a number of delta wing configurations under wind tunnel test conditions and has also agreed with slender cone flight data. This correlation has the form

$$Re_{\theta_t} = f(\alpha) (Re/x)^{0.2} M_e \quad (143)$$

Where $f(\alpha)$ is a function of the vehicle angle of attack, Re_θ is the Reynolds number based on momentum thickness, M_e is the edge Mach number and Re/x is the local unit Reynolds number based on edge properties. For the data used to obtain the correlation (143), $f(\alpha)$ has a value of ~ 10.0 for $\alpha < 35^\circ$ and increases to ~ 6 for $\alpha = 60^\circ$. The accuracy of the correlation, as indicated by data scatter, is about a factor of 4. If the unit Reynolds number effect is not considered, the same data is represented by the correlation

$$Re_{\theta_t} \sim 150 M_e \quad (144)$$

with data scatter as high as a factor of 6.

The dependence on unit Reynolds number is small (to the 0.2 power) and Martellucci's independent comparison with the same and other data show a larger amount of data scatter which led Martellucci to question whether or not there is a unit Reynolds number dependence. In view of the fact that Reference 25 and 35 both observed a unit Reynolds number effect for shuttle type vehicles, either correlations (142) or (144) should be used as transition criteria bearing in mind however that the data scatter has an uncertainty factor of about 4 and that the unit Reynolds number effect, if real, is apparently small. Finally it is suggested that some form of intermittency factor be incorporated to simulate a transition zone and that the length of this zone be determined by $Re_T / Re_t \sim 2.0$.

4.2 SURFACE CATALYZED REACTIONS

Since significant dissociation will occur in portions of the flow field surrounding a shuttle vehicle, surface catalyzed recombination reactions represent a significant portion of the energy transfer to the vehicle. The reduced heating which can be realized from low catalycity surfaces would locally reduce the equilibrium radiation temperature for any given flight condition. However, if a rapid change in catalycity from very low to very high occurs as the flow progresses downstream, then the downstream heating is increased by virtue of the noncatalytic upstream section. It is clear that optimization would require a trade-off study which can be performed with the current code provided that adequate data is available for catalytic efficiencies of materials of interest. Surface catalyzed reactions are often defined in terms of catalytic efficiency γ or catalycity K_w .

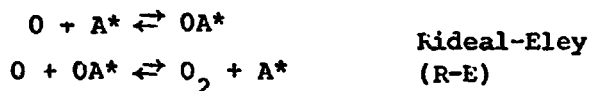
The catalytic efficiency is defined as

$$\gamma = \frac{K_R}{N} \quad (145)$$

Where N is the collision rate of atoms with the surface and N_R is the rate at which these atoms recombine due to collision with the surface. If heterogeneous surface catalysis were due to the simultaneous collision of two atoms and the surface, the recombination rates would be similar in magnitude to homogeneous reaction rates. However, very large catalytic rates ($\gamma \sim 1$) have been observed which lead to the postulation of mechanisms which require an adsorbed layer of atoms on surface active sites with reaction formulas that are identical to homogeneous reaction formulas (Ref. 37-39). Designating A^* as a surface activation site, then the Langmuir-Hinshelwood mechanism is



and the Rideal-Eley mechanism is

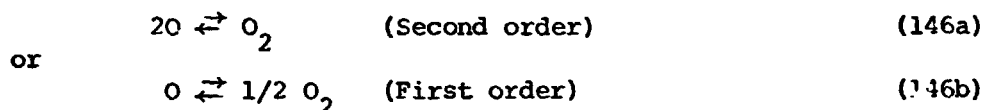


In all likelihood both mechanisms occur simultaneously with rates that depend on the availability of surface active sites and the mobility of absorbed atoms. At high surface temperatures, surface diffusion rates are high and the L-H mechanism is expected to predominate whereas at low surface temperatures the direct collision R-E mechanism is expected to predominate. In any event, it is possible for both mechanisms to be rate limited by the reaction



which depends on the concentration and state of atoms near the surface since the collision rate is a function of the partial pressure of the atoms and their temperature and the probability of the atoms adhering to the surface depends on the kinetic energy (or temperature) of the atoms. Both mechanisms, in terms of the concentration of atomic species, can exhibit first or second order behaviors. For instance, in the L-H mechanism, a slow adsorption of O atoms and a rapid surface migration of OA^* will result in a first order reaction; similarly, the R-E mechanism will be first order for a rapid adsorption of O atoms which forms a high surface density of OA^* such that the reaction $O + OA^* \rightleftharpoons O_2 + A^*$ controls.

The catalycity k_w is defined (Ref. 40) for convenience in gas dynamic studies in terms of local atom concentration and diffusive flux. For a catalytic reaction the diffusion rate, j_w , is equal to the surface reaction rate so that the net overall reaction for both the L-H and R-E mechanisms can be written as



For nonequilibrium boundary layers, the forward direction is the most probable. If the heterogeneous reaction were treated as a homogeneous reaction (with the surface as a third body) then the reaction rate (146a) has the form

$$(\dot{M}_O) = -k_f [(M_O)^2 - \frac{1}{k_c} (M_{O_2})] \quad (146c)$$

Where (M_i) is the molar concentration of specie i , (\dot{M}_i) is its production rate per unit surface area, and k_c is the molar equilibrium constant. For low surface temperatures* and a nonequilibrium condition near the surface the term $(M_{O_2})/k_c$ will be small compared to $(M_O)^2$ so that the reaction rate can be approximated as

* Low temperatures in the current context is defined as a condition in which dissociation is negligible.

$$(\dot{M}_O) = -k_f (M_O)^2 \quad (146d)$$

For near-equilibrium conditions the reaction rate will approach zero with $(M_O)^2 \approx (M_{O_2})/k_c$ and can be achieved with appropriately large values of k_f . Thus at low temperatures reaction (146d) would still be valid since (M_O) approaches zero.

The catalycity k_w is defined for convenience in terms of the local atom concentration and diffusive flux. That is, for a catalytic reaction the diffusion rate, j_w , is equal to the surface reaction rate. Then making use of reaction (146d), with an appropriate transformation to mass production rates, we have (Reference 40)

$$(\rho_w c_w)^n k_w = j_w = \rho_w D_w \left(\frac{\partial c}{\partial y} \right)_w \quad (147)$$

Where n is the order of the reaction and c is the mass fraction of dissociated specie i .

Using a kinetic theory definition of the collision rate, i.e.,

$$N = \frac{P_O}{(2\pi m_O kT)^{1/2}}$$

Where the subscript o is for dissociated species, γ and k_w are then related by

$$\gamma = k_w \left(\frac{2\pi m_O}{RT_w} \right)^{1/2} \left(\frac{m_O}{R^m_w} \right)^{n-1} (P_O)^{n-1} \quad (148)$$

The definition of k_w is convenient since, with it, the surface reaction rate can be expressed in the acceptable form for a forward reaction, i.e., reactions (146a) or (146b).

Note that, for first order reactions ($n = 1$) the relationship between γ and k_w is independent of the specie partial pressures. However for $n > 1$, the partial pressure is required in linking γ to k_w . In addition, if the reaction is first order, at any given value of T_w , there is a maximum finite value for k_w which corresponds to $\gamma = 1$. There is then an obvious discrepancy in the relationship (148) since, as a reaction rate, the limits of k_w should be between 0 and ∞ .

4.3 HOMOGENEOUS KINETICS

Very comprehensive compilations of kinetic reaction rates for oxygen-nitrogen-carbon-hydrogen systems are presented in References 41 through 44. Some of these rates as well as rates from other sources are shown in Table 4-1 and 4-2. For shuttle applications the oxygen-nitrogen reactions are most important; the introduction of small quantities of carbon and silicon compounds, due to ablation or surface oxidations would have only a small effect on the boundary layer solution. Thus oxygen-nitrogen reactions which are important for shuttle environments are shown in the first table and selected carbon-oxygen-nitrogen reactions are shown in the second table. All rates are presented in the modified Arrhenius form

$$k_f = AT^n \exp\left[\frac{E}{T}\right] \quad (149)$$

with T in $^{\circ}\text{K}$ and the units of k_f consistent with (moles - cc - sec). Only forward rates are shown; the presumption being that reverse rates can be calculated from the equilibrium constant k_p or k_c which in turn can be calculated from free energy considerations.

As noted by Dryer (Ref. 45) Equation (149) is not always the best correlation of data, especially over a wide temperature range. This is possibly one of the reasons why Reference 43 recommends two reaction rates; one applicable at high temperatures where the endothermic reaction is dominant and one applicable when the exothermic reaction is dominant. Although it is possible for both exo- and endothermic reactions to be important in different parts of the flow field, only the high temperature values of Reference 43 are shown in Table 4-1.

At wall temperatures of interest, carbon sublimation will be negligible and the primary ablation product from a carbon heat shield will be CO. The relative reactivity of CO with air species was compared and Table 4-2 includes only those reactions which are most likely to have a significant influence on the boundary layer solution.

TABLE 4-1
AIR REACTIONS

	A	N	E (°K)	REF.
1) $O_2 + M \rightleftharpoons O + O + M$				
M = O_2	3.3 (19)	- 1.0	59,400	43
M = O	9.0 (19)	- 1.0	59,400	43
M = N_2	7.2 (18)	- 1.0	59,400	43
M = N, NO, Ar	3.6 (18)	- 1.0	59,400	43
M = N, NO, Ar	2.5 (16)	- 0.5	59,400	46
M = N, NO, Ar	3.5 (18)	- 1.0	59,400	47
2) $N_2 + M \rightleftharpoons N + N + M$				
M = N	4.15 (22)	- 1.5	113,100	43
M = N_2	4.75 (17)	- 0.5	113,100	43
M = O_2 , O, NO, Ar	1.92 (17)	- 0.5	113,100	43
M = O_2 , O, NO, Ar	2.0 (20)	- 1.5	112,500	48
M = GENERAL	4.75 (17)	- 0.5	112,500	46
3) $NO + M \rightleftharpoons N + O + M$				
M = NO, O, Ar	7.8 (21)	- 1.5	75,600	43
M = O_2 , N_2	4.0 (20)	- 1.5	75,600	43
M = O_2 , N_2	5.5 (20)	- 1.5	75,000	48
M = O_2 , N_2	5.3 (16)	- 2.5	75,000	46
4) $NO + O \rightleftharpoons N + O_2$				
	3.2 (9)	1.0	19,550	46, 48 - 51
	3.2 (9)	1.0	19,700	43
5) $N_2 + O \rightleftharpoons NO + N$				
	6.6 (13)	0.0	37,750	52 - 55
	7.0 (13)	0.0	37,750	46, 50, 51
	6.75 (13)	0.0	37,500	43
	6.8 (13)	0.0	37,500	48
6) $N_2 + O_2 \rightleftharpoons NO$				
	9.1 (23)	- 2.5	64,250	48
	8.4 (13)	- 0.5	61,600	43

TABLE 4-2
AIR AND CARBON REACTIONS

	A	N	E (°K)	REF.
1) $\text{CO}_2 + \text{M} \leftrightarrow \text{CO} + \text{O} + \text{M}$				
	2.3 (13)	0.0	37,050	56
	1.8 (20)	- 0.7	65,000	43
	1.3 (18)	- 0.58	62,290	48
2) $\text{CO} + \text{O} \leftrightarrow \text{C} + \text{O}_2$				
	3.0 (12)	0.5	132	43
3) $\text{CO} + \text{O}_2 \leftrightarrow \text{CO}_2 + \text{O}$				
	2.5 (12)	0.0	48	57
	1.6 (13)	0.0	41	58
	7.0 (12)	0.0	51	49
	3.6 (12)	0.0	50	59
4) $\text{CO} + \text{N} \leftrightarrow \text{C} + \text{NO}$				
	4.8 (17)	1.0	100	43
5) $\text{CO} + \text{N}_2 \leftrightarrow \text{CN} + \text{NO}$				
	6.0 (11)	0.0	276	43
6) $\text{CO} + \text{N} \leftrightarrow \text{CN} + \text{O}$				
	2.4 (12)	0.5	92	43
7) $\text{C} + \text{NO} \leftrightarrow \text{CN} + \text{O}$				
	6.0 (11)	0.0	0.0	43
8) $\text{C} + \text{N}_2 \leftrightarrow \text{CN} + \text{N}$				
	1.2 (12)	0.0	56.8	43
9) $\text{C} + \text{O} + \text{M} \leftrightarrow \text{CO} + \text{M}$				
	3.0 (16)	- 0.5	0.0	60

SECTION 5

TYPICAL RESULTS BASED ON EQUILIBRIUM EDGE BOUNDARY CONDITIONS

Because of the difficulties of obtaining inviscid flow solutions with nonequilibrium chemistry for general bodies, many boundary layer calculations are performed using equilibrium edge conditions and, in the case of blunt bodies, isentropic expansions from the stagnation point. For shuttle vehicles, which decelerate at high altitudes and have long characteristic lengths compared to their nose radius, these assumptions are not valid. Nevertheless, these assumptions are convenient and were used to establish the significance of variables such as nodal point distribution, surface catalycity, homogeneous chemistry, and pressure. In most cases to be discussed stagnation point solutions on a nose radius of 2.325', a total enthalpy of 9013 Btu/lbm and stagnation pressures between .004 and .09 atmospheres were used since this would be representative of a shuttle vehicle at relatively high altitudes. The parameters of all cases in this section are shown in Table 5-1 and Figure 5-1. The homogeneous reaction rates are shown in Table 5-2. The values shown in column 2 of this table were used in most cases in this section, however, column 1 was used for comparisons shown in Section 5-1.

5.1 EFFECT OF HOMOGENEOUS KINETICS

The effect of two different sets of kinetic data (Table 5-2) are shown in Figure 5-2 for noncatalytic walls. A significant difference is noted in the N concentrations and results in an equally significant difference in heat transfer (~15% from Table 5-1). Although not shown, the difference decreases as the catalycity increases with no significant differences for fully catalytic walls. The effect of differences in kinetic rates is also expected to decrease as the flow field becomes more reactive, i.e., at higher stagnation pressures. A high density, small nose radius comparison is shown in Figure 5-3. Under these conditions the effect of the two different sets of reaction rates is negligible.

TABLE 5-1
CONDITIONS AND RESULTS FOR COMPARISON CASES

No.	H_T Btu lbm	P_T (Atm)	R_N (ft.)	K_W cm. sec	T_w (°K)	No. of Node		q Btu ft. ² sec	WALL MASS FRACTION					CHEM
						Nodes	Dist.		N	O	O ₂	NO	N ₂	
1	9013	.04	2.325	~ ∞	1800	13	B	44.35	~ 0	5.16(-5)	2.34(-1)	1.39(-3)	7.65(-1)	2
2						7	A	44.48	~ 0	5.15(-5)	2.34(-1)	1.39(-3)	7.64(-1)	2
3				EQUIL		7	A	43.63	~ 0	5.09(-6)	2.34(-1)	1.39(-3)	7.63(-1)	2
4				36		13	C	15.64	2.50(-1)	2.34(-1)	1.45(-3)	1.33(-4)	5.15(-1)	2
5				36		7	A	15.60	2.50(-1)	2.34(-1)	1.42(-3)	1.26(-4)	5.15(-1)	2
6				~ 0		7	A	13.12	2.83(-1)	2.35(-1)	3.49(-5)	1.59(-5)	4.82(-1)	2
7				~ 0		7	A	15.49	2.51(-1)	2.35(-1)	3.45(-5)	8.06(-5)	5.14(-1)	1
8				144		7	A	21.70	1.71(-1)	2.30(-1)	5.79(-3)	9.52(-4)	5.92(-1)	2
9				1440		13	C	39.54	3.32(-3)	1.09(-1)	1.21(-1)	1.31(-2)	7.54(-1)	2
10				144		7	A	8.29	2.36(-1)	2.33(-1)	2.93(-3)	~ 0	5.28(-1)	2
11		.01		144		7	A	4.47	2.67(-1)	2.32(-1)	4.53(-3)	1.54(-4)	4.96(-1)	2
12		.004				13	C	64.75	1.35(-4)	3.29(-2)	1.97(-1)	8.69(-3)	7.61(-1)	2
13		.09		3600		13	C	42.27	2.01(-3)	4.69(-2)	1.82(-1)	1.18(-2)	7.58(-1)	2
14		.04				13	C	19.92	1.03(-2)	8.34(-2)	1.44(-1)	1.32(-2)	7.49(-1)	2
15		.01				13	C	11.67	2.96(-2)	1.09(-1)	1.19(-1)	1.33(-2)	7.29(-1)	2
16	7885	.004		0	1060	7	A	2421	~ 0	8.68(-2)	1.28(-1)	4.61(-2)	7.40(-1)	2
17		6.026	.0833	0		7	A	2443	~ 0	7.87(-2)	1.35(-1)	4.85(-2)	7.84(-1)	1
18				*		7	A	2628	~ 0	1.13(-2)	1.99(-1)	5.53(-2)	7.34(-1)	1

* ∞ for N and O, zero for NO

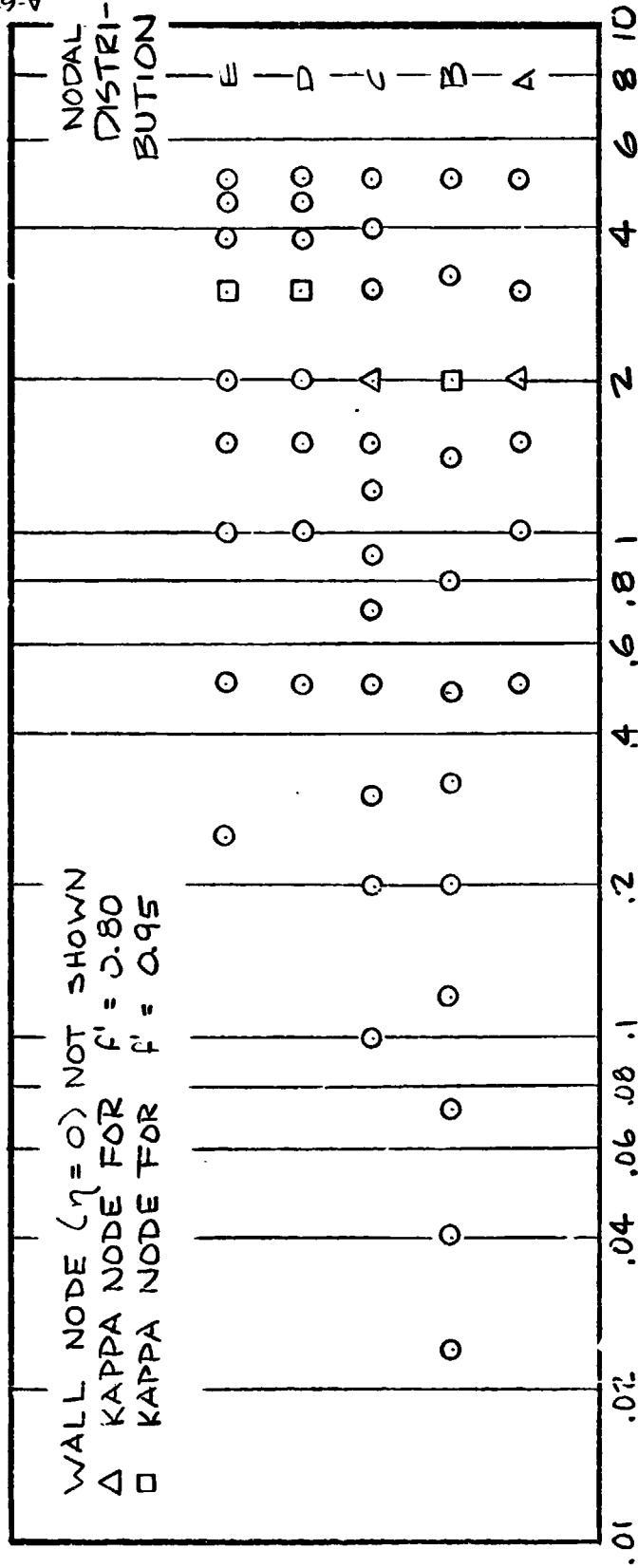


FIGURE 5-1 NODAL DISTRIBUTIONS

TABLE 5-2
REACTION RATE CONSTANTS

REACTION	THIRD BODY	RATE CONSTANTS USED BY REFERENCE 61			RATE CONSTANTS FROM REF. 41		
		A	B	E	A	B	E
$O_2 + M \rightleftharpoons 2O + M$	N, NO O O ₂ N ₂	3.61×10^{18} 9.025×10^{19} 3.25×10^{19} 7.22×10^{18}	-1.0 -1.0 -1.0 -1.0	59,400 59,400 59,400 59,400	2.99×10^{18} 8.49×10^{19} 2.30×10^{19} 2.99×10^{18}	-1.0 -1.0 -1.0 -1.0	59,400 59,400 59,400 59,400
$N_2 + M \rightleftharpoons 2N + M$	O, O ₂ , NO N N ₂	1.92×10^{17} 4.15×10^{22} 4.80×10^{17}	-0.5 -1.5 -0.5	113,100 113,100 113,100	1.90×10^{19} 1.30×10^{20} 3.8×10^{19}	-1.0 -1.0 -1.0	113,200 113,200 113,200
$NO + M \rightleftharpoons N + O + M$	O ₂ , N ₂ N, O NO	3.97×10^{20} 7.94×10^{21} 7.94×10^{21}	-1.50 -1.50 -1.50	76,500 76,500 76,500	2.40×10^{17} 2.40×10^{17} 2.40×10^{17}	-0.5 -0.5 -0.5	75,500 75,500 75,500
$NO + O \rightleftharpoons O_2 + N$	--	3.18×10^9	1.0	19,700	4.30×10^7	1.5	19,100
$N_2 + O \rightleftharpoons NO + N$	--	6.75×10^{13}	0.0	37,500	6.80×10^{13}	0.0	37,750
$N_2 + O_2 \rightleftharpoons 2NO$	--				3.00×10^{10}	0.0	61,600
$N + O \rightleftharpoons NO^+ + e^-$	--	9.03×10^9	0.5	32,400			
Forward Rate Constant = $k_f = A T^B e^{-E/T}$, T = °K							

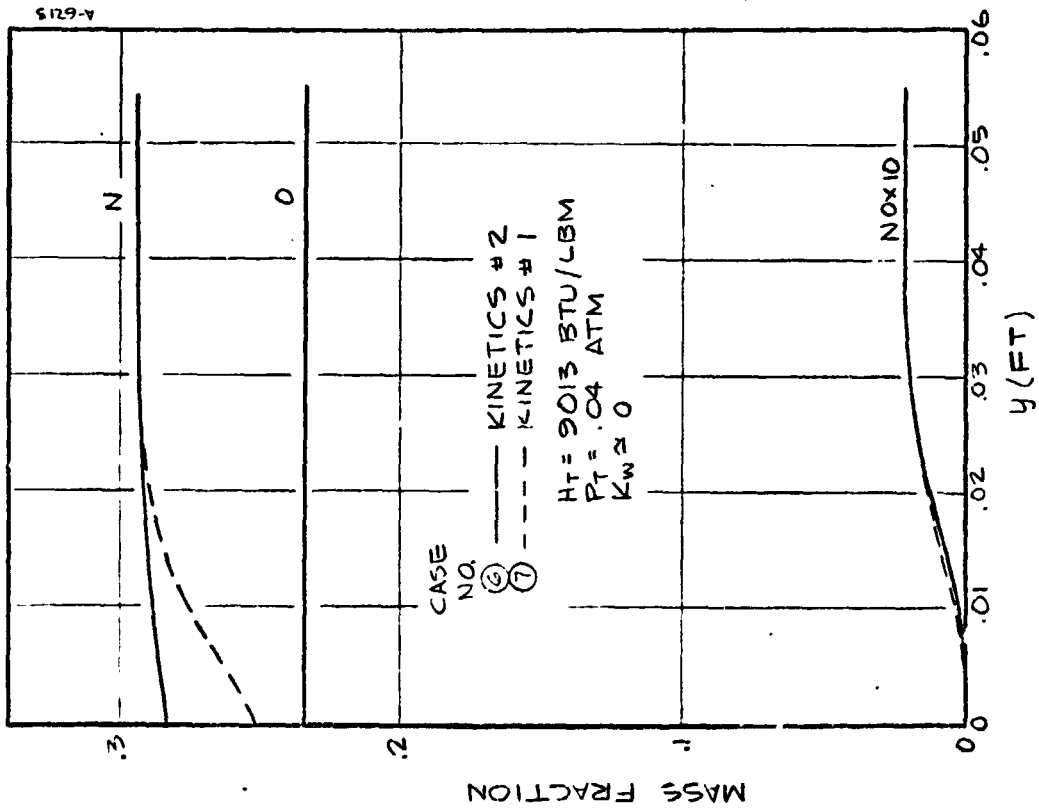


FIGURE 5-2 EFFECT OF HOMOGENEOUS KINETICS

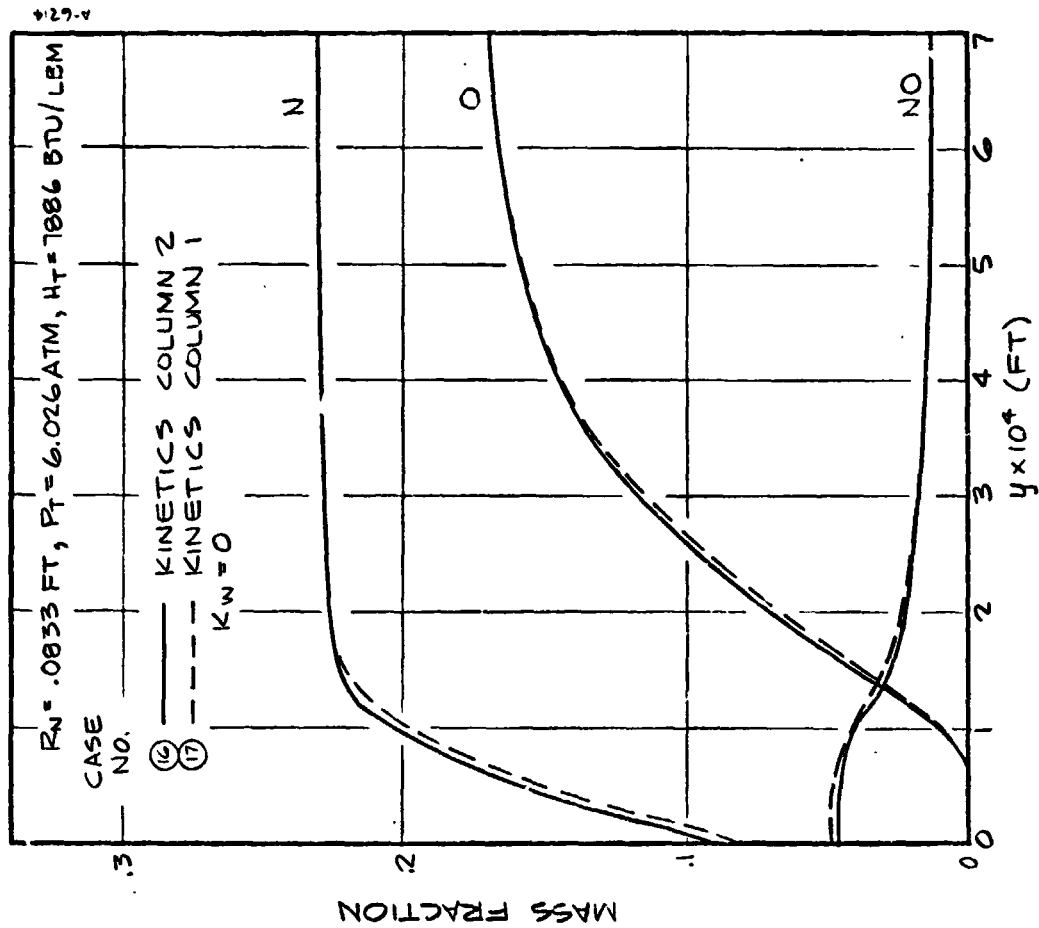


FIGURE 5-3 EFFECT OF HOMOGENEOUS KINETICS

5.2 EFFECT OF NUMBER OF NODAL POINT

The BLIMP computational procedures uses spline fits of the primary variables across the boundary layer and therefore require a lesser number of nodes than linearized finite difference methods. Appropriate nodal point distributions for equilibrium chemistry are recommended in Reference 1 and it appears logical to determine if similar distributions are valid for nonequilibrium conditions. A typical nodal distribution has 7 nodes for laminar boundary layers and 13 nodes for turbulent boundary layers. These distributions are not sacred, however, they and similar distributions provide good starting points for comparing the effect of nodal distribution on predicted boundary layer variables. In this and most of the subsequent comparisons, the mass fractions of N, O, and NO will be shown and used as criteria for determining the magnitude of any discrepancies.

The stagnation point specie distributions for a catalytic wall and a near-noncatalytic wall are shown in Figures 5-4 and 5-5, respectively. The solid lines represent a 13 node distribution and the indicated "data" points are from a 7 node distribution. Both distributions are shown in Figure 5-1. Also shown in Figure 5-4 is the equilibrium distribution. The strong resemblance between the two profiles in Figure 5-4 is a result of the high catalycity which reduces atomic species to zero at the wall. Between the 7 and 13 node distribution there is a small but noticable discrepancy in the NO concentrations for a catalytic wall. However, this is accented somewhat by the fact that the NO scale is magnified by an order of magnitude. All differences between 7 and 13 node distributions are considered small and result in no significant difference in predicted heat transfer rates as shown in Table 5-1.

5.3 EFFECT OF SURFACE CATALYCITY

The effect of catalycity on the specie distribution within the boundary layer are shown in Figures 5-6 to 5-8. It was assumed that the surface catalytic reactions were given by

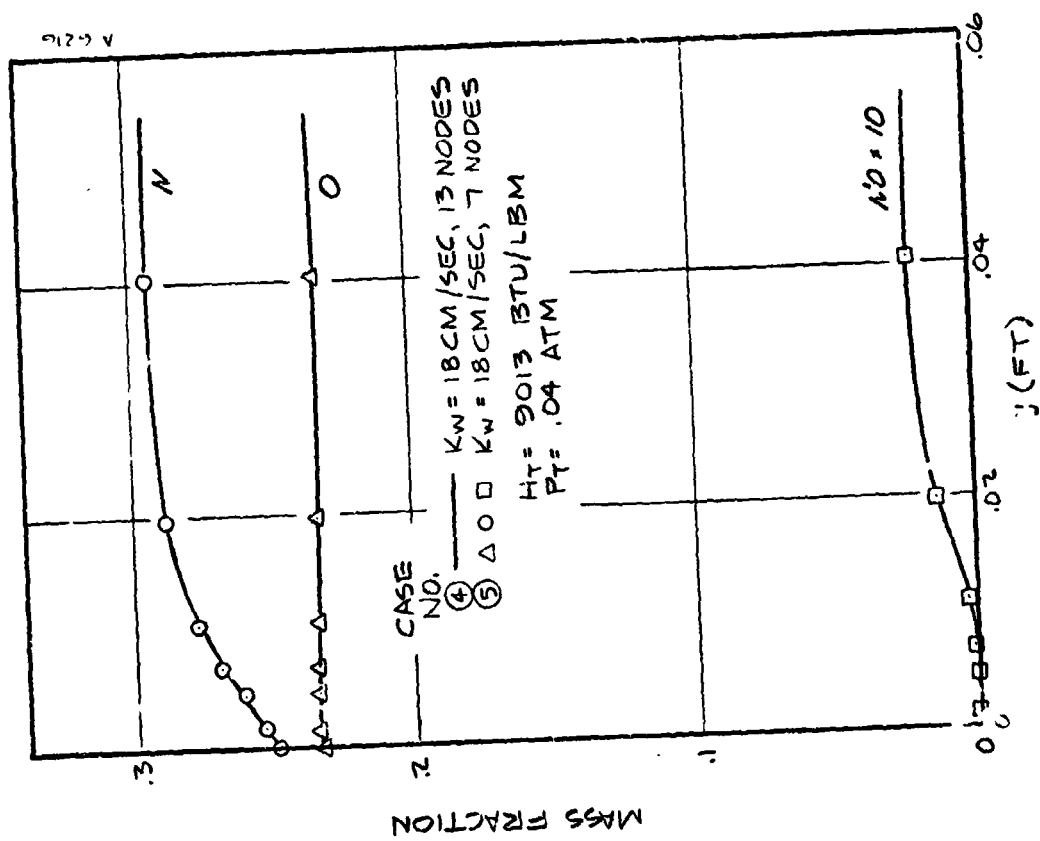


FIGURE 5-4 EFFECT OF NODAL DISTRIBUTION

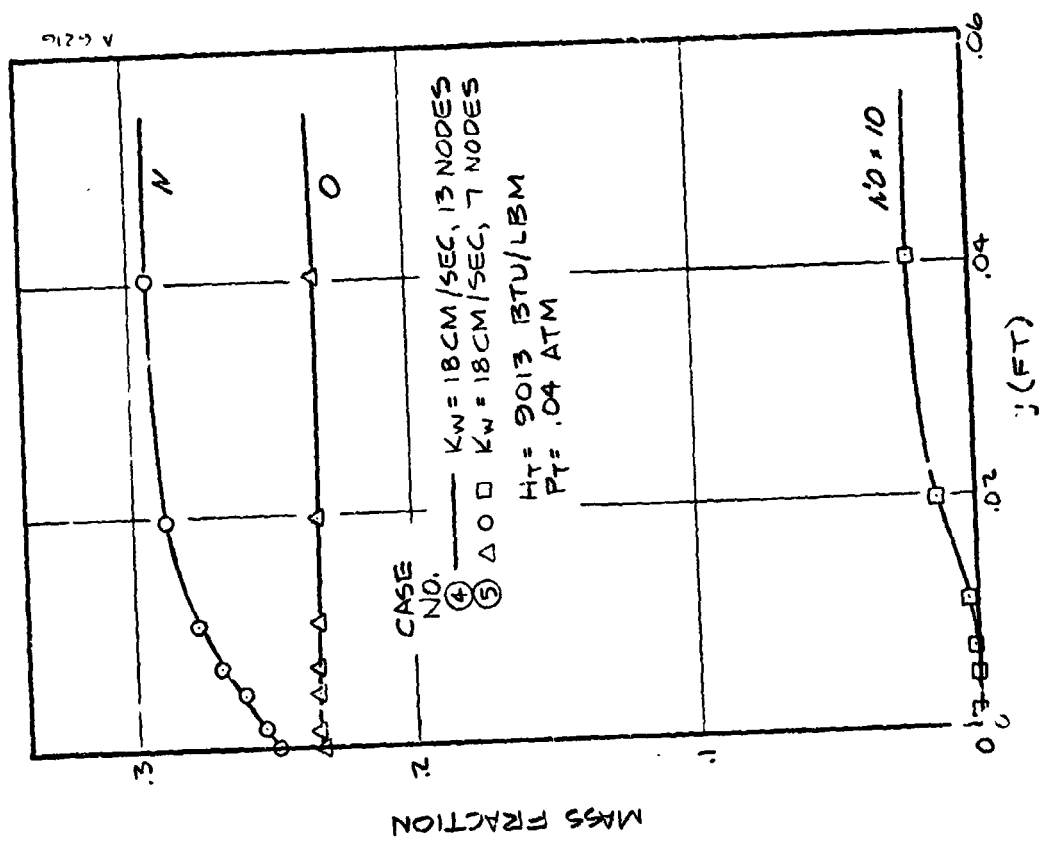


FIGURE 5-5 EFFECT OF NODAL DISTRIBUTION

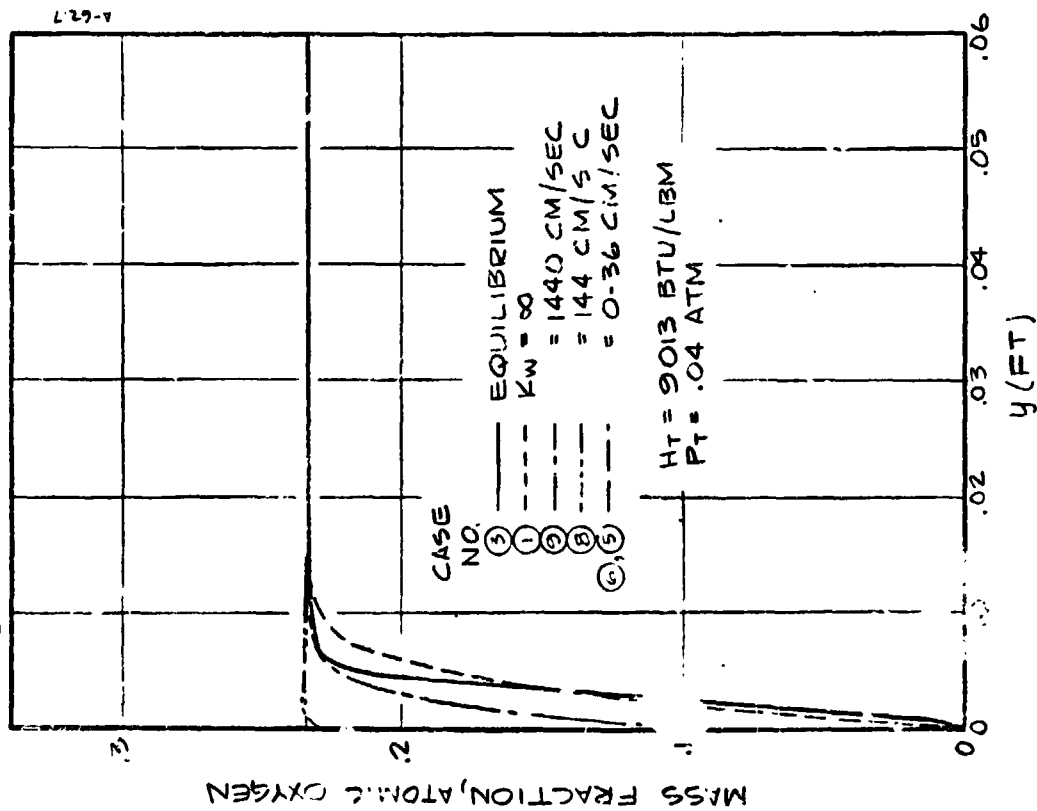


FIGURE 5-6 EFFECT OF SURFACE CATALYTICITY ON ATOMIC OXYGEN CONCENTRATION

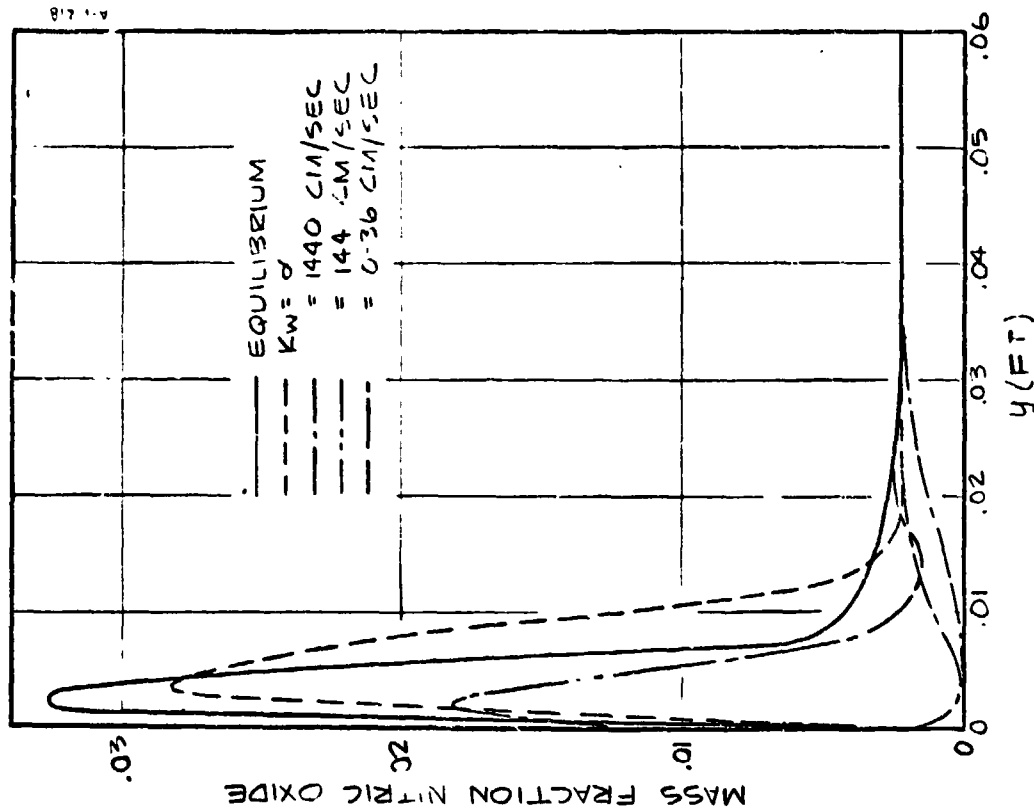


FIGURE 5-7 EFFECT OF SURFACE CATALYTICITY ON NITRIC OXIDE CONCENTRATION

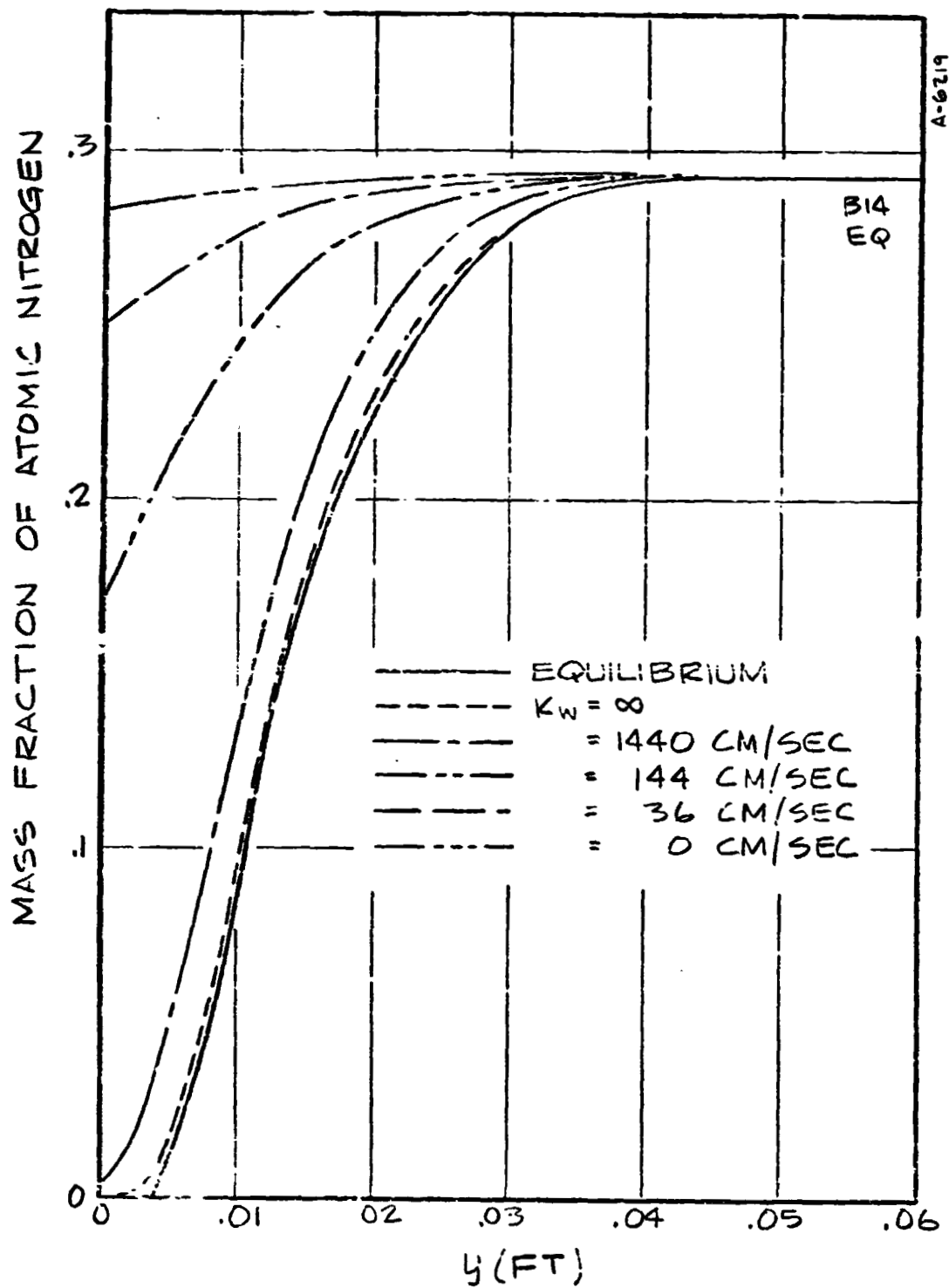
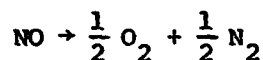
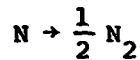
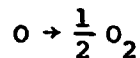


FIGURE 5-8 EFFECT OF SURFACE CATALYTICITY
ON ATOMIC NITROGEN CONCENTRATION



The catalycity for all three reactions were assumed equal although it will be subsequently shown in Section 5.6 that the apparent catalycity of typical shuttle materials is greater for O recombination than for N recombination. Finally, it was assumed that all reactions were first order so that the catalycity can be defined as

$$K_w(A) = \rho_w D_w \frac{\partial}{\partial y} [SP(A)]$$

where A represents O, N or NO and SP(A) represents, the mass fraction of A.

It can be seen from Figures 5-6, 5-7 and 5-8 that the extent to which the reactions at the wall influence the boundary distribution is much greater for N than for O. This is a result of the strong influence of the nitric oxide shuffle reactions which has the net effect of wanting to deplete N in favor of O. Thus, O atom concentrations even for highly catalytic walls are virtually frozen for about 3/4 of the boundary layer. This effect will be shown in Section 5-4 to decrease (i.e., a smaller fraction of the boundary layer being frozen) as the pressure decreases and vice versa.

The ratio q/q_{cat} is shown in Figure 5-9 as a function of the catalycity for the above cases which correspond to a velocity and altitude of about 21,600 ft/sec and 225,000 ft, respectively. This is compared with the results of Reference 40 which used a smaller nose radius (1.95 ft as opposed to 2.325) and a lower wall temperature (760°K as opposed to 1800°K). It can be seen from Figure 5-9 that a significant difference exists between the two predictions. The effect of the difference in nose radius is expected to be small. An increase in wall temperature would shift the curves to the right slightly, however, most of the difference is probably due to the binary gas behavior used in Reference 40.

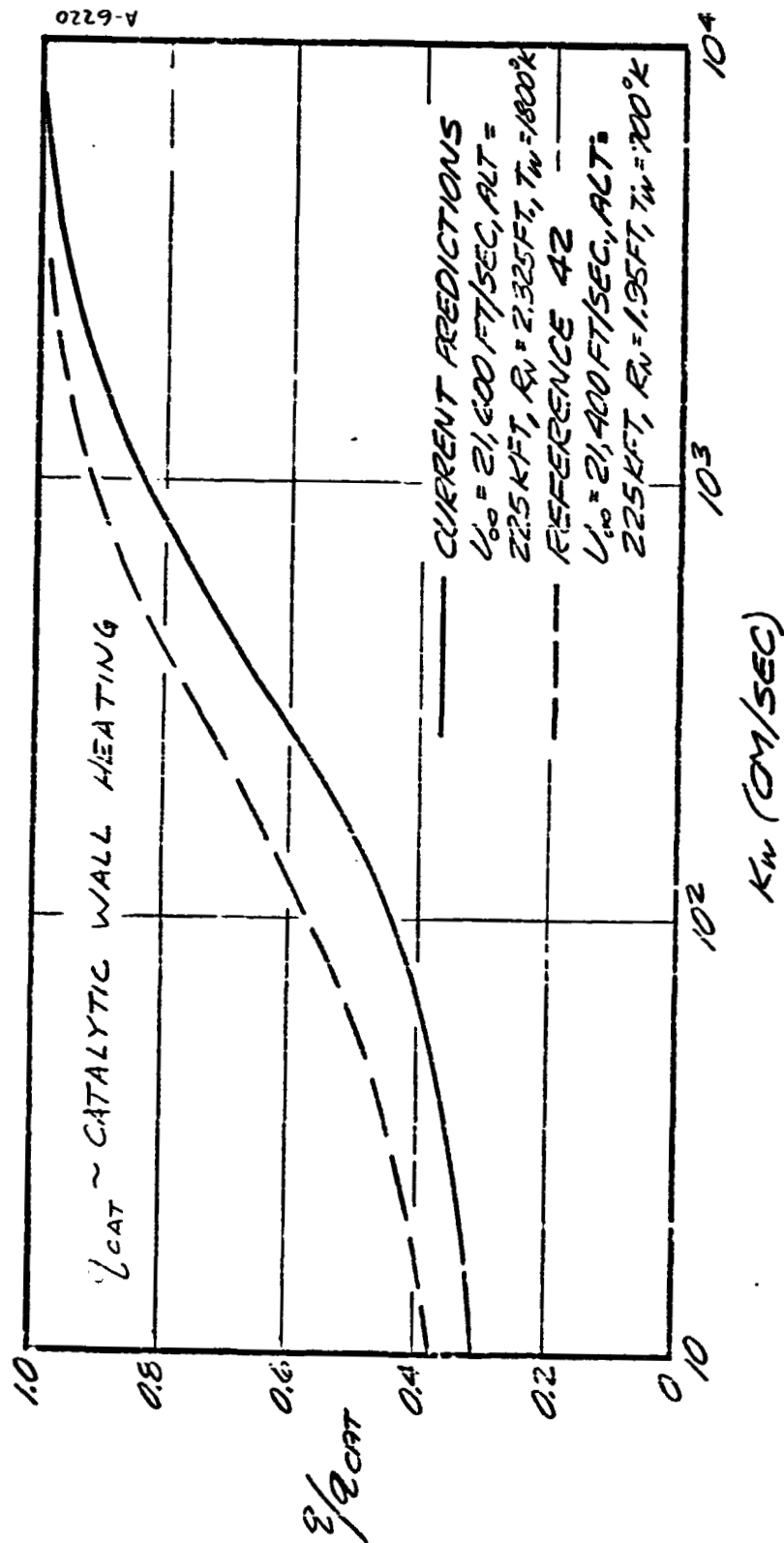


FIGURE 5-9 EFFECT OF SURFACE CATALYTICITY ON HEAT TRANSFER.

It is clear from Figure 5-7 that NO distributions are strongly dependent on the wall catalycity and the resulting interaction with the shuffle reaction will doubtless have significant effects on the wall values of O and N concentrations (thereby affecting the heating rates). It is, therefore, necessary to exercise some caution in the specification of wall catalycities from experimental data since homogeneous reactions, even in near frozen flows, are intimately coupled to the wall reactions.

5.4 EFFECT OF PRESSURE

The effect of stagnation pressure on specie distributions is shown in Figures 5-10 and 5-11 for a low catalycity wall (144 cm/sec) and a high catalycity wall (3600 cm/sec). Since the boundary layer thickness is highly dependent upon the pressure the normal coordinate y was normalized with respect to a reference value representing the value of y at a fixed value of u/u_e (in this case $u/u_e = 0.8$). The degree of dissociation at the boundary layer edge for equilibrium is also dependent on the pressure, however, no normalization was made in plotting the graphs. Although there are differences in the distributions at different pressures, these differences are not dramatic as long as the wall catalycity is fixed.

A comparison of the heat transfer rates as a function of pressure are shown in Figure 5-12. Also shown are the slopes for $q \sim \sqrt{p}$. As might be expected, catalytic wall heat transfer can be scaled by this classic relationship with moderate accuracy, however, low catalycity walls can not be scaled in this form.

5.5 COMPARISON OF CURRENT PREDICTIONS WITH REFERENCE 61

The relative accuracy of predictions from the current code were compared with those from the computer code described in Reference 61. This latter code was made available to Aerotherm by F. G. Blottner so that output from both codes could be compared directly. A case from Reference 61 was used for comparison, namely, a spherical nose with a radius of 0.0833 feet at stagnation conditions of 6.026 atmospheres and 7886 Btu/lbm. The rate constants used in both codes were those shown in column 1 of Table 5-2 and edge conditions were those given in Reference 61. Specie distributions are shown in Figure 5-13 for a wall which

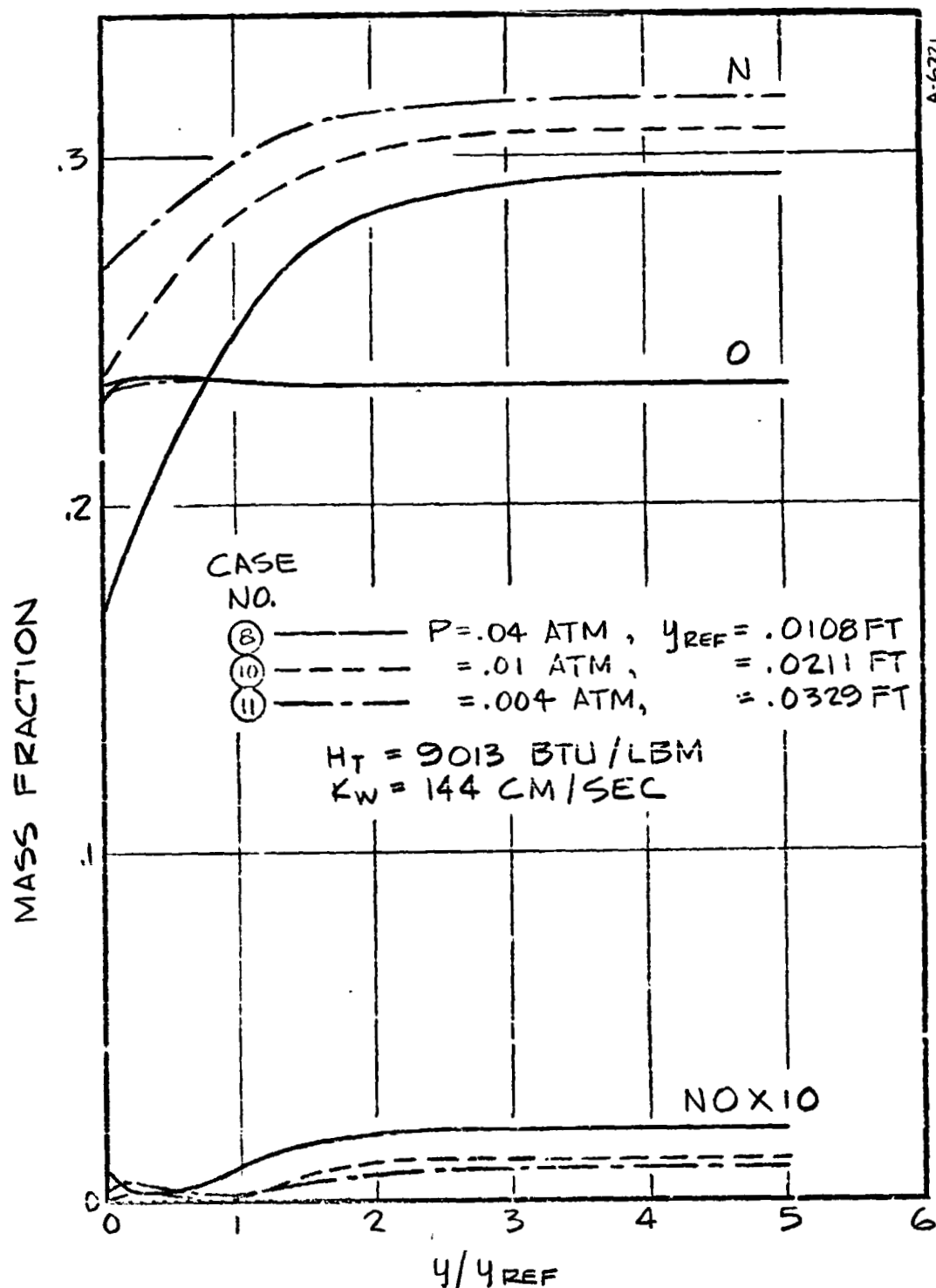


FIGURE 5-10 EFFECT OF PRESSURE

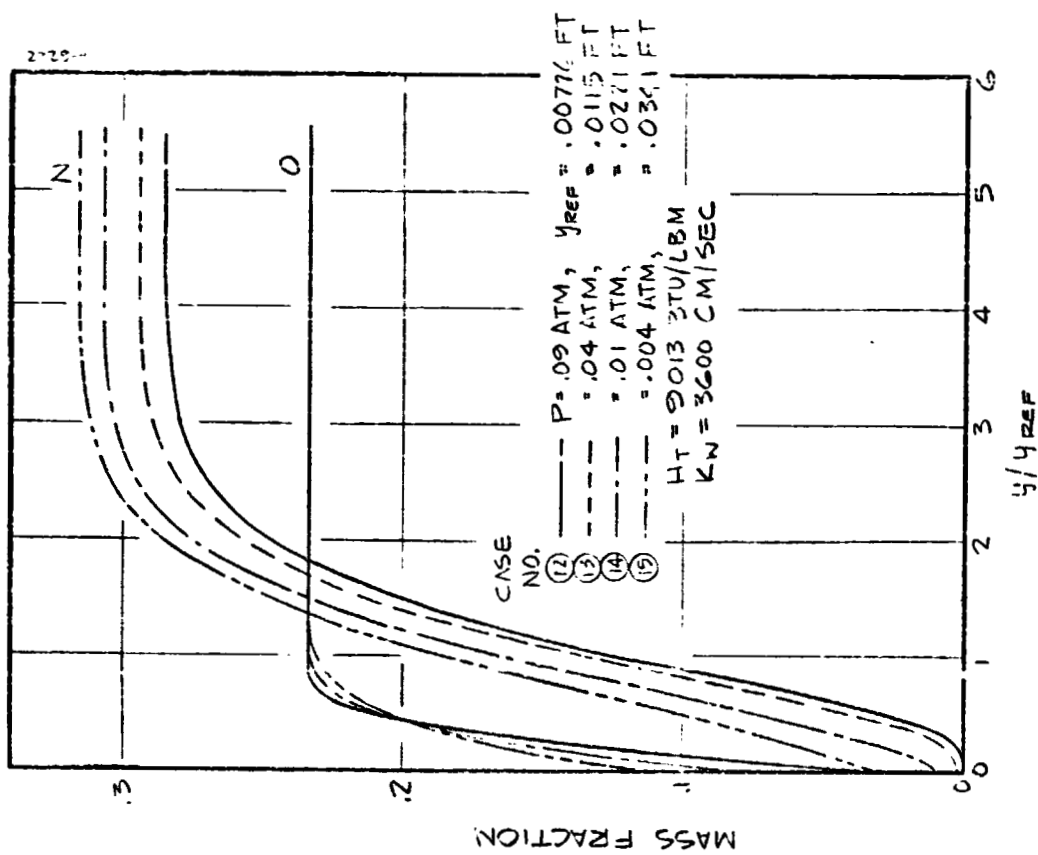


FIGURE 5-11A EFFECT OF PRESSURE

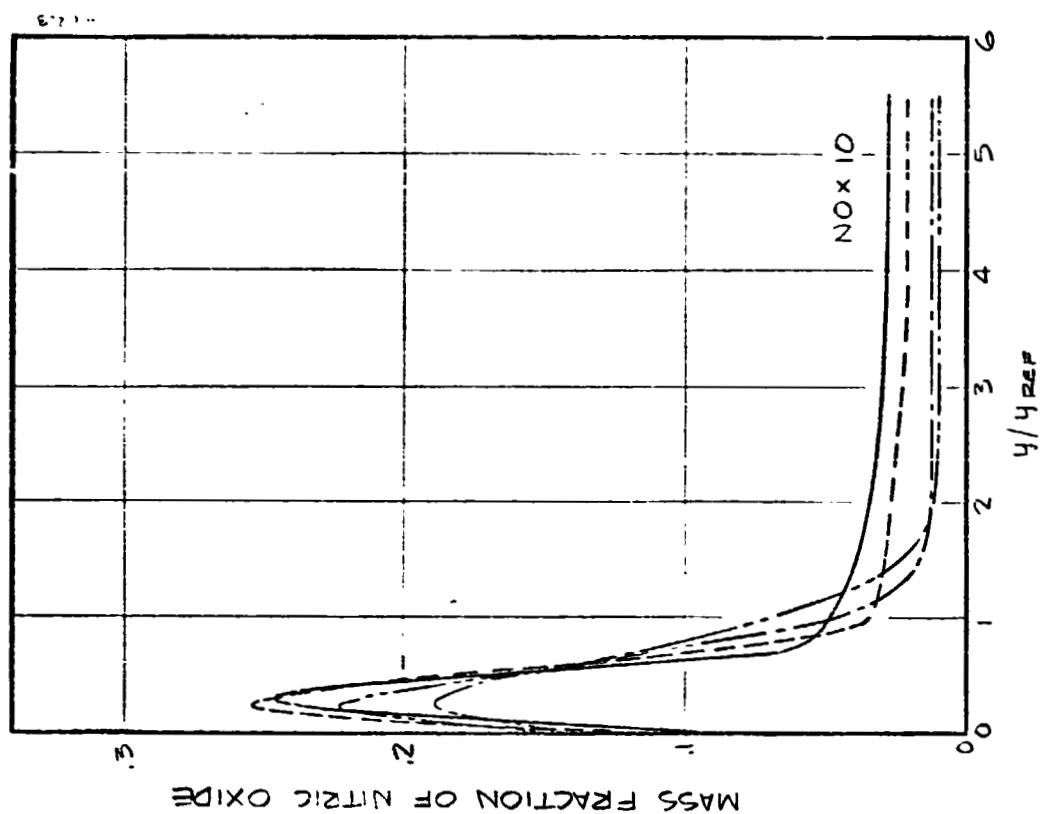


FIGURE 5-11B EFFECT OF PRESSURE

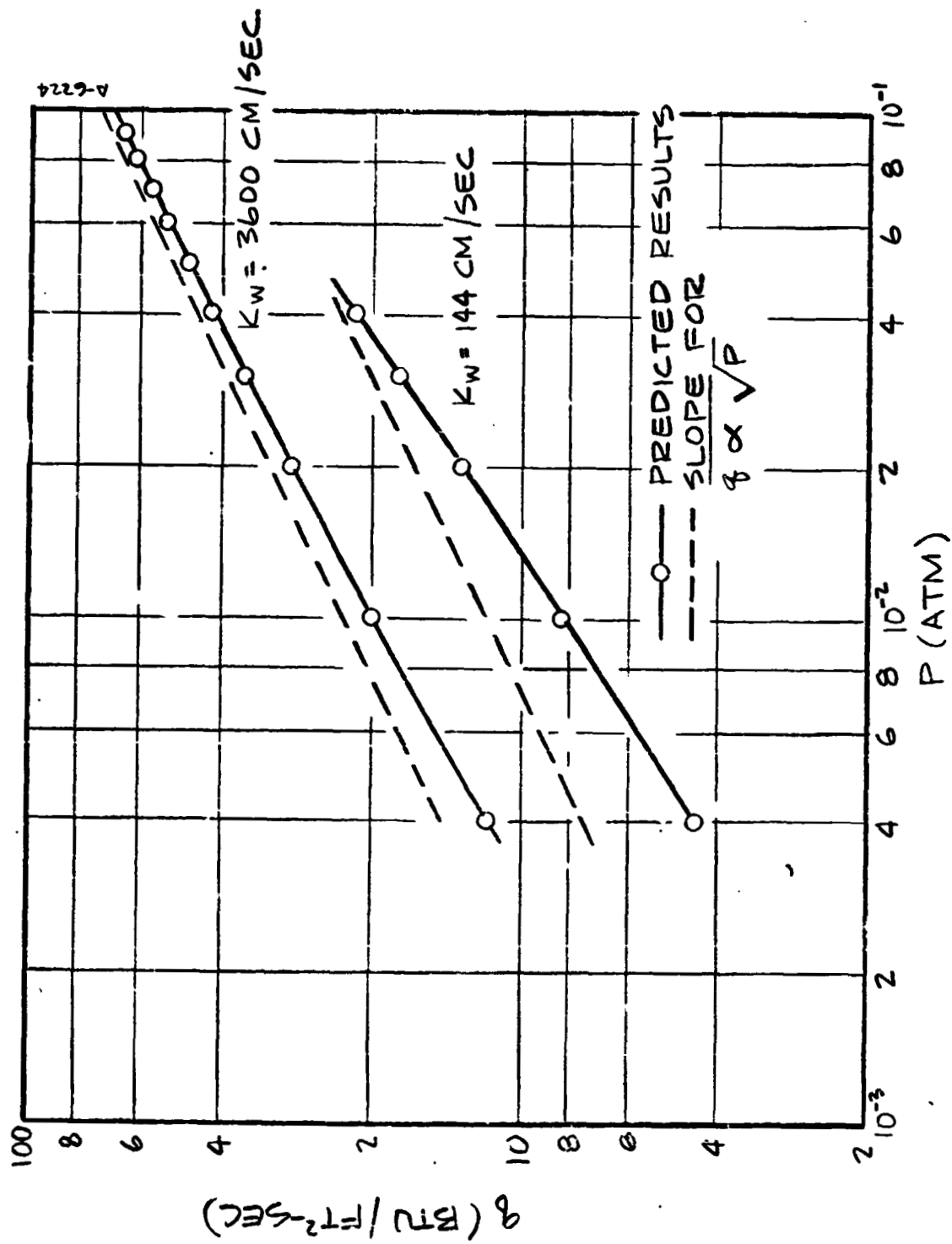


FIGURE 5-12 PRESSURE DEPENDENCE OF NONEQUILIBRIUM HEAT TRANSFER

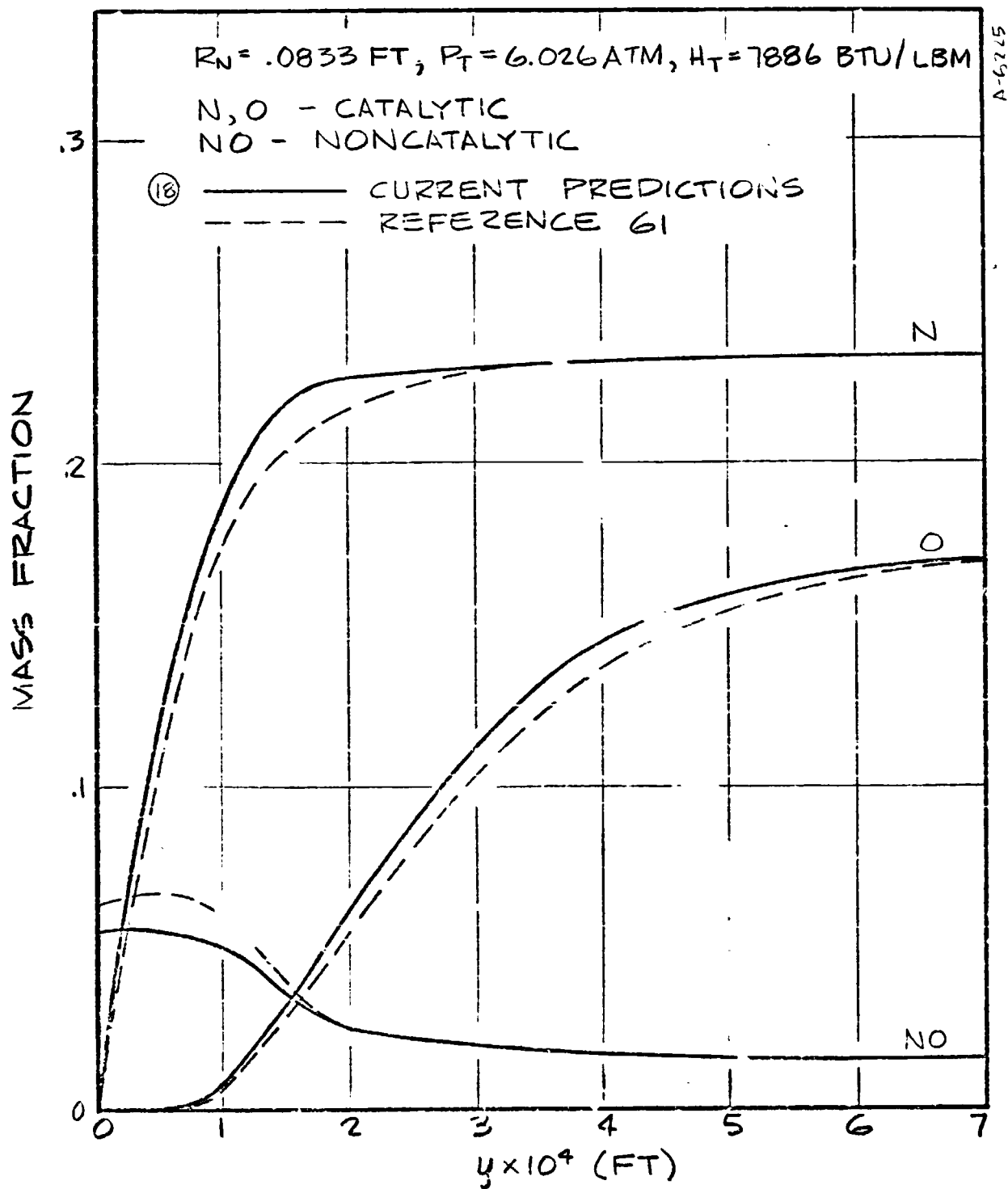


FIGURE 5-13 COMPARISON OF CURRENT PREDICTIONS WITH REFERENCE 61

is catalytic to N and O recombination, but noncatalytic to NO reactions. Similar distributions are shown in Figure 5-14 for a noncatalytic wall. For catalytic walls, the differences are relatively small, however, a significant difference, especially in the concentration of O, is noted for the noncatalytic case. The probable reasons for these differences have not been resolved but would appear to be either in the computational procedure or the thermodynamic models.

5.6 ANALYSIS OF ARC JET DATA

Plasma arc jets have been used extensively for the simulation of reentry heating environments and some recent data was reported in Reference 62 for candidate shuttle materials, namely, oxidation inhibited carbon-carbon composites (LTV), coated silica refractory insulation (LI-900) and coated columbium. The surface coating on the carbon-carbon is believed to be primarily silicon carbide. Composition of the other coatings is given in Table 5-3. All coatings have a significant amount of silica which at high temperatures is expected to form a glassy surface with a low to moderate catalycity. The referenced data was obtained for dissociated air over a range of enthalpies between 3000 and 20,000 Btu/lbm and at a pressure of about 0.01 atm with flat faced cylinder models. At the low enthalpy conditions, only oxygen would be dissociated under equilibrium conditions whereas at the higher enthalpies both oxygen and nitrogen would be dissociated. The maximum enthalpy of 20,000 Btu/lbm is significantly greater than would be experienced by an earth orbit reentry vehicle and would result in some ionization which is not considered in the current analysis. The data was not obtained with the intent of calculating catalytic efficiencies so that there is no data for any one of the materials which span the whole enthalpy range. However, since all coatings contain silica and have glassy properties, it was assumed that their catalytic behavior would be similar. Thus, the data was considered as a complete set and the BLIMP/KINET code used to estimate the average catalytic efficiencies for both O and N recombination in dissociated air.

The calculations were performed on the assumption that the edge of the boundary layer at the stagnation point was in chemical equilibrium. Although the chemical state of the arc jet flow was not measured, the stagnation point would be at or close to equilibrium since a high pressure dissociated equilibrium state is attained in the plenum and the rapid expansion in the nozzle retards chemical recombination. Thus only a small change in chemical composition would be required, as the flow transverses the bow shock, to reach a stagnation point equilibrium state.

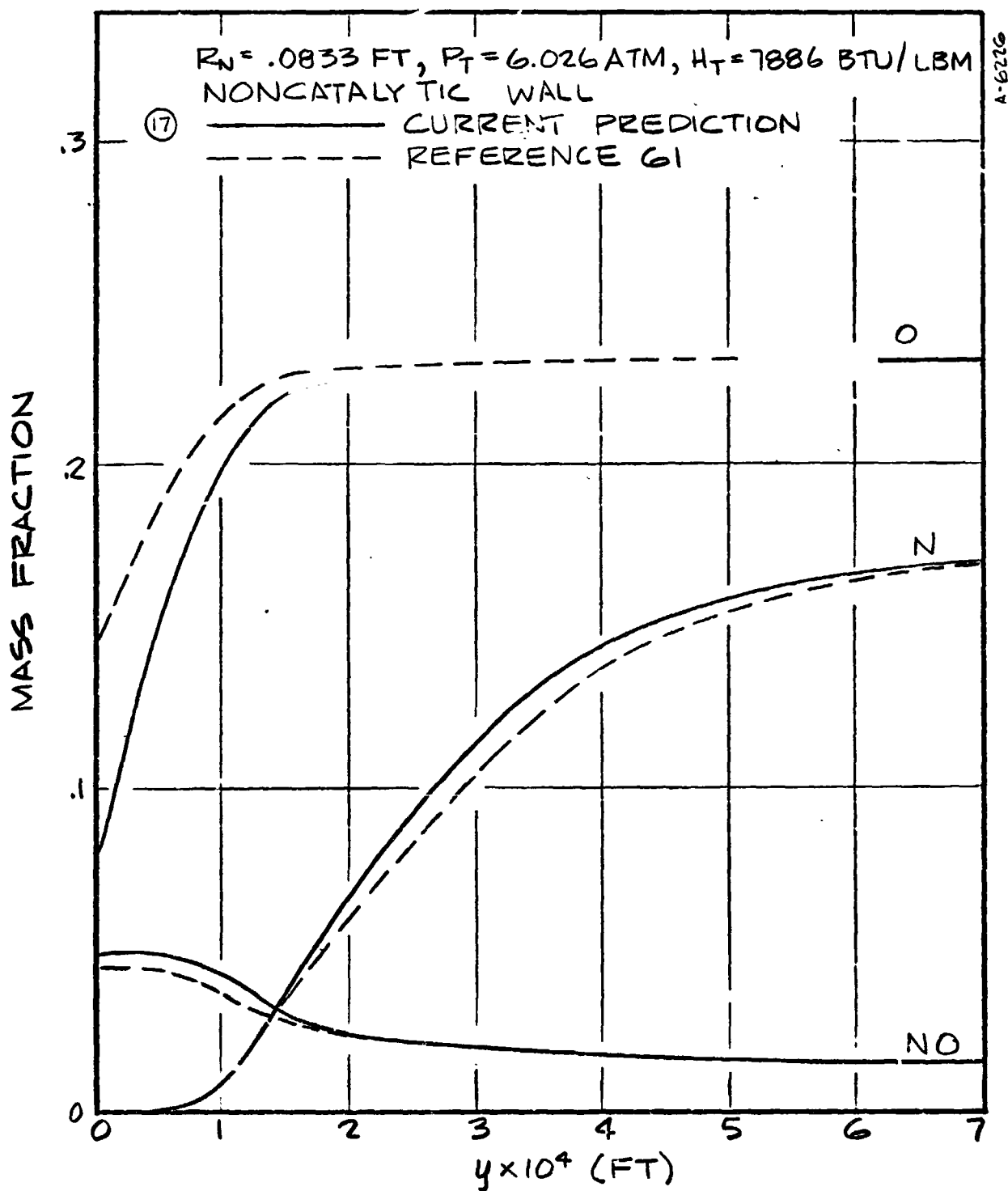


FIGURE 5-14 COMPARISON OF CURRENT PREDICTIONS WITH REFERENCE 61

TABLE 5-3
ELEMENTAL COMPOSITION OF COATINGS, % BY WEIGHT

	R5 12E Coated Columbium 752	VH 109 Coated Columbium	LTV Coated Carbon- Carbon	LI 900
Si	38	70		
Nb	57			
W	4			
Fe	.2	5		
Cr	.1	5		
Hf		20	(1)	(2)
(1) Proprietary but believed to be mostly SiC				
(2) Silicon carbide, borosilicate glass. Ref. 22				

Stagnation point solutions were then obtained over the prescribed enthalpy range for various values of the surface catalycity for O and N recombination. For all but one set of computations, the wall was assumed to have no effect on NO chemistry. The assignment of a wall that is noncatalytic to NO reactions was simply an expedient to reduce wall catalytic effects to two parameters, namely, the catalycities of N and O. It is clear that a significant number of coupled chemical reactions occur simultaneously on the wall and in a zone near the wall. Further it is known that the gas phase NO shuffle reactions are very rapid so that slow generation or depletion rates of NO at the wall would be rapidly compensated for by homogeneous gas phase reactions. Even so, since it is not possible to determine the rates for all possible simultaneous surface reactions, the data, from which multi-component catalycities are deduced, should be obtained at pressure levels which are representative of the flight environment.

The wall reaction rate parameters (FKF) are shown in Table 5-4 for each set of calculations and the ratio of q/q_{cat} is shown in Figure 5-15. Also shown are the data for the three materials as determined from the equilibrium radiation surface temperature. At low enthalpies, where only oxygen is dissociated, the curves all come together at a value of $FKF(O)$ equal to 0.02. At higher enthalpies where both oxygen and nitrogen is dissociated, extensions of the curve for $FKF(N)$ equal to 0.006 appear to best represent the data, at least for enthalpies less than 14,000 Btu/lbm. At higher enthalpies the ratio q/q_{cat} either remains constant or increases slightly. This may be due to ionization effects or a shift in composition of surface adsorbed atoms from O to N, thereby increasing the catalytic efficiency for N recombination. At the higher enthalpies, due to the fact that ionization was not included and complete dissociation was achieved, the amount of energy stored as chemical energy no longer increased with the total enthalpy of the flow. Thus, fortuitously, the predicted ratios of q/q_{cat} also increased at the higher enthalpies.

The values of FKF are related to K_w (as shown in the Appendix) by the relationship

$$K_w = \frac{FKF \times T_w}{0.761} \quad \text{ft/sec}$$

when the surface reaction is considered as

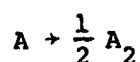


TABLE 5-4
SURFACE REACTION RATE CONSTANTS

CURVE	FKF(0)	FKF(N)	FKF(NO)
1	0.02	0.006	NC
2	0.02	0.012	NC
3	0.02	NC	NC
4	0.02	0.02	0.02
5	0.02	0.0002	NC
6	0.02	0.002	NC
7	0.002	0.002	NC
8	0.02	0.008	NC

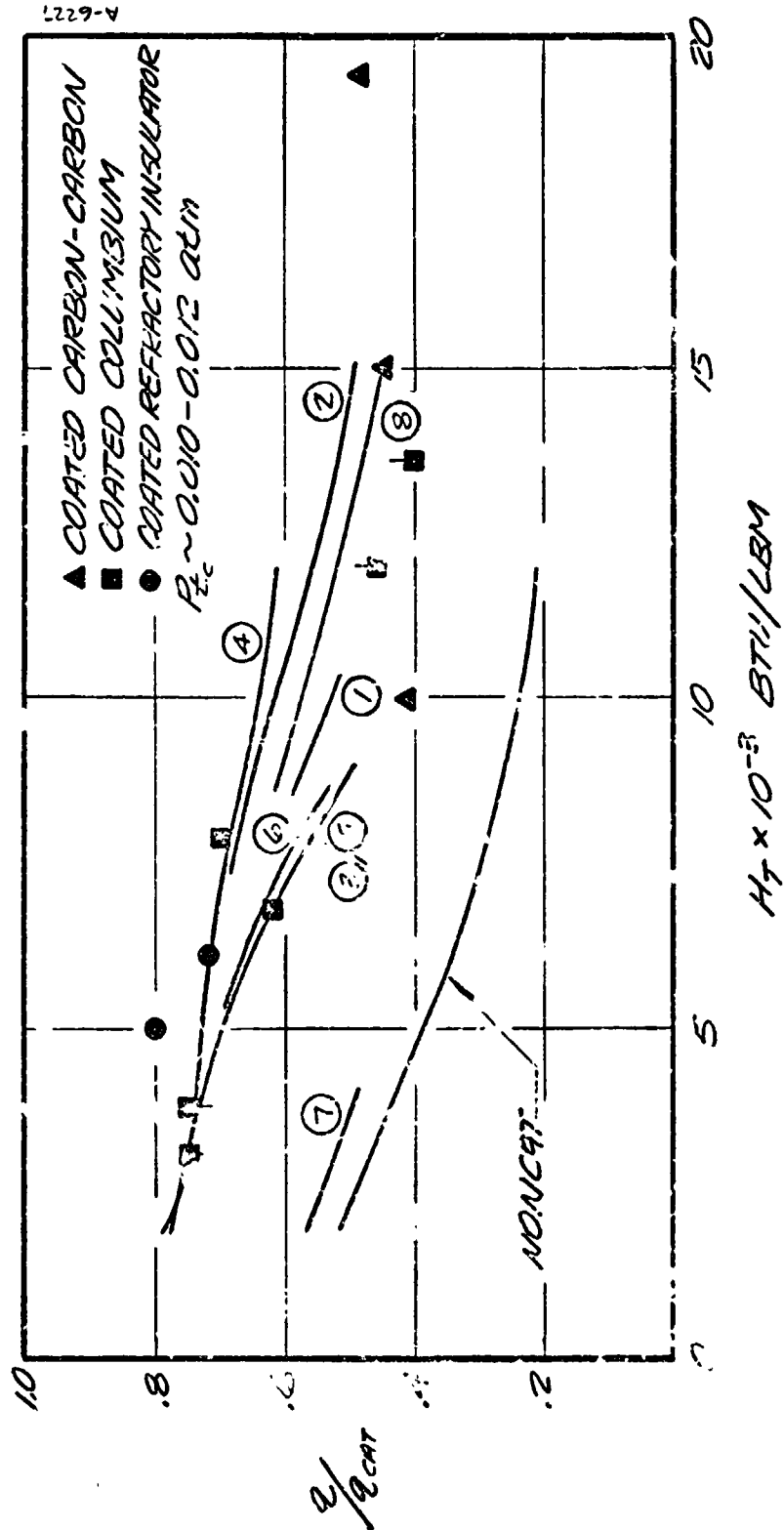


FIGURE 5-15 CATALYTICITY EVALUATION.

SECTION 6

APPROXIMATION OF NONEQUILIBRIUM CONDITIONS AT EDGE OF BOUNDARY LAYER

The development of a nonequilibrium computer code for calculating the inviscid flow field about a three-dimensional shuttle body is a formidable task being pursued by several investigators. Until these codes become operational, however, some approximate methods are required to obtain realistic boundary layer calculations. In this section, an approximate procedure is presented for specifying the edge boundary conditions. The computations are performed in three steps. The first step is an approximation of the pressure history along various streamlines in the inviscid flow field. The second step uses the pressure history and initial conditions of the streamline to calculate the thermochemical state, including entropy, along the streamline. The final step is to match the boundary layer mass flow with the mass flow represented by the streamline. Clearly planar or axisymmetric assumptions are necessary in order that mass flows be defined.

Although in the current context, this procedure is applied to shuttle flow fields, it is not necessarily limited to this application. For instance, the chemical relaxation code (step 2) can be used for the computation of chemical reactions on any prescribed pressure streamline.

6.1 CORRELATION OF INVISCID SHOCK LAYER FLOW FIELD

The inviscid flow field on the windward pitch plane of a space shuttle was calculated over a range of flight conditions representative of a typical entry trajectory. In particular, the initial conditions immediately behind the detached shock wave and the spatial pressure history of several streamlines were calculated. The correlations presented here were the data base for these calculations.

The crucial features known to dominate the flow field property distribution are the shock surface and the body which supports it in a hypersonic angle of attack flow. For this reason, curve fits were prepared for second-order (curvature variation) smooth shock and body surfaces and used as defining boundaries in the correlation functions.

In addition it is convenient to characterize the equilibrium hypersonic shock layer equation of state properties using an analytic representation as opposed to more cumbersome table look-up. These state functions are also presented here.

The data correlations are supplied in graph and tabular form and where available, in functional form for subsequent use. Included are pressure distributions, enthalpy ratios at the shock entrance position (transition ratios) for each of the selected streamlines, streamline traces (distance along the streamline as a function of body axial coordinate station) and quantitative comparisons with available measurements or exact inviscid calculations.

6.2 GEOMETRY

Figure 6-1 shows the body oriented coordinate system adopted for the code solutions as well as the correlations. Here the windward generator axis is rotated about its origin at positive angle of attack, α . The axial distance is \bar{x} measured from the origin $\bar{x} = 0$ at nose. The basic coordinates are the distance along the body measured from the forward stagnation point, ξ_0 , or along selected streamlines, measured where they enter the shock, $\xi_i = 0$, for example, which is the entry position for the i th streamline. The streamlines selected for the correlations are traced through the shock layer a distance ξ which corresponds to a body station distance (axial dimension) \bar{x} , given in the graph, Figure 6-2.

All length measures in the correlations are ratioed to the nose radius, R_0 . \bar{r} is the dimensionless radial dimension of a point in the shock layer measured from the body generator axis while $\bar{r}_w(\bar{x})$ is the radial surface dimension at station \bar{x} , and $\bar{r}_\delta(\bar{x})$ is the radial shock dimension at \bar{x} . \bar{y} is the coordinate measure of a point in the shock layer measured along a normal from the body and has a value $\bar{\delta}$ (the shock standoff) at the shock. θ_δ and θ_w refer to shock and body inclination angles, respectively. Both are measured as clockwise angular deviations from the normal to the body axis as shown. The effective shock angle at positive angle of attack, α , is simply

$$\Lambda \equiv (\theta_\delta - \alpha) \quad (150)$$

The components of velocity, \bar{u} , \bar{v} are oriented positive along streamlines ξ and outward normal to them, respectively. Velocities and components appear as ratios to the free stream velocity, U_∞ . Shock layer density $\bar{\rho}$ is ratioed to the free stream density ρ_∞ . Shock layer pressure \bar{p} is ratioed to twice the free stream dynamic pressure, although in the correlations, it always appears as ratioed to the stagnation point pressure \bar{P}_{T0} , or the local streamline total pressure, $\bar{P}_{T\delta}$. The static enthalpy \bar{h} is ratioed to the square of the free stream

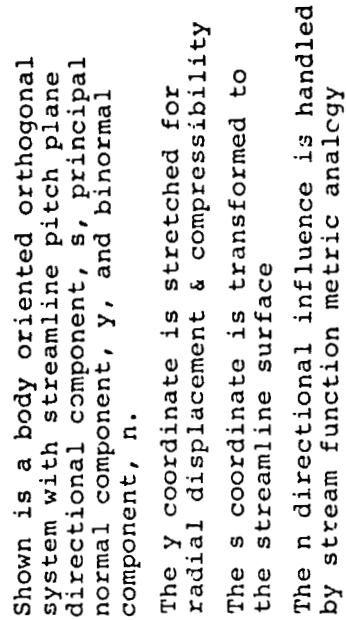


FIGURE 6-1 BODY ORIENTED COORDINATE SYSTEM

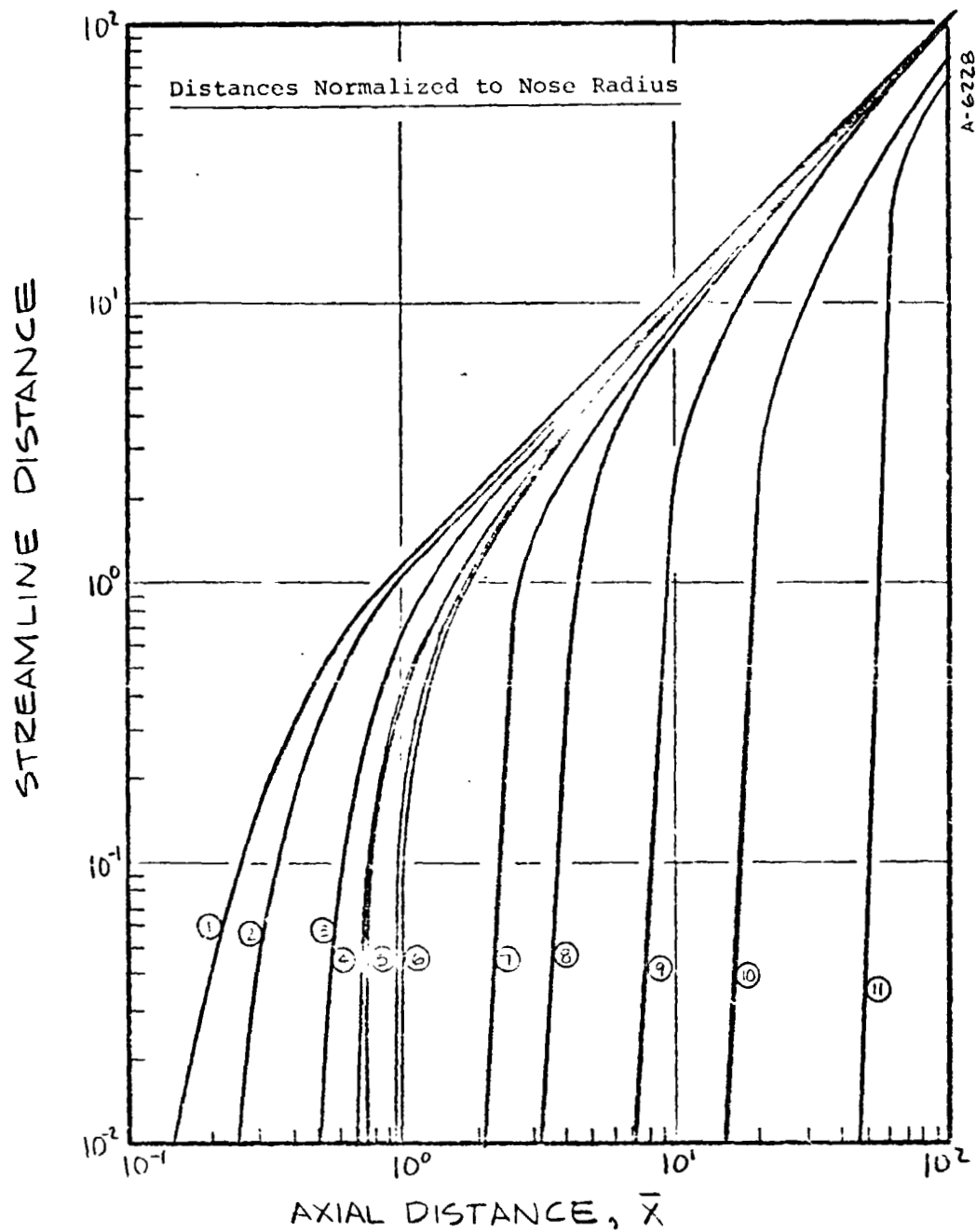


FIGURE 6-2 SPACE SHUTTLE SHOCK LAYER
STREAMLINES

velocity, although in the correlations it is normally ratioed to the total enthalpy, H_{To} .

Figure 6-3 shows details of the shock layer stand-off geometry. Once the body surface variables $\bar{r}_w(\bar{x})$, $\theta_w(\bar{x})$, $\bar{\kappa}_w(\bar{x})$ are computed from the curve fit expressions, the necessary shock values may then be readily computed from the wall variables and one additional correlatable parameter, the shock stand-off, $\bar{\delta}(\bar{x})$. The geometry of Figure 6-3 is characterized by a simple set of defining shock wave-surface relations:

$$\bar{r}_\delta = \bar{r}_w + \bar{\delta}(\bar{x}) \sin \theta_w \quad (151)$$

$$\tilde{x} = \bar{x} + \bar{\delta}_o - \bar{\delta}(\bar{x}) \cos \theta_w \quad (152)$$

$$\theta_\delta = \tan^{-1} \left(\frac{\partial \tilde{x}}{\partial \bar{r}_\delta} \right) \quad (153)$$

$$d\zeta_\delta = \sqrt{d\tilde{x}^2 + d\bar{r}_\delta^2} \quad (154)$$

$$\bar{\kappa}_\delta = \frac{d\theta_\delta}{d\zeta_\delta} \quad (155)$$

The mass flow calculations which are used to obtain the \bar{y} displacements of the streamlines in the shock layer, and to establish the position at which a streamline enters the boundary layer are based on some additional geometric considerations.

Figure 6-4 shows the geometry illustrating the mass flow balance used for the inviscid streamline displacements. Adoption of a generator axis nose intercept origin for the axial displacement ($\bar{x} = 0$) necessitates accounting for both the radial offset of the generator axis (\bar{A} in the figure) and the normal dimension, \bar{S}_o , which is a measure of the shift of the forward stagnation point at angle of attack. The mass flow intercepted by the shock over an annular section of radius, \bar{S}_o , is spilled over the leeward side of the body at angle of attack. This is accounted for by subtracting this leeward mass flow when computing the dimensionless mass flow for a given streamline.

The geometry leads to the following set of relations for dimensionless mass flow associated with the i th streamline. In these equations \hat{Z} is the rotated angle of attack annular radius while μ is the local flow angle.

$$\hat{Z}_i = (\bar{r}_0 + \bar{A}_i) \cos \alpha \quad (156)$$

$$\bar{A}_i = (\bar{x}_i \tan \alpha) \quad (157)$$

$$\dot{\bar{m}}_i = (\hat{Z}_i^2 - \bar{S}_0^2) = \pi [\{(\bar{r}_i(\bar{x}) + \bar{A}_i) \cos \mu\}^2 - \{(r_{w_i}(\bar{x}) + \bar{A}) \cos \mu\}^2] \bar{\rho} \bar{U} \cos \mu \quad (158)$$

6.3 CASES

A selected number of cases from a typical shuttle trajectory (see Section 7) were covered in the correlations and subsequent calculations. Flight conditions for these cases, which span a Mach number range from 9.61 to 30.2 and an angle-of-attack range from 30 to 34°, are shown in Table 6-1. Although the correlations were obtained for a limited angle-of-attack range they are expected to be valid over a much wider range.

TABLE 6-1

NAR BASELINE TRAJECTORY

Case Number	U_∞ (kfps)	Altitude (kft)	M_∞	α°	t (sec)
1	25.6	300	30.2	34	250
2	25.4	250	28	34	400
3	23.9	238	25.1	33.3	600
4	21.8	224	22	32.3	800
5	18.7	201	17.9	31.1	1000
6	14.6	181	13.6	30.2	1200
7	10.4	164	9.61	30	1400

6.4 EQUATION OF STATE

The state relations for the equilibrium air shock layer calculations were correlated from the normal shock parameters given in the Cornell Aero Lab tables prepared by Witliff and Curtiss (Ref. 63). These are based on the 1959 ARDC Model Atmosphere.

The equation of state model is a particularly simple form yielding surprising accuracy in hypersonic equilibrium blunt body shock layer calculations of many investigators. In particular we use the form suggested by Swigart (Reference 64) in his 1963 theoretical investigation of the blunt body angle of attack problem in equilibrium air

$$\bar{h} = \frac{\gamma}{\gamma - 1} \frac{\bar{p}}{\bar{\rho}} + \bar{A}_0 \quad (159)$$

$$\bar{h} = h/u_\infty^2 \quad \bar{p} = p/\rho_\infty u_\infty^2$$

$$\bar{A}_0 = A_0/u_\infty^2 \quad \bar{\rho} = \rho/\rho_\infty$$

where γ is an effective caloric ratio on a particular adiabat (shock entry point) and \bar{A}_0 is the energy deviation from polytropic due to equilibrium gas phase chemistry.

The current range of calculations correlate within about 5 percent maximum deviation from the shock table values to the following forms

$$\bar{A}_0 = .098 * (M^*)^{-.77} \quad , \quad 12 \leq M_\infty^* \leq 31 \quad (160)$$

$$\bar{A}_0 = 0. \quad , \quad M_\infty^* < 12$$

$$\gamma = 1.5 * (M_\infty^*)^{-.085} \quad , \quad 9.5 \leq M_\infty^* \leq 31 \quad (161)$$

The effective shock Mach number, M_{∞}^* for the angle of attack cases is given by

$$M_{\infty}^* = M_{\infty} \cos \Lambda \quad (162)$$

These shock state correlations are altitude invariant over the range of altitudes treated in the 7 cases (Table 6-1). The shock Mach number range of applicability is recorded with Equations (160) and (161).

6.5 BODY SURFACE AND SHOCK SURFACE REPRESENTATIONS

To insure smoothness in both local body surface slope and curvature, the body surface was represented by a connected sequence of five second order polynomials. The representation is initiated at the generator axis intercept at the shuttle nose ($\bar{x} = 0$). Avoidance of higher order polynomial representations or alternate functionals insured timely smooth surface profile and derivative generation without embarking on a lengthy process of tedious analytical smoothing. The body generator equation in the windward pitch plane is

$$\bar{r}_w^2 = a + b\bar{x} + c\bar{x}^2 \quad (163)$$

TABLE 6-2

BODY COEFFICIENTS

Section	\bar{x}	a	b	c	
I	[0, 0.525]	0.	1.92059	-0.84868	
II]0.525, 2.60]	0.2550	0.94915	0.07651	
III]2.60, 15.2[-0.40705	1.45843	-0.02143	
IV]15.2, 46.5[3.11583	0.99502	-0.00619	
V	[46.5, 80[$\bar{r}_w (46.5)^2$	0.	0.	(cylinder)

The symbols [a, ,b[indicate whether or not the range limits a,b are included or excluded from the interval, respectively. No attempt was made to fit the boat tail region.

The body and shock curves were based on extensive wind tunnel shadowgraph measurements of shuttle profiles at angle of attack reported in previous Aero-therm analysis (Reference 65). These data were supplemented by experimental shadowgraph traces reported by Marvin et al. (Reference 66) and numerically exact inviscid angle of attack model shuttle calculations presented by Rakich and Kutler (Reference 67).

A particularly significant factor in the development of the shock shape correlation for angle of attack shuttle flow fields was the observation that the geometrical relationships between body and shock surface were invariant despite changes to the angle of attack. The angle of attack effects on shock transition variables between about 25° and 50° positive pitch were recoverable by rotation of an assumed fixed shock surface-body surface unit. The shock stand-off adjustment was correlated by accounting for Mach number change with density jump across the rotated shock.

A set of relations for predicting the local shock stand-off at a specified body station, together with the shock shape equations, (151) through (155), are sufficient to generate the shock surface of a given Mach number, altitude and angle of attack of interest. The stand-off correlations are as follows.

In the "afterbody" region ($\bar{x} \geq 1$.) the ratio of the "baseline" ($M_\infty = 9.61$, $\alpha = 30^\circ$, altitude = 164 kft) to its value at the generator axis is computed in three segments:

$$\begin{aligned} (\bar{\delta}_B / \bar{\delta}_O) &= f(\bar{x}) = 0.139 + 0.891 \bar{x} & 1. < \bar{x} \leq 15. \\ (\bar{\delta}_B / \bar{\delta}_O) &= f(\bar{x}) = 7.7 + 0.387 \bar{x} & 15 \leq \bar{x} \leq 46.5 \\ (\bar{\delta}_B / \bar{\delta}_O) &= f(\bar{x}) = -10.24 + 0.773 \bar{x} & 46.5 < \bar{x} \end{aligned} \quad (164)$$

The baseline "deltas" may then be corrected for the particular Mach number altitude and angle of attack

$$\frac{\delta}{\delta_B} = \left(1 + \left(\frac{\bar{\delta}_O - \bar{\delta}_{BO}}{\bar{\delta}_O} \right) \cos \Lambda \right) \quad (165)$$

The effective shock angle, Λ , was introduced previously.

In the foregoing Equation (165) the dimensionless normal shock wave stand-offs, $\bar{\delta}_O$ and $\bar{\delta}_{BO}$ (for the particular and baseline cases) are computed from the hypersonic similarity spherical shock expansion written in terms of the inverse of the normal shock wave density ratio, ϵ

$$\bar{\delta}_O = \frac{\phi_\epsilon}{1 - \phi_\epsilon} \quad (166)$$

$$\phi_\epsilon \equiv \epsilon - \sqrt{\frac{8}{3}} \epsilon^{3/2} + 3\epsilon^2 + a(\epsilon^3)$$

In the forebody region the shock stand-off variation from its value at the generator axis, $\bar{\delta}_O$, to its value at the shifted stagnation point, $\bar{\delta}_{SP}$, on the windward side is correlated by combining the results of Kaattari (Reference 68) and Swigart (Reference 64). First compute the radial position of the forward stagnation point

$$(\bar{r}_w)_{SP} = 1.34 \sin \alpha - 0.682 \sin^{2.2} \alpha \quad (167)$$

Next compute the variation in stand-off from $\bar{r}_w = 0$ to $(\bar{r}_w)_{SP}$

$$\bar{\delta} = \bar{\delta}_O - (\bar{r}_w \bar{\delta}_O) \left(\frac{1}{\bar{\delta}_O} \frac{d\bar{\delta}}{d\bar{r}_w} \right) \quad 0 < \bar{r}_w \leq (\bar{r}_w)_{SP} \quad (168)$$

where

$$\frac{1}{\bar{\delta}_0} \frac{d\bar{\delta}}{d\bar{r}_w} = 0.94 \sin \alpha - 0.046$$

Over the short distance between forebody stagnation point and the after-body range correlated by Equation (164), a linear growth of stand-off correlates the data

$$\bar{\delta} = \bar{\delta}_{SP} + (\bar{\delta}(1) - \bar{\delta}_{SP}) \left(\frac{\bar{x} - \bar{x}_{SP}}{1 - \bar{x}_{SP}} \right) \quad (169)$$

Two additional dimensionless metrics, the shock wave normal, $\tilde{N}(\bar{x})$ and the shock wave tangent metric, \tilde{C} , are used in the shock relations developed subsequently. Both depend on the derivative of the shock wave trace $\partial\tilde{x}/\partial\bar{r}_\delta$, as does the local shock slope. This derivative is obtained as follows. Combine Equations (151) and (152) obtaining

$$\tilde{x} = \bar{x} + \bar{\delta}_0 - \cot \theta_w (\bar{r}_\delta - \bar{r}_w)$$

Differentiate and rearrange, obtaining

$$\tilde{x}' \equiv \left(\frac{\partial\tilde{x}}{\partial\bar{r}_\delta} \right) = \bar{x}' + (\bar{r}_\delta - \bar{r}_w) \csc^2 \theta_w \left(\frac{d\theta_w}{d\bar{r}_\delta} \right) + \cot \theta_w \left(\frac{d\bar{r}_\delta}{d\bar{r}_w} - 1 \right) \quad (170)$$

Differentiate Equation (151) and neglecting terms $\theta(\epsilon)$ or smaller we obtain

$$\frac{d\bar{r}_w}{d\bar{r}_\delta} = 1 + \theta(\epsilon) \quad (171)$$

and $d\theta_w/d\bar{r}_w$ can be obtained directly

$$\frac{d\theta_w}{dr_w} \equiv \left(\frac{d\theta_w}{d\xi} \right) \left(\frac{d\xi}{dr_w} \right) = \bar{\kappa}_w(\xi) \frac{d\xi}{dr_w} = \bar{\kappa}_w \sqrt{1 + (\bar{x}')^2} \quad (172)$$

Introducing (171) and (172) into (170) the expression used for the required derivative is obtained

$$\tilde{x}' = \bar{x}' + \bar{\kappa}_w(\bar{r} - \bar{r}_w) \sqrt{1 + (\bar{x}')^2} / \sin^2 \theta_w \quad (173)$$

For $\theta_w > 0$

and $\bar{x}' = 0$, for $\theta_w = 0$

The body slope, \bar{x}' and the body curvature $\bar{\kappa}_w$ are obtained directly from differentiating Equation (163).

A comparison of the accuracy of the shock and body correlation vs measured values is presented in the following graphs.

Figures 6-5, 6-6, and 6-7 show comparisons of computed vs measured (shadowgraph) traces of the shock slope supported by the shuttle model bodies (Reference P1 and P3). The more sensitive body and shock slope results are compared in Figure 6-7. Figures 6-5 and 6-6 show the overall results and details restricted to the forebody region respectively. Profile 2, is the selected body shape function generated by the coefficients in Table 6-1.

6.6 COMPUTATION OF THE SHOCK TRANSITION VARIABLES

In the generalized body-oriented coordinate systems for the shock layer previously introduced, a formal development of the jump relations is obtained. The metric direction normal and tangential to the shock surface are readily determined in terms of the foregoing body and shock surface relations and their derivatives. With this information, the remaining shock transition variables are readily computed for shock intercepts in terms of arbitrary body stations \bar{x} , selected for the analysis.

Formulation of the shock relations are an extension of the previously reported NASA supported work of References 69 and 70 with modifications suggested by the formulation of Webb et al., (Reference 71).

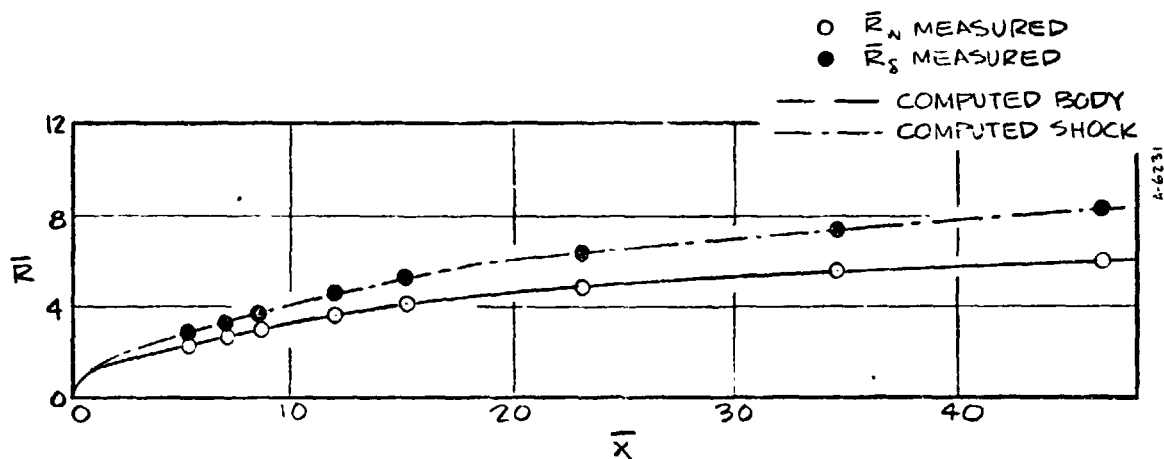


FIGURE 6-5 COMPARISON OF SHOCK AND BODY SURFACE CORRELATIONS VS. SHADOWGRAPH MODEL WIND TUNNEL VALUES $\alpha = 30^\circ$ $M_\infty = 7.4$

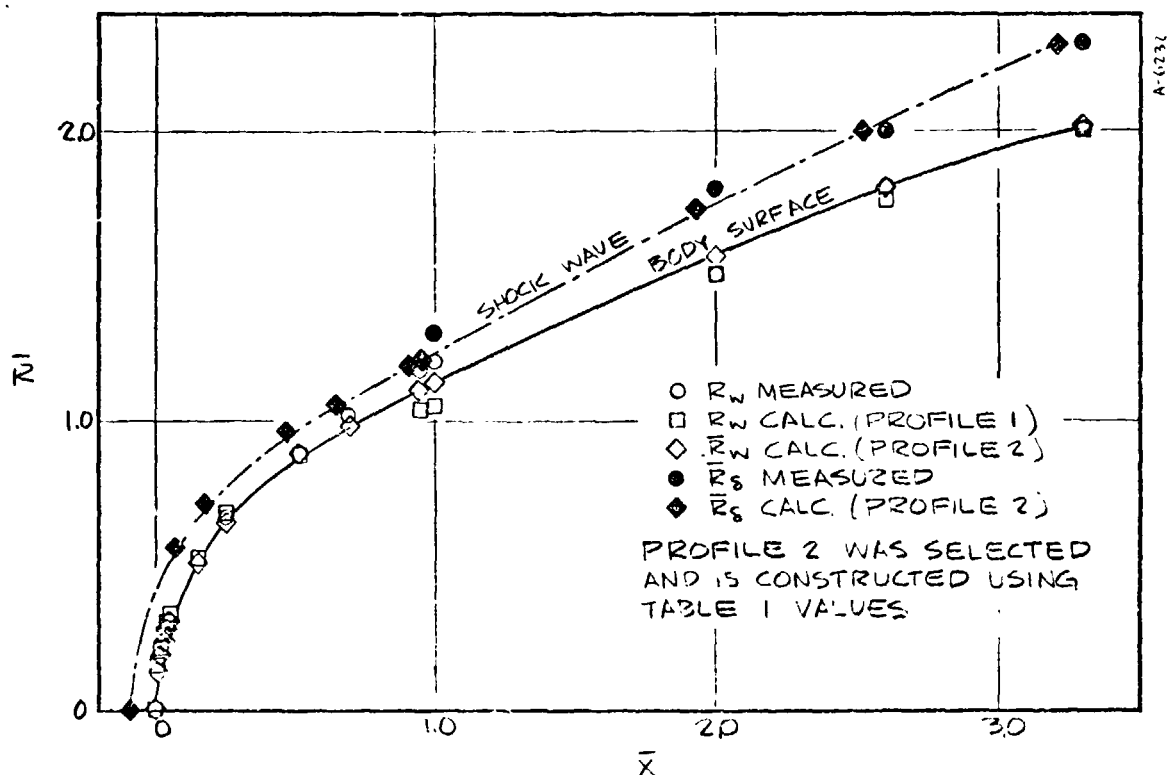


FIGURE 6-6 COMPARISON OF SHOCK AND BODY SURFACE CORRELATIONS VS. SHADOWGRAPH MODEL WIND TUNNEL VALUES (REF. P1 AND P3) $\alpha = 30^\circ$, $M_\infty = 1.4$. DETAILS OF FOREBODY REGION

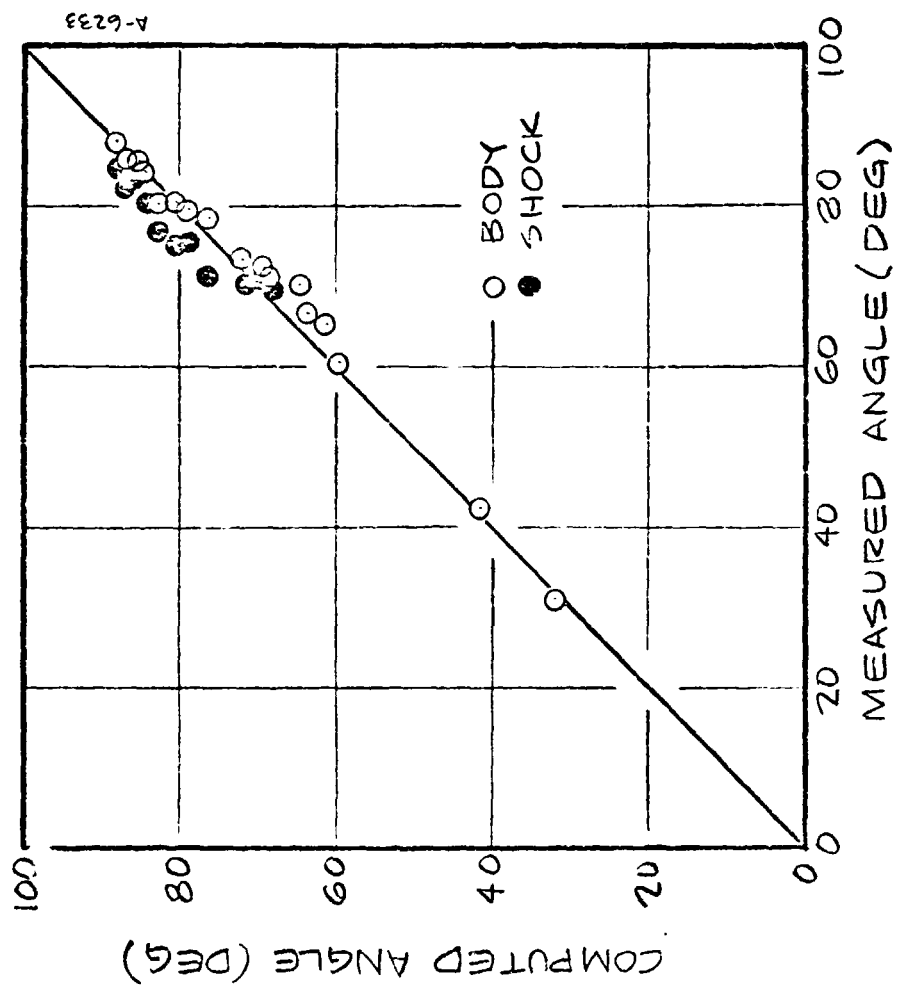


FIGURE 6-7 COMPARISON OF MEASURED VS CORRELATION COMPUTED SHOCK WAVE AND BODY ANGLES

Reference is made to the principal axis vector direction cosines shown in Figure 6-8, the geometry introduced in Figures 6-1 and 6-2 and the non-dimensional scheme used for the flow quantities, introduced in Section 2.

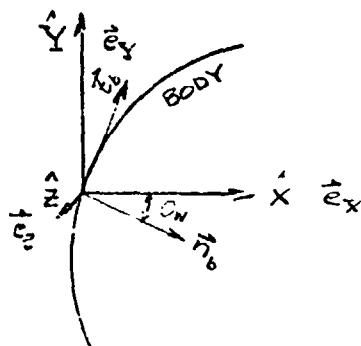


Figure 6-8 Direction Cosines

We choose $\vec{e}_\phi = -\vec{e}_Z$, where ϕ is the azimuthal angle and the direction metric is outward.

The direction cosines are written

$$\begin{array}{ll} \text{(body normal)} & \vec{n}_b = \vec{e}_X \cos \theta_b - \vec{e}_Y \sin \theta_b \end{array} \quad (174)$$

$$\begin{array}{ll} \text{(body tangent)} & \vec{t}_b = \vec{e}_X \sin \theta_b + \vec{e}_Y \cos \theta_b \end{array}$$

$$\begin{array}{ll} \text{(binormal)} & \vec{b}_b = -\vec{e}_Z = -\vec{e}_\phi \end{array}$$

Multiplying \vec{n}_b by $\cos \theta_b$ and \vec{t}_b by $\sin \theta_b$ and adding, yields for \vec{e}_X

$$\vec{e}_X = \vec{n}_b \cos \theta_b + \vec{t}_b \sin \theta_b \quad (175)$$

Multiplying \vec{n}_b by $-\sin \theta_b$ and \vec{t}_b by $\cos \theta_b$ and adding, yields for \vec{e}_Y

$$\vec{e}_Y = -\vec{r}_b \sin \theta_b + \vec{t}_b \cos \theta_b \quad (176)$$

While, quite simply

$$\vec{e}_\phi = -\vec{b}_b \quad (177)$$

The normal and tangent surface metrics of a shock surface $\tilde{X}(r_\delta, \phi)$ arbitrarily oriented in our body geometry for positive angle of attack may then be written

$$\begin{aligned} \tilde{N} &= \left(1 + \tilde{x}'^2 \right)^{1/2} \\ \tilde{C} &= \cos \alpha + \sin \alpha \left(\tilde{x}' \right) \end{aligned} \quad (178)$$

The derivative of the shock trace is obtained using Equation (173), the ϕ derivatives are neglected close to the plane of symmetry on the windward side.

The free stream velocity can next be decomposed into components exterior and tangent (\vec{t}_δ) or normal (\vec{n}_δ) to the shock surface at angle of attack, under the pitch plane symmetry simplification. See, for example, Reference 71.

The components are

$$(U_\infty)_{n_\delta} = \left(\frac{\tilde{C}U_\infty}{\tilde{N}} \right) \left(\frac{1}{\tilde{N}} \right) \left(\vec{e}_X - \vec{e}_Y \left(\frac{\partial \tilde{X}}{\partial r} \right) \right) \quad (179)$$

$$\vec{n}_b = \left(\frac{1}{\tilde{N}} \right) \left(\vec{e}_X - \vec{e}_Y \left(\frac{\partial \tilde{X}}{\partial r} \right) \right)$$

and

$$(\vec{U}_\infty)_{t_\delta} = U_\infty \left\{ \vec{e}_X \left(\cos \alpha - \frac{\tilde{C}}{\tilde{N}^2} \right) + \vec{e}_Y \left(\tilde{C} \left(\frac{1}{\tilde{N}^2} \right) \frac{\partial \tilde{X}}{\partial r} - \sin \alpha \right) \right\} \quad (180)$$

$$\vec{t}_\delta = \frac{1}{\sqrt{1 - \frac{\tilde{C}^2}{\tilde{N}^2}}} \left\{ \vec{e}_X \left(\cos \alpha - \frac{\tilde{C}}{\tilde{N}^2} \right) + \vec{e}_Y \left(\left(\frac{\tilde{C}}{\tilde{N}^2} \right) \left(\frac{\partial \tilde{X}}{\partial \tilde{r}} \right) - \sin \alpha \right) \right\}$$

To obtain the relations used first write the velocity component directions (179) and (180) in terms of the body direction cosines, equations (175), (176), and (177), obtaining

$$\vec{n}_\delta = \left(\frac{1}{\tilde{N}} \right) \left[\vec{n}_b \left(\cos \theta_b + \sin \theta_b \frac{d\tilde{X}}{d\tilde{r}} \right) - (\tilde{t}_b \cos \theta_b - \vec{n}_b \sin \theta_b) \left(\frac{\partial \tilde{X}}{\partial \tilde{r}} \right) \right] \quad (181)$$

$$\begin{aligned} \vec{t}_\delta = \left(1 - \left(\frac{\tilde{C}}{\tilde{N}} \right)^2 \right)^{-1/2} \left\{ \vec{n}_b \left(\cos \theta_b \left(\cos \alpha - \left(\frac{\tilde{C}}{\tilde{N}^2} \right) \right) - \sin \theta_b \left(\frac{\tilde{C}}{\tilde{N}^2} \left(\frac{\partial \tilde{X}}{\partial \tilde{r}} \right) - \sin \alpha \right) \right. \right. \\ \left. \left. + \tilde{t}_b \left(\sin \theta_b \left(\cos \alpha - \frac{\tilde{C}}{\tilde{N}^2} \right) + \cos \theta_b \left(\left(\frac{\tilde{C}}{\tilde{N}^2} \right) \left(\frac{\partial \tilde{X}}{\partial \tilde{r}} \right) - \sin \alpha \right) \right) \right\} \quad (182) \end{aligned}$$

Now the free stream vector velocity may be expressed compactly in terms of the developed normal and tangential metric coefficients, Equations (181) and (182).

$$\vec{U}_\infty = \left(U_\infty \frac{\tilde{C}}{\tilde{N}} \right) \vec{n}_\delta + \left(U_\infty \sqrt{1 - \tilde{C}^2/\tilde{N}^2} \right) \vec{t}_\delta \quad (183)$$

The Rankine-Hugoniot relations for an oblique shock wave are summarized as

$$\begin{aligned} u_\delta &= \epsilon u_\infty & h_\delta &= h_\infty + \frac{u_\infty^2}{2} (1 - \epsilon^2) \\ v_\delta &= v_\infty & \epsilon &= \frac{\rho_\infty}{\rho_\delta} \\ p_\delta &= p_\infty + \rho_\infty u_\infty^2 (1 - \epsilon) & & \end{aligned} \quad (184)$$

For computation we combine the foregoing metric expression for the free stream velocity, Equation (183), the Rankine-Hugoniot relations, Equation (184) and the equation of state, Equation (159), obtaining the relations in order of their calculation. For any selected station \tilde{x} , following calculation of all of the body surface and shock surface variables compute

$$\epsilon = \frac{\rho_\infty}{\rho_\delta} = \frac{G_2 \left(1 + \frac{\bar{p}_\infty}{D_1}\right) - \sqrt{G_2^2 \left(1 + 2 \frac{\bar{p}_\infty}{D_1} + \left(\frac{\bar{p}_\infty}{D_1}\right)^2\right) - (4G_2 - 2) \left(\frac{1}{2} + \frac{\bar{h}_\infty}{D_1} - \frac{\bar{A}_0}{D_1}\right)}}{(2G_2 - 1)} \quad (185)$$

$$\bar{u}_\delta = \sin \theta_w \left[\cos \alpha - \frac{\tilde{C}}{\tilde{N}^2} (1 - \epsilon) \right] - \cos \theta_w \left[\sin \alpha - \frac{\tilde{C}}{\tilde{N}^2} \tilde{x}' (1 - \epsilon) \right] \quad (186)$$

$$\bar{v}_\delta = -\sin \theta_w \left[\sin \alpha - \frac{\tilde{C}}{\tilde{N}^2} \tilde{x}' (1 - \epsilon) \right] - \cos \theta_w \left[\cos \alpha - \frac{\tilde{C}}{\tilde{N}^2} (1 - \epsilon) \right] \quad (187)$$

$$\bar{p}_\delta = \bar{p}_\infty + \left(\frac{\tilde{C}}{\tilde{N}}\right)^2 (1 - \epsilon) \quad (188)$$

$$\bar{h}_\delta = \bar{h}_\infty + \left(\frac{1}{2}\right) \left(\frac{\tilde{C}}{\tilde{N}}\right)^2 (1 - \epsilon^2) \quad (189)$$

and

$$G_2 = \frac{\gamma}{\gamma - 1}, \quad D_1 = \left(\frac{\tilde{C}}{\tilde{N}}\right)^2$$

In addition we compute the total pressure at the local streamline intersection with the shock front

$$\bar{p}_{T_\delta} = \bar{p}_\delta + \frac{1}{2} \epsilon^{-1} (\bar{u}_\delta^2 + \bar{v}_\delta^2) \quad (190)$$

and the total enthalpy

$$\bar{H}_{T_\delta} = \bar{h}_\delta + \frac{1}{2} (\bar{u}_\delta^2 + \bar{v}_\delta^2) \quad (191)$$

Using these to form the streamline to streamline correlation ratios

$$\frac{\bar{P}}{\bar{P}_{T\delta}} \quad \text{and} \quad \frac{\bar{h}}{\bar{h}_{T\delta}}$$

Equations (185) through (191), the shock surface and body surface relations and a streamtube integration of the streamwise momentum were calculated for the 7 trajectory points using a desk calculator and the correlation relations for 9 streamlines.

6.7 STREAMTUBE CHEMICAL RELAXATION

The streamtube code was developed to interface with the BLIMP/KINET code and the prescribed pressure distribution presented in previous sections. By matching mass flow rates it is thus possible to approximate both nonequilibrium chemistry and variable entropy at the edge of the boundary layer. Although any available reacting streamtube code could be used, the code described below was written so that the calculation of thermochemical data would be identical to that used in BLIMP/KINET. Thus there would be no incompatibilities in the chemistry. The computational procedure is implicit and is therefore numerically stable even for large step sizes.

The equations to be solved are the combined energy and momentum equation

$$\frac{dh}{ds} = \frac{1}{\rho} \frac{dp}{ds} \quad (192)$$

and a set of $n-1$ specie equations

$$\frac{d}{ds} (SP_i) = \frac{1}{\rho u} \phi_i \quad (193)$$

subject to the constraints that

$$H_T - h = \frac{u^2}{2}$$

$$h = \sum_{i=1}^n h_i$$

(194)

$$\sum_{i=1}^n SP_i = 1$$

Let m denote the spatial station along the streamtube and ℓ be the iteration at station m . Then a Newton-Raphson procedure was used to solve the above equations. Assume that the solution is known at $m-1$ (which could for instance be the initial conditions) then the independent variables h and SP_i at station m for the ℓ -th iteration is related to the known $m-1$ station and $\ell-1$ iteration by the equations

$$\begin{aligned} \Delta h \left\{ 1 + \frac{\Delta s}{2} \left(\frac{1}{\rho^2} \frac{\partial \rho}{\partial h} \frac{dp}{ds} \right)_{n-1} \right\} + \sum_{i=1}^n \frac{\Delta s}{2} \left(\frac{1}{\rho^2} \frac{\partial \rho}{\partial SP_i} \frac{dp}{ds} \right)_{n-1} \Delta SP_i \\ = - \left\{ h_{m,n-1} - \frac{\Delta s}{2} \left(\frac{1}{\rho} \frac{dp}{ds} \right)_{n-1} - HHH_{m-1} \right\} \end{aligned} \quad (195)$$

$$\begin{aligned} \Delta h \left\{ \frac{\Delta s}{2} \left[\left(\frac{\phi_i}{\rho} \frac{1}{u^2} \frac{\partial u}{\partial h} \right) - \frac{1}{u} \frac{\partial}{\partial h} \left(\frac{\phi_i}{\rho} \right) \right] \right\} + \Delta SP_i \\ - \left\{ \sum_{i=1}^n \frac{\Delta s}{2} \frac{1}{u} \frac{\partial}{\partial SP_i} \left(\frac{\phi_i}{\rho} \right) \Delta SP_i \right\} = - \left\{ SP_{i,n-1} - \frac{\Delta s}{2} \frac{\phi_i}{\rho u} - (SPP_i)_{m-1} \right\} \end{aligned} \quad (196)$$

where

$$\begin{aligned}
 \Delta h &= h_{m,\ell} - h_{m,\ell-1} \\
 \Delta SP_i &= (SP_i)_{m,\ell} - (SP_i)_{m,\ell-1} \\
 \Delta s &= s_m - s_{m-1} \\
 HHH_{m-1} &= \left\{ h_{m-1} + \frac{\Delta s}{2} \left(\frac{1}{\rho} \frac{dp}{ds} \right)_{m-1} \right\} \\
 (SPP_i)_{m-1} &= \left\{ (SP_i)_{m-1} + \frac{\Delta s}{2} \left(\frac{\phi_i}{\rho u} \right)_{m-1} \right\}
 \end{aligned} \tag{197}$$

Equations (195) and (196) represent n equations with an equal number of unknowns, namely $\Delta h, \Delta SP_1, \Delta SP_2 \dots \Delta SP_{n-1}$. Implicit unknowns are

$$\begin{aligned}
 \rho &= \rho(SP_i, h, p) \\
 T &= T(SP_i, h, p) \\
 \phi_i &= \phi_i(T, SP_i, p) \\
 u &= u(h)
 \end{aligned} \tag{198}$$

Equations (195) and (196) are solved iteratively with a step size constraint based simply on the number of iterations required to obtain a converged solution.

SECTION 7

CALCULATIONS FOR REPRESENTATIVE SHUTTLE VEHICLE

For these calculations nonequilibrium chemistry in both the inviscid and viscous regions were considered. Pitch plane calculations were made for the windward side of the Rockwell International orbiter (Figure 7-1) at flight conditions representative of their 2007 baseline trajectory (Figure 7-2). The pitch plane outline of the vehicle at angle of attack was assumed to be the generator of an axisymmetric body with a shock shape determined from correlations of wind tunnel shadowgraphs (Reference 65).

A simple-in-theory but involved-in-practice procedure was used to estimate the nonequilibrium and nonisentropic conditions at the edge of the boundary layer. The following steps were required for each trajectory point.

1. Calculate body pressure distribution
2. For a prescribed shock shape, estimate the pressure distribution along various streamlines in the inviscid flow.
3. For each streamline, starting with a frozen oblique shock state, chemically relax along the prescribed pressure-distance history to yield the thermochemical state along each streamline.
4. Estimate the boundary layer mass flow using equilibrium assumptions and compare with the mass flow represented by each streamline to determine where that streamline should enter the boundary layer. Then from 3 the thermochemical state at the edge of the boundary layer is known.

The current inviscid flow calculations are not applicable in the stagnation region except in an integrated sense. In fact no streamline approach would be valid on the stagnation line for nonequilibrium conditions because of the zero velocity limit. Thus, the nonequilibrium solution in the stagnation region was

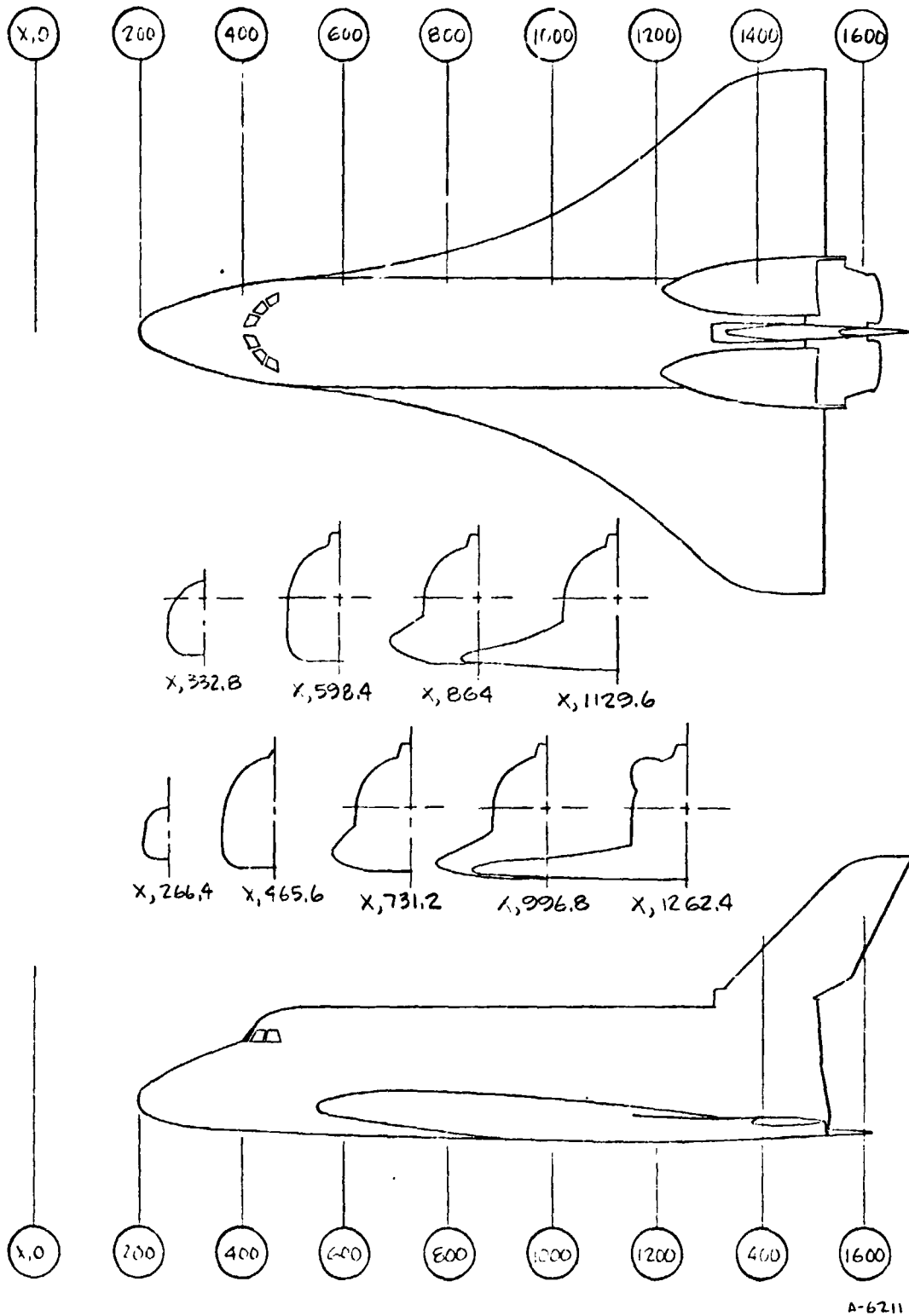


FIGURE 7-1 SHUTTLE GEOMETRY

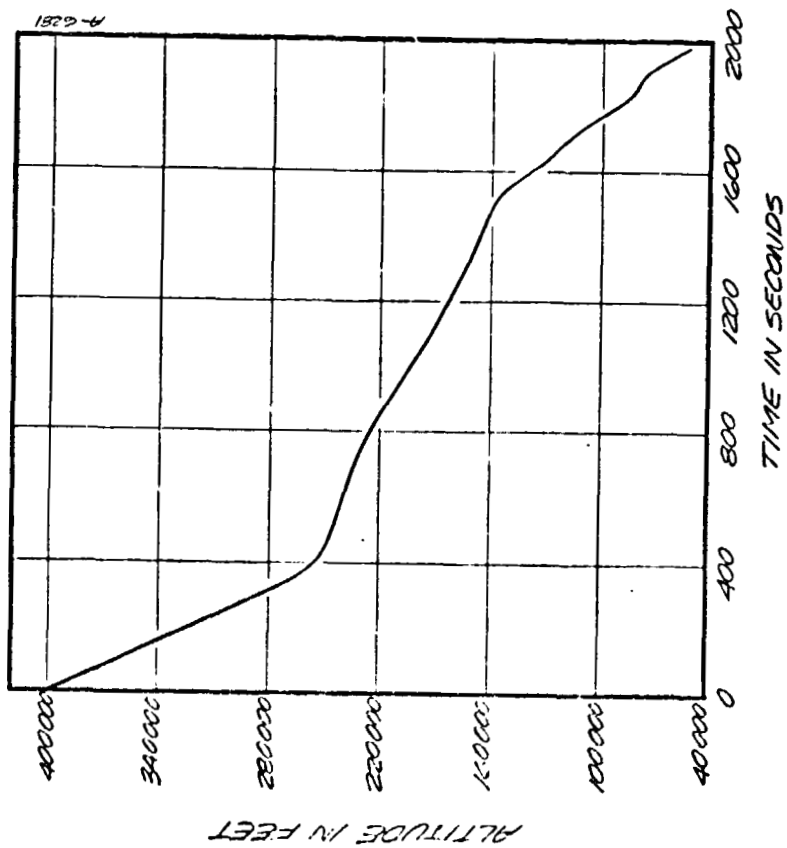


FIGURE 7-2A RI 2007 BASELINE TRAJECTORY.

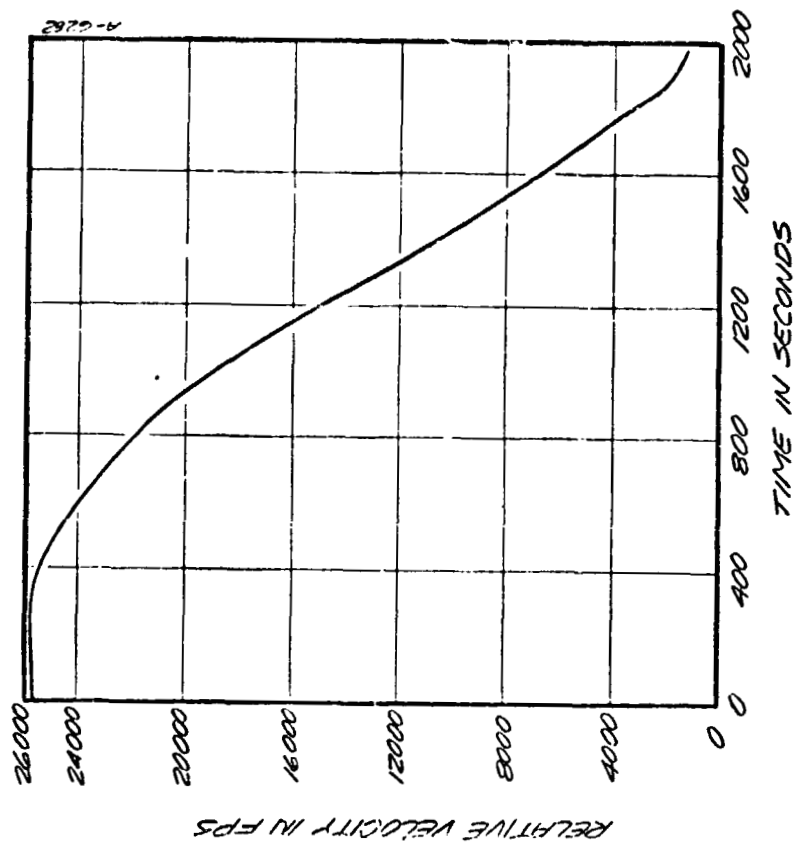


FIGURE 7-2B RI 2007 BASELINE TRAJECTORY.

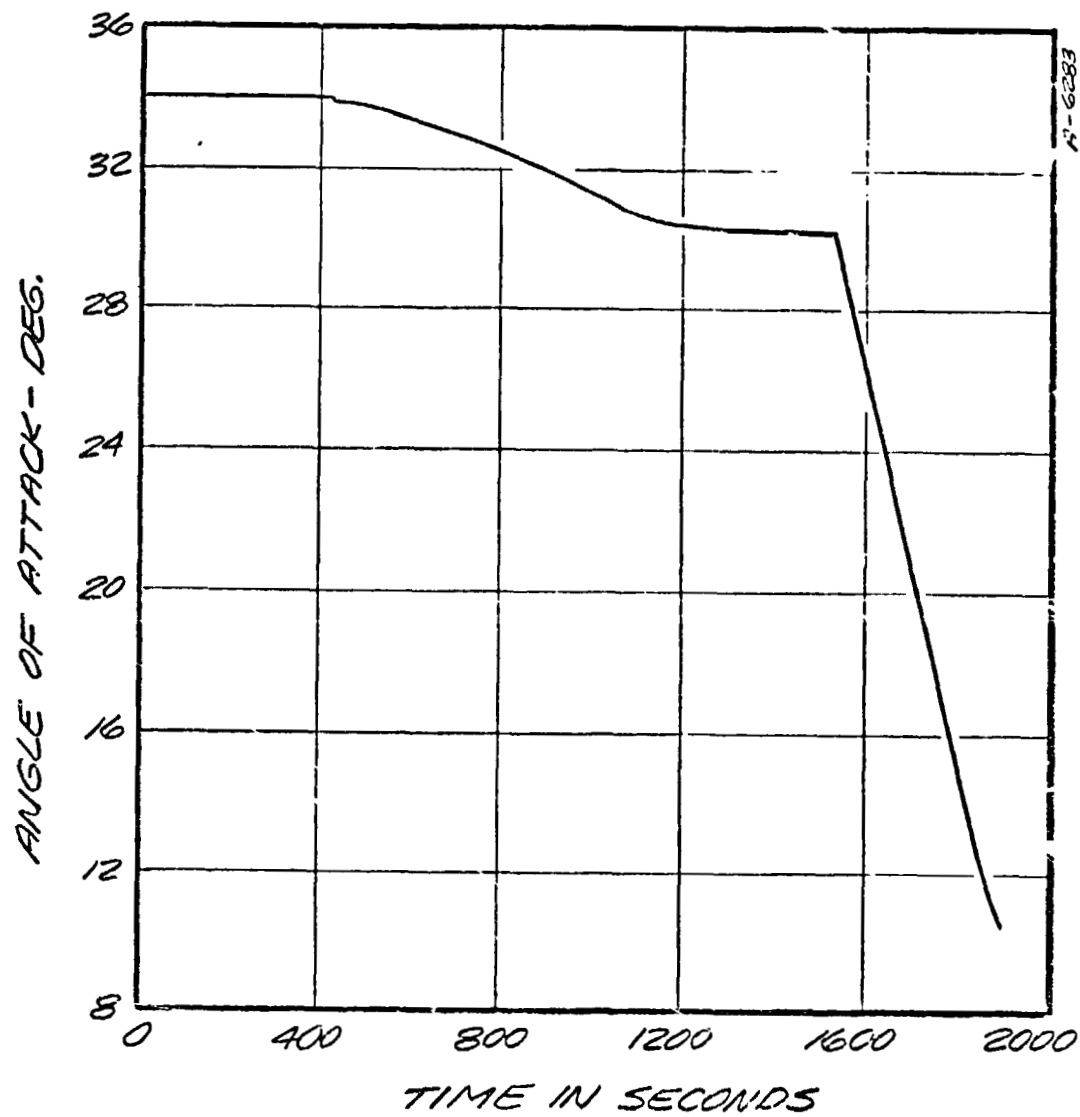


FIGURE 7-2C RI 2007 BASELINE TRAJECTORY.

calculated using a viscous shock layer option and these solutions were then matched with the solution from (4) above to use as the edge conditions for a boundary layer calculation.

7.1 SURFACE PRESSURE DISTRIBUTIONS AND APPROXIMATE BOUNDARY LAYER MASS FLOW RATE

Surface pressure distributions for the cases given in Table 6-1 were computed using the modified correlations presented in Reference 71a and are shown in Figure 7-3. Similar distributions could be calculated via a smooth transition from modified Newtonian values in the vicinity of the nose to local tangent cone values downstream as suggested in Reference 65. With these pressure distributions, boundary layer calculations* were used to determine the boundary layer characteristics on an equivalent axisymmetric body. Since axial symmetry was assumed, the mass flow rate at any given body station is defined and can be related to a stream tube mass flow. Typical mass flow rates for 4 cases are shown in Figure 7-4. Of the cases given in Table 6-1, only cases 1, 2, 4 and 7 ($t = 250, 400, 800, 1400$ seconds) were considered for complete heating analysis.

7.2 VISCOUS SHOCK LAYER SOLUTIONS IN THE STAGNATION REGION

Since chemical reactions along an inviscid stagnation streamline are not well defined, the BLIMP/KINET viscous shock layer option was used to determine the thermochemical state in the shock layer. A noncatalytic wall was assumed since primary interest was in the state at some point which would represent the edge of the boundary layer. It was also assumed that the shock wave was chemically frozen. A typical set of distributions for $t = 800$ seconds is shown in Figure 7-5 through 7-7 for three body stations. The rapid dissociation immediately downstream of the shock wave is evident however the remainder of the shock layer is not very reactive. Similar shock layer solutions were obtained for $t = 250, 400$, and 1400 seconds for estimating boundary conditions as described in Section 7-4.

7.3 STREAMLINE PRESSURE AND ENTHALPY CALCULATIONS

The enthalpy, pressure, density, and velocity components were computed for 9 selected streamline entrances at the shock front including the body streamline. These streamline shock jump conditions and a determination of the pressure expansion

*Integral boundary layer calculations were used here, however any reliable procedure including the BLIMP code could be used.

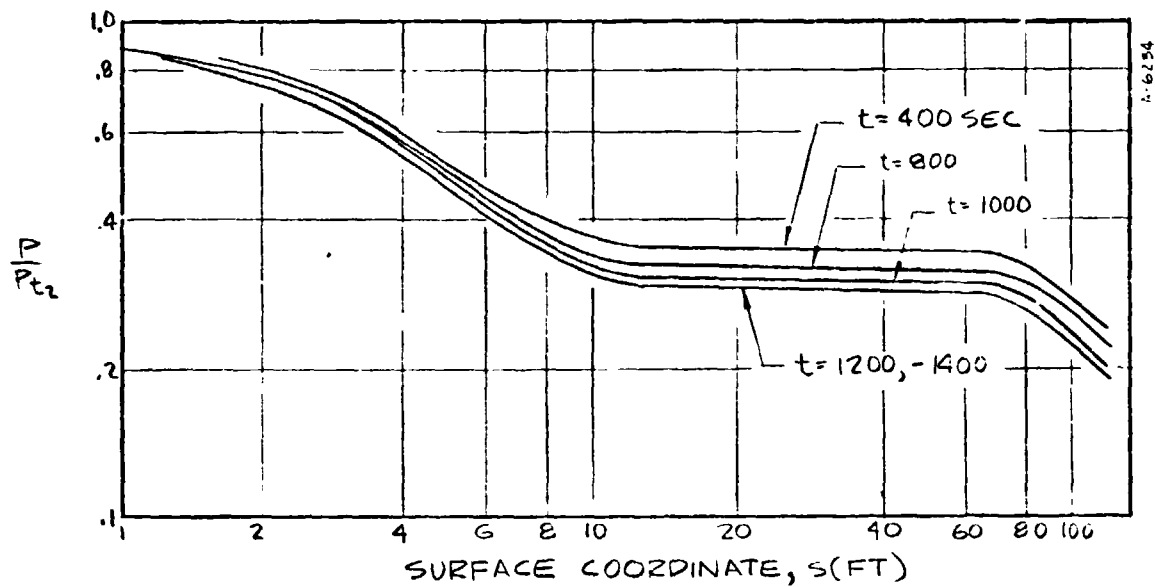


FIGURE 7-3 SURFACE PRESSURE DISTRIBUTION, WINDWARD CENTERLINE

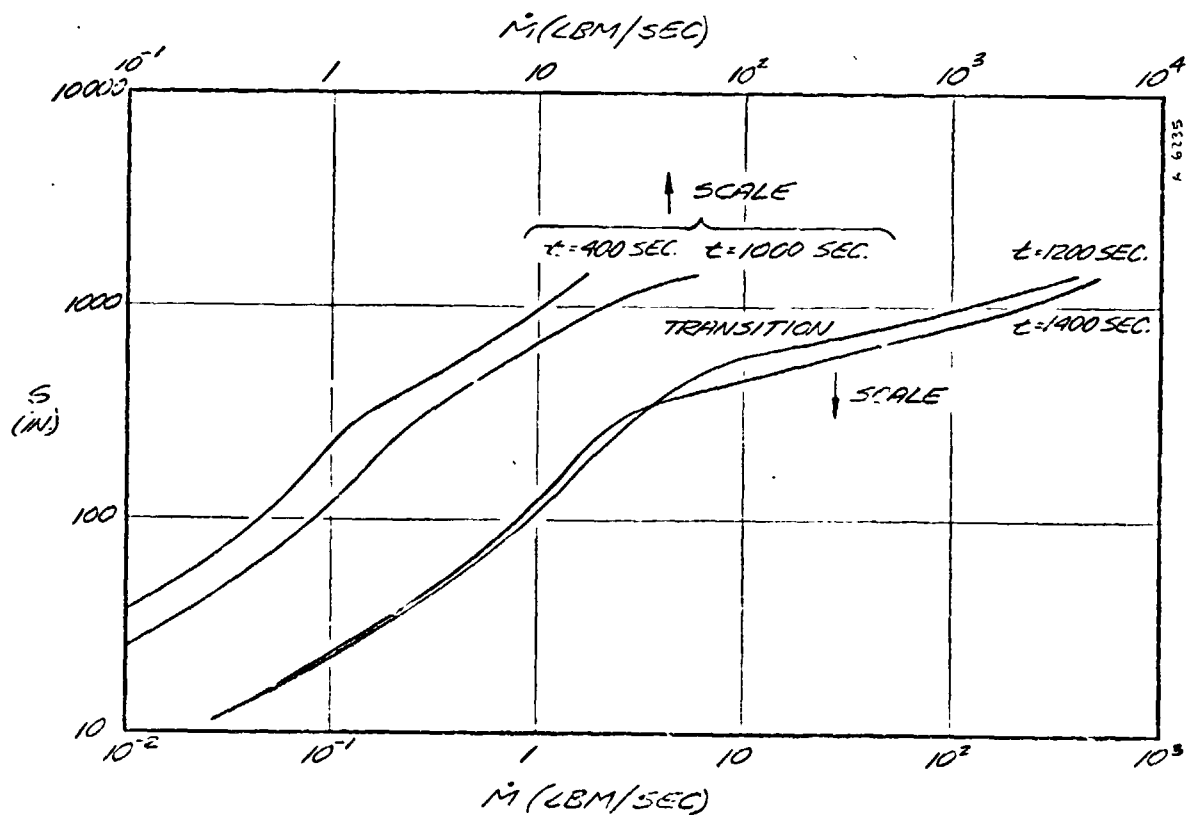


FIGURE 7-4 APPROXIMATE BOUNDARY LAYER MASS FLOW RATES.

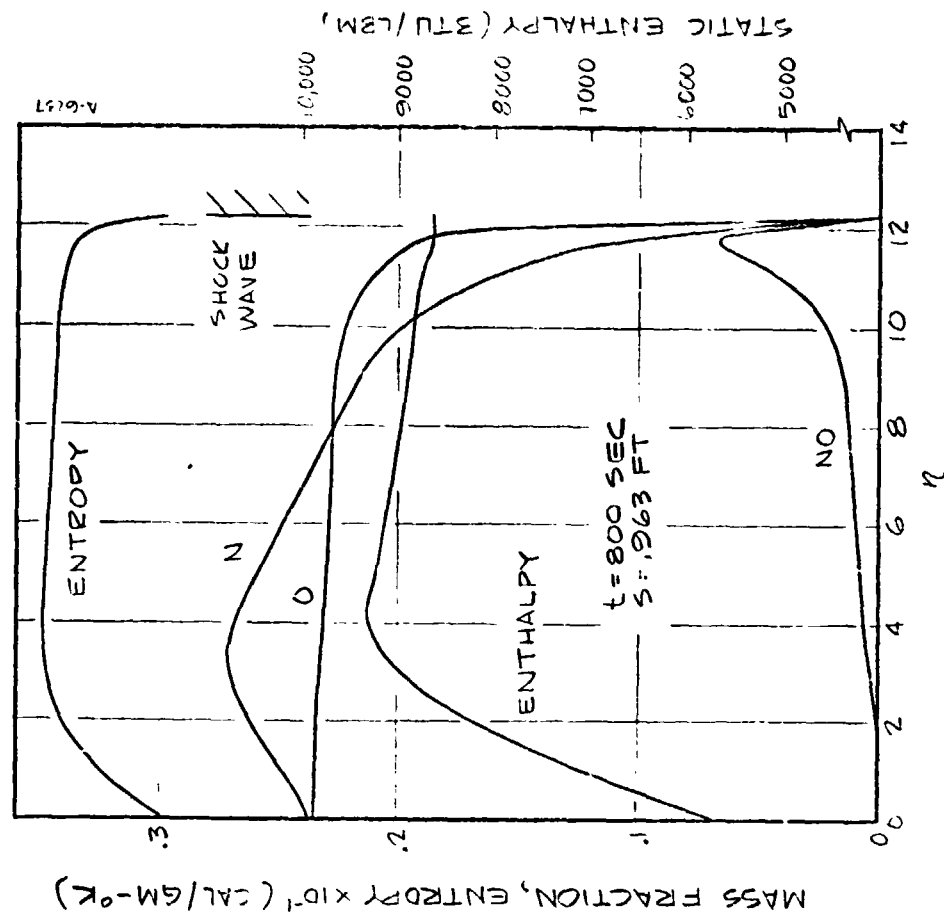


FIGURE 7-6 VISCOUS SHOCK LAYER

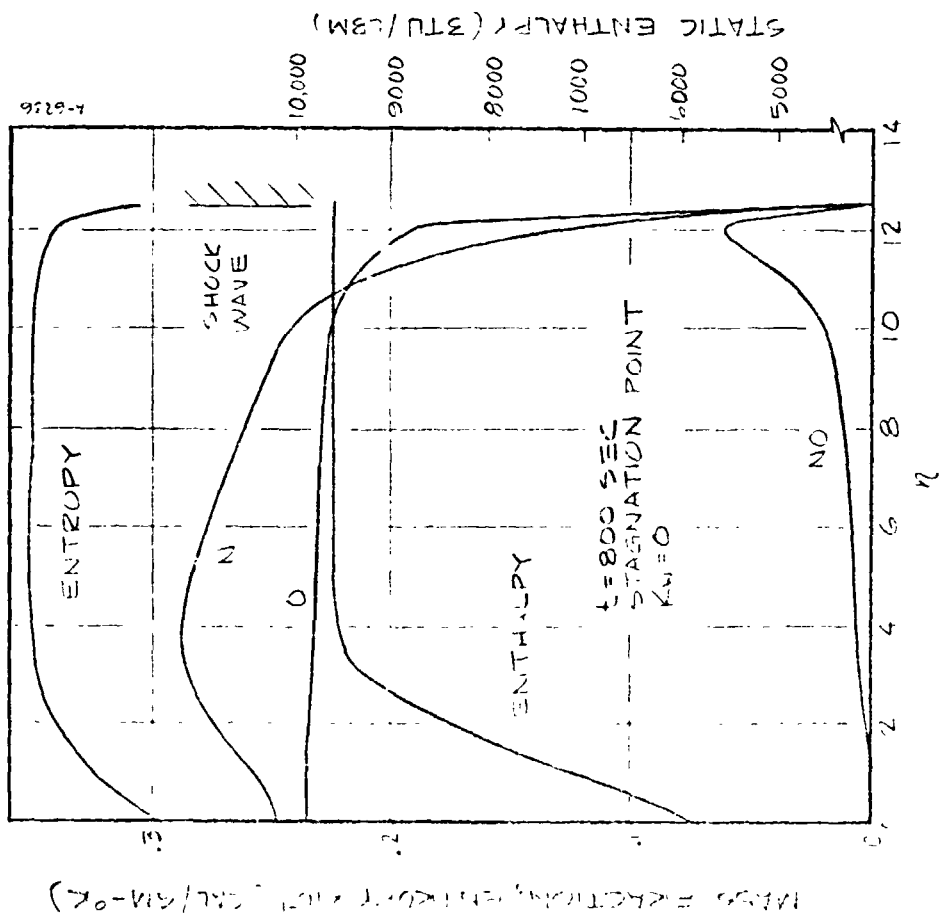


FIGURE 7-5 VISCOUS SHOCK LAYER

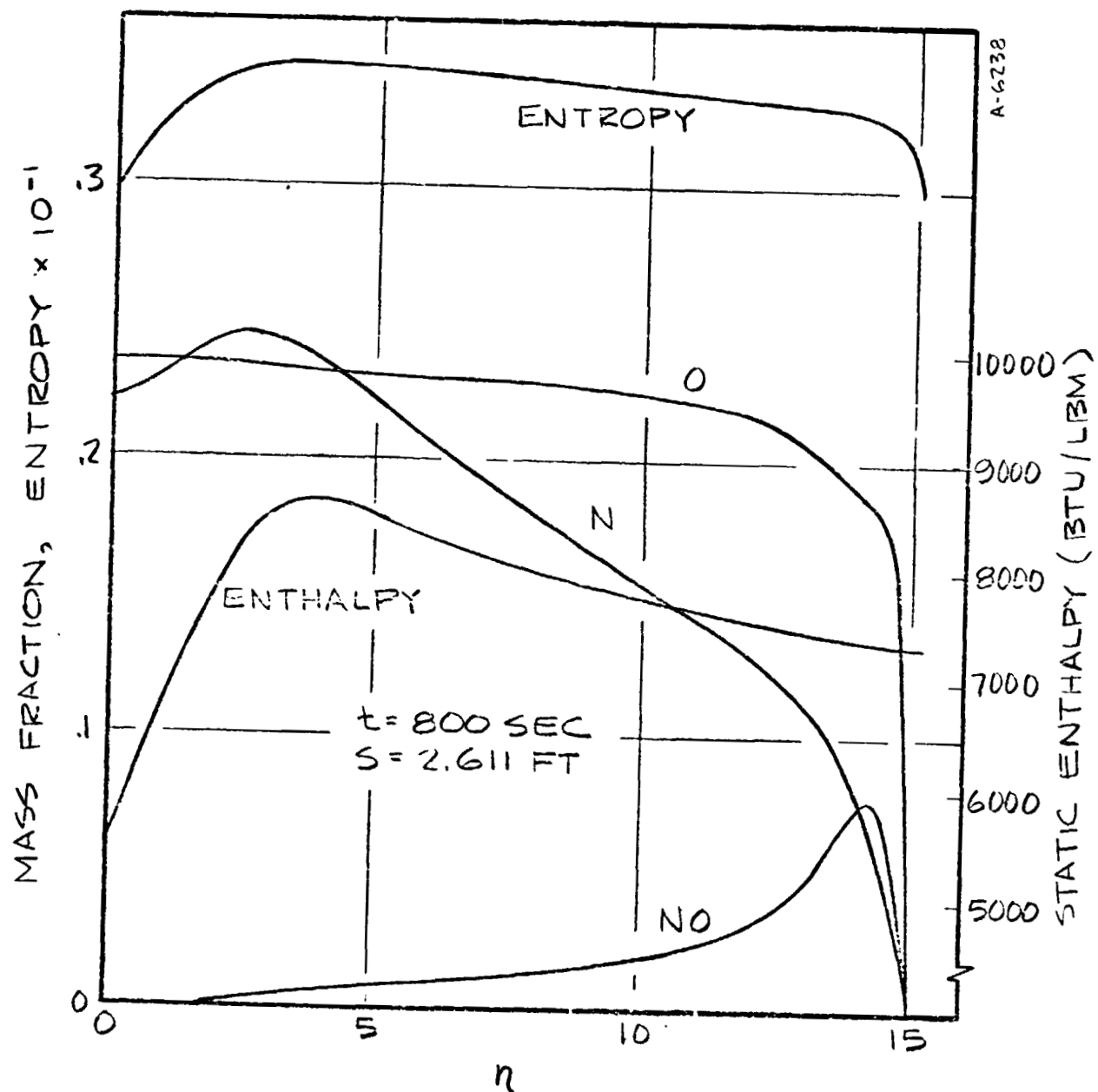


FIGURE 7-7 VISCOUS SHOCK LAYER

downstream on individual stream tubes provided the initial and boundary conditions for the subsequent flow field chemistry and reacting boundary layer solutions.

The jump conditions are computed at arbitrarily selected positions on the computed shock surface from the shock relations developed in the previous section. In the presented analysis, the ratios \bar{P}_2/\bar{P}_{T2} , \bar{H}_2/\bar{H}_T , $\bar{\rho}_2$, \bar{u}_2 , and \bar{v}_2 were found to be useful parameters for application to the subsequent code solutions.

From the shock wave surface relations, equations 151 through 158 and Equation (173), the parameters $\bar{\delta}$, $\bar{\kappa}_\delta$, θ_δ , \tilde{x}_δ , \tilde{x}_δ' , \bar{r}_δ are obtained. Next the initial sweep or arc of the streamline as it departs from the shock correlates simply as the sector of a characteristic circumscribed semicircle in the forebody (and tends to zero in the afterbody)

$$S_\delta \approx \frac{\pi R_o \bar{\delta}}{2 R_o}$$

$$\xi_\delta = \frac{\pi \bar{\delta}}{2} \quad (199)$$

The normal displacement,

$$\bar{y} = \frac{y - y_w}{y_\delta - y_w}$$

of any streamline is next computed for all streamlines which entered the shock upstream of the shock station being computed. This is accomplished using Equation (158) to determine the dimensionless mass flow, \bar{m} for all streamlines. The procedure is, as follows. Consider a streamline entering the shock at the jth station. the upstream entering streamlines (J-1, J-2, ...) have normal displacements, measured at the jth station, given by

$$\frac{\bar{y}_{J-1}}{\bar{\delta}_J} = \sqrt{\bar{m}_{J-1}/\bar{m}_J}, \quad \frac{\bar{y}_{J-2}}{\bar{\delta}_J} = \sqrt{\bar{m}_{J-2}/\bar{m}_J}, \quad \dots \quad (200)$$

The streamline path lengths are then computed,

$$(\xi_{J-N})_J = \frac{\pi \bar{\delta}_{J-N}}{2} + \sum_{K=J-N}^J \left\{ (\tilde{x}_K - \tilde{x}_{K-1})^2 + (\bar{y}_K - \bar{y}_{K-1})^2 \right\}^{\frac{1}{2}} \quad (201)$$

A plot of the calculated streamline path lengths as a function of body station axial coordinate \bar{x} appears in a previous section (Figure 6-2).

To compute the pressure distribution along the streamlines correlative procedures were developed. Observations derived from wind tunnel data and exact numerical inviscid flow field calculations were used as a basis for the procedure and relations developed.

A regularity in the body surface pressure distribution for both adiabatic and non-adiabatic shock layers supported by long, analytically smooth, blunt-nosed body surface profiles at zero angle of attack has been exploited in many inviscid flow analyses. In particular, under a NASA sponsored study Buckingham and Hoshizaki (Reference 72) showed that for affinely related power law bodies with slenderness ratios ($L/D > 3$) series correlations exist for both pressure and convective heat transfer that are independent of both Mach number and altitude. These correlations are verifiable for a restricted but useful range of hypersonic reentry trajectories. The profiles, which possess spherical, oblate and prolate ogival, or paraboloid noses generate correlatable pressure distributions. Success of the correlations depended, in part, on treating the pressure distribution as a ratio of the local pressure to the total pressure on the streamline, P/P_T .

From studies of exact numerical inviscid flows on shuttle vehicles at angle of attack (Rakich and Kutler, Reference 67) experimental wind tunnel shuttle data (Marvin et al Reference 66) and the extensive data tabulated by Bartlett, Morse, and Tong at Aerotherm (Reference 65), the constancy of the ratio P/P_T on each streamline along normal \bar{y} at a particular body station may be noted. Some results of previous theoretical studies, using exact numerical method of characteristics and finite difference solutions help to substantiate this observation. For instance, Figures 7-8 and 7-9 are for axisymmetric flow past an ogive ($L/D = 3.5$) and sphere-cone-cylinder ($L/D = 12$) method of characteristics with equilibrium air (Reference 73). Similar results have been obtained by reducing the profile data of Rakich and Kutler (Reference 67) and experimental data presented by Marvin (Reference 66). Significant deviation from constant P/P_{T2} along a normal was restricted to the forebody region of this representative sample of both

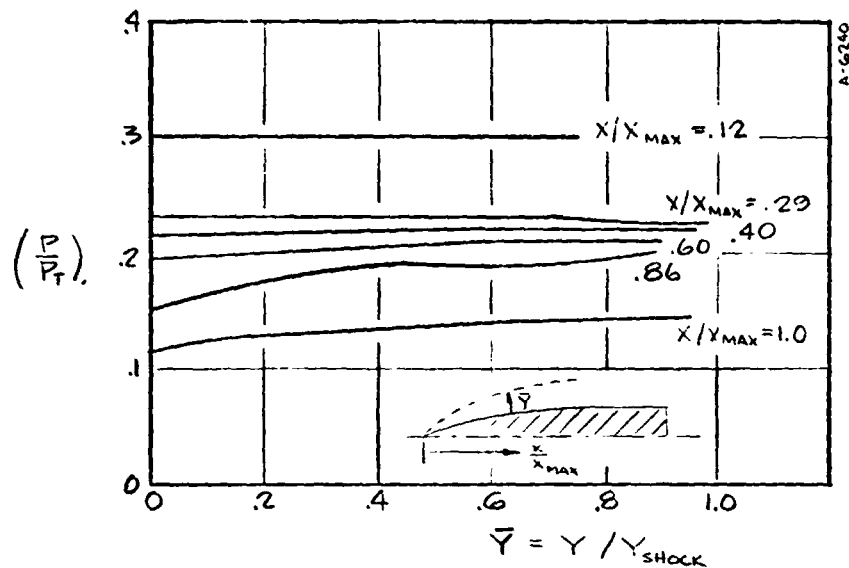


FIGURE 7-8 PRESSURE ACROSS THE SHOCK LAYER, METHOD-OF-CHARACTERISTICS, OGIVE FINENESS RATIO 3.5, $M_\infty = 2.$, $\alpha = 0$

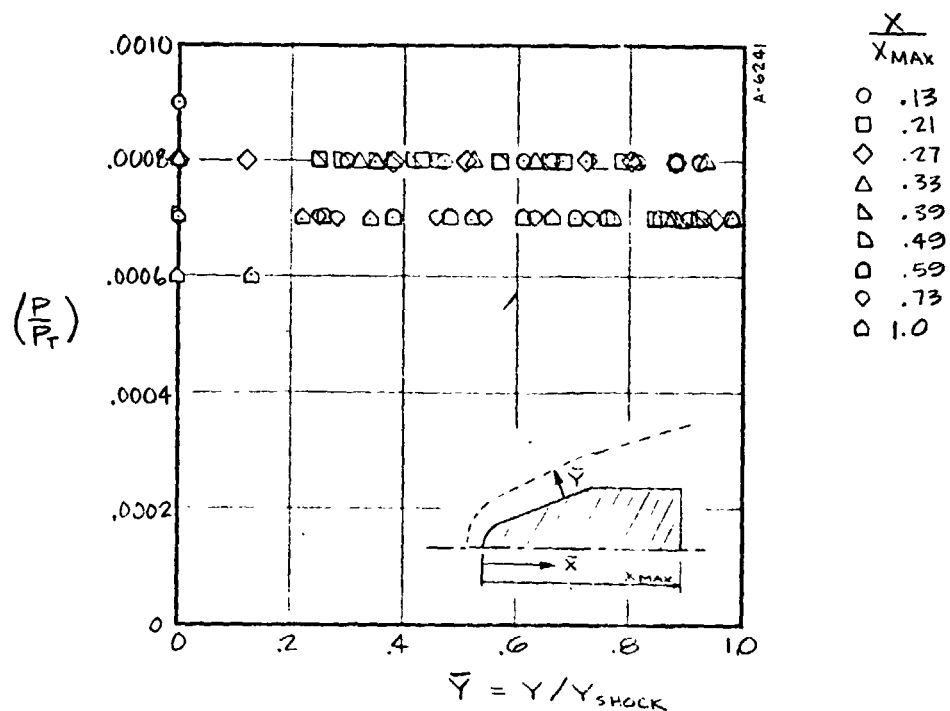


FIGURE 7-9 PRESSURE ACROSS THE SHOCK LAYER, METHOD OF CHARACTERISTICS, SPHERE CONE CYLINDER BODY, FINENESS RATIO 12.0, $\alpha = 0$, $M_\infty = 6.0$

shuttle and shuttle-like slender bodies of revolution at various angles of attack. To anticipate these results examine the X and Y inviscid momentum equations. For the adopted coordinate system, in dimensionless terms, these are:

$$\bar{\rho} \bar{u} \frac{\partial \bar{u}}{\partial \bar{\xi}} + (1 + \bar{\kappa} \bar{y}) \bar{\rho} \bar{v} \frac{\partial \bar{u}}{\partial \bar{y}} = - \frac{\partial \bar{p}}{\partial \bar{\xi}} \quad (202)$$

$\bar{\rho}_0 \quad \bar{\rho}_0$

$$\bar{\rho} \bar{u} \frac{\partial \bar{v}}{\partial \bar{\xi}} + \bar{\rho} \bar{v} \frac{\partial \bar{v}}{\partial \bar{y}} - \frac{\kappa \bar{\rho} \bar{u}^2}{(1 + \bar{\kappa} \bar{y})} = - \frac{\partial \bar{p}}{\partial \bar{y}} \quad (203)$$

$\bar{\rho}_0 \quad \bar{\rho}_0 \quad \bar{\rho}_0$

Dropping terms $O(\epsilon)$ with respect to terms retained in the shock layer it is seen that we recover the usual stream tube and normal momentum equations.

Dividing (202) by the total pressure on the streamline and integrating, along the body surface from the stagnation point yields

$$p(\xi)/p_T - 1 = - \left(\frac{1}{1 + (2p(\xi)/\bar{\rho} \bar{u}^2)} \right)$$

which in the forebody as $\xi \rightarrow 0$ approaches the stagnation limit

$$\lim_{\xi \rightarrow 0} p(\xi)/p_T - 1 = 0 \Rightarrow \frac{p(\xi)}{p_T} \rightarrow 1$$

In the afterbody as $\xi \rightarrow \infty$ the pressure approaches the vacuum limit (the stream tube "fault", unlimited decay of momenta)

$$\lim_{\xi \rightarrow \infty} \frac{p(\xi)}{p_T} - 1 = -1 \Rightarrow \frac{p(\xi)}{p_T} \rightarrow 0$$

So that an expected solution of the stream tube momentum equation subject to these limits near the stagnation point (variable area S_ξ) would have the form

$$\frac{dP}{P} + \frac{dS_\xi}{S_\xi} \approx 0 \Rightarrow \frac{(d\xi)^N}{\xi^N} = - \frac{dP}{P} \quad (204)$$

$$\text{or } \frac{dP}{P} = - Nd \ln(\xi)$$

$$\text{or } \left(\frac{P}{P_T}\right)_{\bar{y}=0} = 1 - \text{Constant} * \xi^N \quad (204)$$

Equation (204) is clearly inappropriate for the stream tube at large ξ . However, as noted, an asymptotic limit pressure must be applied to insure that the stream tube expansion limit is not exceeded.

The dependence on curvature may be deduced from an integration of the y momentum equation, Equation (203) following division by the total pressure.

$$\int_0^{\bar{\delta}} \frac{\partial(\frac{P}{P_T})}{\partial \bar{y}} d\bar{y} = \int_0^{\bar{\delta}} \frac{\bar{\kappa} \bar{\rho} \bar{u}^2}{\bar{\rho} \bar{u}^2 + 2P} d\bar{y} \quad (205)$$

$$\text{For } \xi \rightarrow \infty \quad \bar{\rho} \bar{u} \rightarrow \infty \quad \text{and } \left(\frac{P}{P_T}\right)_{\xi} = f(y) = \bar{\kappa}_{\delta} \bar{\kappa}_w = 0 \quad (206)$$

Hence p/p_T may be expected to approach a constant value along a given normal. The strong entropy layer effect on pressure is absorbed by using the ratio of the local pressure to the "local" streamtube total pressure.

For $\xi \rightarrow 0$ on the other hand, $\bar{\rho} \bar{u}^2 \rightarrow 0$ and from (205)

$$\left(\frac{P}{P_T}\right)_{\xi} = f(\bar{y}) + (\bar{\kappa}_{\delta} - \bar{\kappa}_w) \bar{\delta} \quad (207)$$

Or the total pressure variation in the forebody is linearly dependent on the curvature variation. In our simplification it is assumed to vary proportional to \bar{y} .

The present results correlate in the form implied by Equation (204). Along the body streamline we find

$$\left(\frac{P}{P_T}\right)_{\bar{y}=0} = 1 - 0.247 (\xi)^{0.328} \quad (208)$$

$$\text{For } \left(\frac{p}{p_T}\right) \geq \left(\frac{p}{p_T}\right)_{\text{Limit}} \quad (208)$$

While

$$\left(\frac{p}{p_T}\right)_{\text{Limit}} = \sin^2 \alpha + 0.11 \sin \alpha \quad \text{For } 15^\circ \leq \alpha \leq 53.5^\circ \quad (209)$$

In the shock layer ($0 < \bar{y} \leq \bar{\delta}$) the presented results are adjusted to correlate in accordance with Equation (207)

$$\left(\frac{p}{p_T}\right)_{\bar{y} > 0} = \left(\frac{p}{p_T}\right)_{\bar{y} = 0} * \left[1 - \left(\frac{\bar{\kappa}_w - \bar{\kappa}_\delta}{\bar{\kappa}_w} \right) \left(\frac{\bar{\delta} - \bar{y}}{\bar{\delta}} \right) \right] \quad (210)$$

Here

$$\bar{\kappa}_{w_0} = \bar{\kappa}_w \text{ (maximum)} = \bar{\kappa}_w \text{ } (\bar{x} = 0)$$

The relative invariance of the streamtube pressure correlations to changes in reentry trajectory conditions is illustrated in the accompanying correlation plots Figures 7-10, 7-11 and 7-12 for the 7 cases (trajectory points) previously listed in Table 6-1. On these plots appear the correlation calculations developed by the procedures introduced here plotted against the mean values taken from the references previously listed.

Tables 7-1, 7-2, and 7-3 summarize the numerics for the 7 angle of attack shock layer flow situations treated in the inviscid analysis. The streamtube pressure distributions, in terms of p/p_δ shown in Table 7-2 are virtually invariant over the trajectory range considered in this analysis however Mach number and angle of attack effects are present in the pressures, p_δ/p_{T_0} via the computed local conditions behind the shock wave. These initial conditions behind the shock wave are presented in Table 7 for each trajectory point.

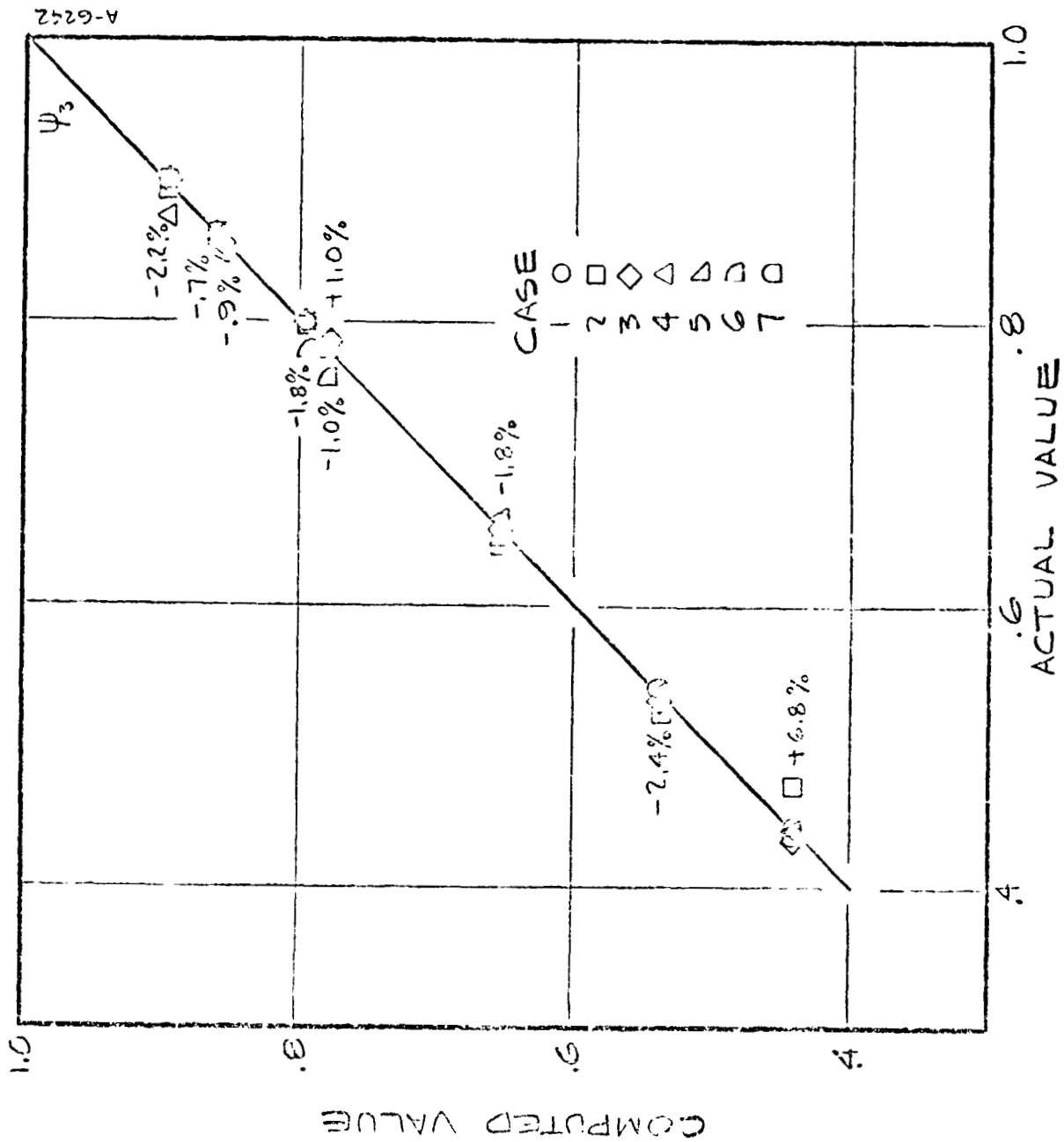


FIGURE 7-10 STREAMTUBE PRESSURE CORRELATION
STREAMLINE 3

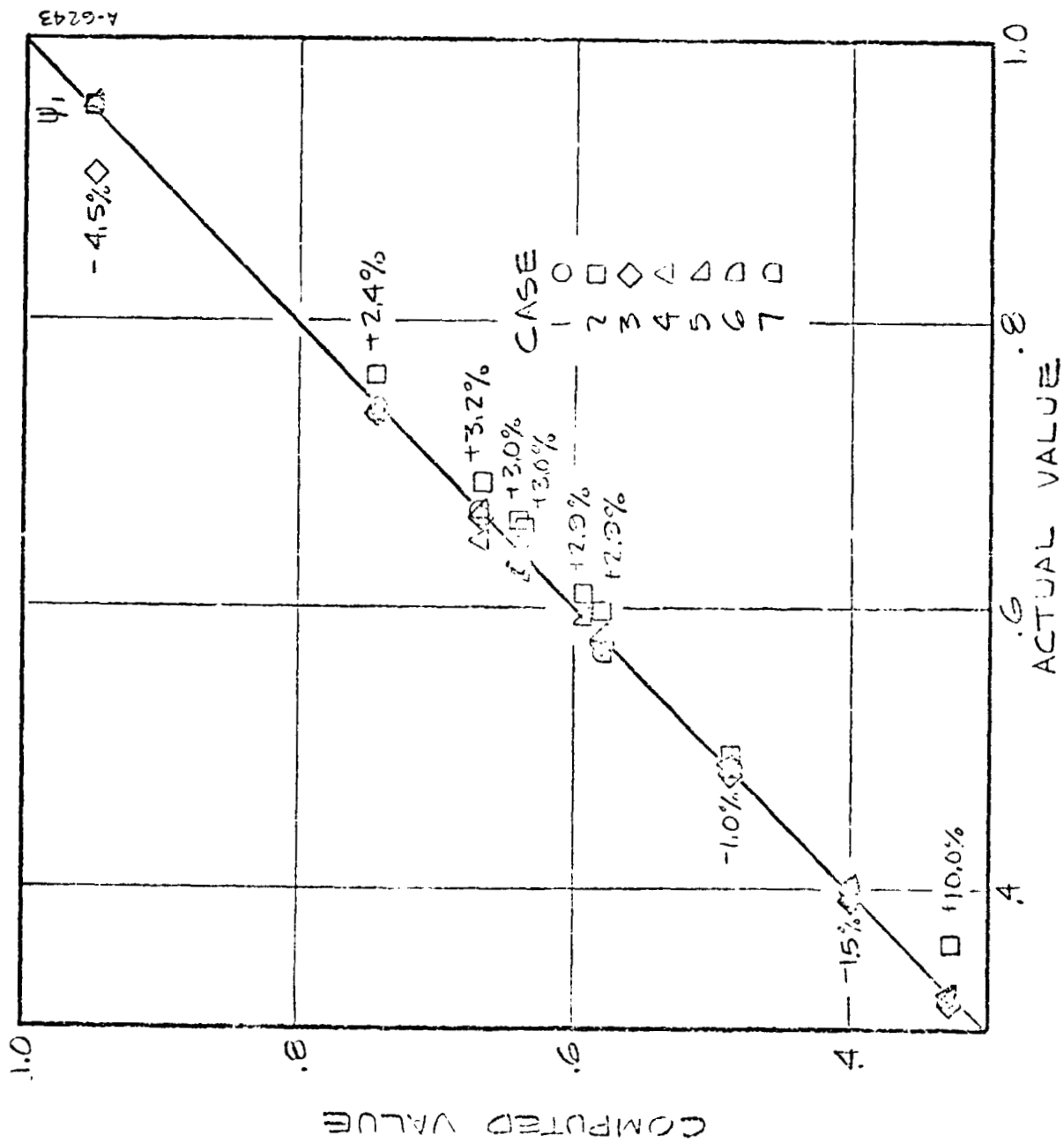


FIGURE 7-11 STREAMTUBE PRESSURE CORRELATION
STREAMLINE 7

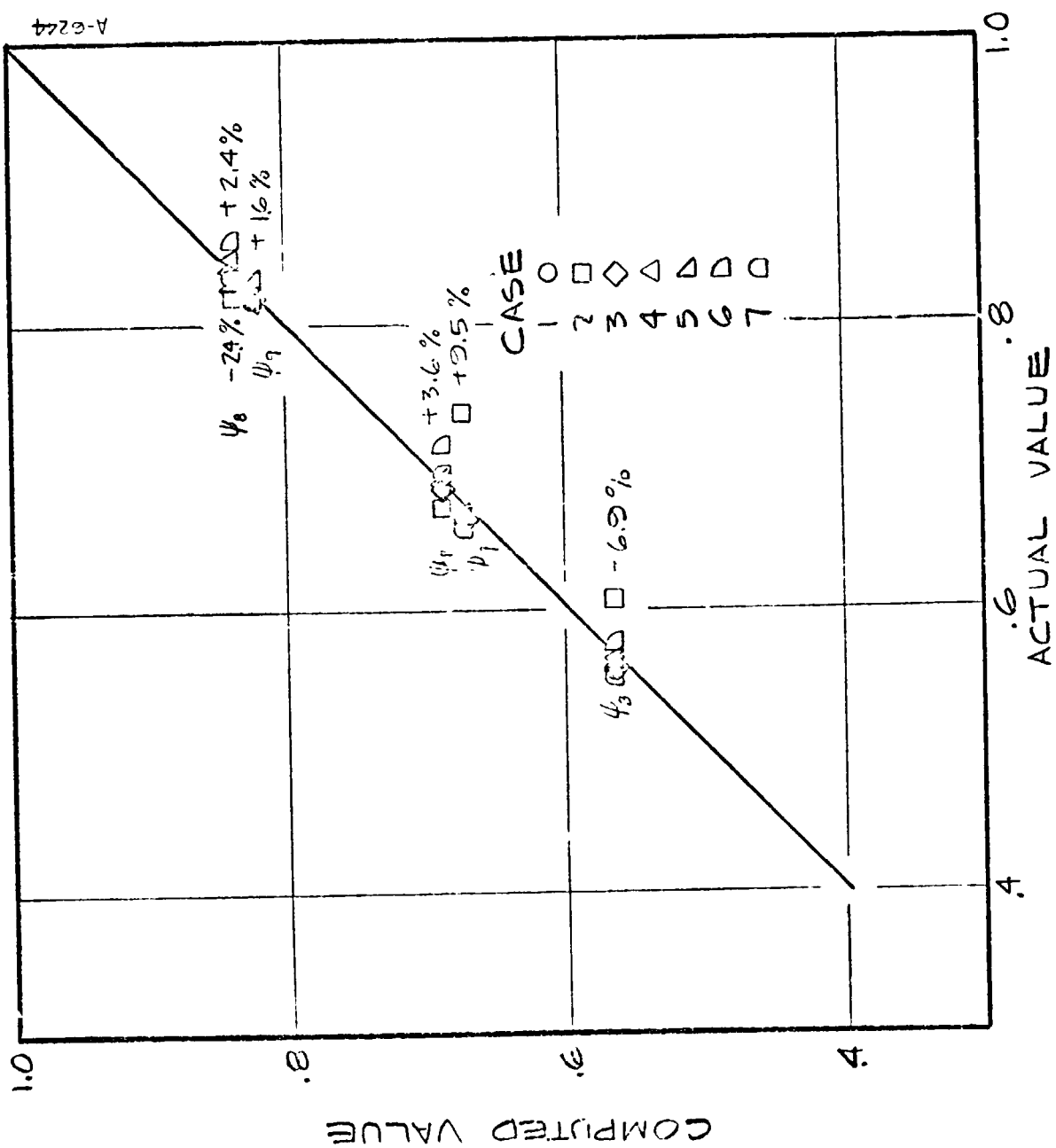


FIGURE 7-12 STREAMTUBE PRESSURE CORRELATION
STREAMLINE 8 AND 9

TABLE 7-1
SHOCK LAYER METRICS

\bar{x}	\bar{r}_δ	\bar{A}	$(\hat{B}_\delta - \hat{B}_{\delta_{sp}})$	\bar{m}
Case # 1 $M_\infty = 30.2$ ALT = 300K FT $\alpha = 34^\circ$				
0.25	0.710	.169	0.180	.102
0.50	0.960	.337	0.526	.809
0.70	1.13	.472	0.779	1.91
0.95	1.30	.641	1.060	3.33
1.0	1.34	.675	1.12	3.94
2.0	1.84	1.35	2.10	13.85
3.3	2.34	2.23	3.24	32.98
7.0	3.34	4.72	6.13	118.05
Case # 2 $M_\infty = 28$ ALT = 254K FT $\alpha = 34^\circ$				
0.25	.710	.169	.180	.102
0.50	.960	.337	.526	.809
0.70	1.13	.472	.779	1.91
0.95	1.30	.641	1.060	3.33
1.0	1.34	.675	1.12	3.94
2.0	1.84	1.35	2.10	13.85
3.3	2.34	2.23	3.24	32.98
7.0	3.34	4.72	6.13	118.05
Case # 3 $M_\infty = 25.1$ ALT = 238K FT $\alpha = 33.3^\circ$				
0.25	.700	.164	.179	.101
0.50	.950	.328	.525	.866
0.70	1.12	.460	.778	1.90
0.95	1.29	.624	1.06	3.53
1.0	1.33	.657	1.12	3.94
2.0	1.83	1.31	2.08	13.59
3.3	2.33	2.17	3.22	32.57
7.0	3.33	4.60	6.09	116.52

\bar{x}	\bar{r}_δ	\bar{A}	$(\hat{B}_\delta - \hat{B}_{\delta_{sp}})$	\bar{m}
Case # 4 $M_\infty = 22$ ALT = 224K FT $\alpha = 32.3^\circ$				
0.25	.690	.158	.186	.109
0.50	.940	.316	.530	.882
0.70	1.11	.442	.780	1.91
0.95	1.28	.600	1.055	3.50
1.0	1.32	.632	1.115	3.91
2.0	1.82	1.26	2.075	13.53
3.3	2.32	2.09	3.195	32.07
7.0	3.32	4.42	6.005	113.30
Case # 5 $M_\infty = 17.9$ ALT = 201K FT $\alpha = 31.1^\circ$				
0.25	.680	.151	.191	.115
0.50	.930	.302	.535	.899
0.70	1.10	.422	.783	1.93
0.95	1.27	.573	1.06	3.53
1.0	1.31	.603	1.12	3.94
2.0	1.81	1.21	2.06	13.33
3.3	2.31	1.99	3.16	31.57
7.0	3.31	4.22	5.92	110.10
Case # 6 $M_\infty = 13.6$ ALT = 181K FT $\alpha = 30.7^\circ$				
0.25	.670	.146	.196	.121
0.50	.920	.291	.537	.906
0.70	1.09	.407	.784	1.93
0.95	1.26	.553	1.055	3.50
1.0	1.30	.582	1.115	3.91
2.0	1.80	1.16	2.045	13.14
3.3	2.30	1.92	3.135	30.88
7.0	3.30	4.07	5.855	107.70
Case # 7 $M_\infty = 9.61$ ALT = 164K FT $\alpha = 30^\circ$				
0.25	0.670	.144	.196	.121
0.50	0.920	.289	.538	.909
0.70	1.09	.404	.785	1.94
0.95	1.26	.546	1.06	3.53
1.0	1.30	.577	1.12	3.94
2.0	1.80	1.155	2.05	13.20
3.3	2.30	1.905	3.13	30.78
7.0	3.30	4.04	5.85	107.51

TABLE 7-2
STREAMTUBE PRESSURE DISTRIBUTION

AXIAL POSITION X/R_0	STREAMLINE DISTANCE, ξ/ξ_0	P/P_0	AXIAL POSITION X/R_0	STREAMLINE DISTANCE, ξ/ξ_0	P/P_0	AXIAL POSITION X/R_0	STREAMLINE DISTANCE, ξ/ξ_0	P/P_0
Streamline # 1 (Stag. Streamline)			Streamline # 3			Streamline # 5		
0.15	0	1.	0.50	0	1.	0.95	0	1.
0.25	0.11	0.947	0.70	0.094	0.895	1.0	0.155	0.994
0.50	0.47	0.744	0.95	0.561	0.860	2.0	1.28	0.923
0.70	0.78	0.666	1.0	0.652	0.855	3.3	2.67	0.965
0.95	1.09	0.640	2.0	1.89	0.744	5.0	4.40	0.838
1.0	1.15	0.636	3.3	3.20	0.778	7.0	6.42	0.759
2.0	2.27	0.591	7.0	6.91	0.653	15.2	14.40	0.623
3.3	3.67	0.579	15.2	15.2	0.536	32.2	30.00	0.511
7.0	7.43	0.486	29.5	30.00	0.440	46.5	46.10	0.511
15.2	16.1	0.399	46.5	46.70	0.440	Streamline # 6		
28.2	30.0	0.327	Streamline # 4			1.0	0	1.
46.5	47.1	0.327	0.70	0	1.	2.0	1.22	0.929
Streamline # 2			0.95	0.330	0.961	3.3	2.61	0.910
0.25	0	1.	1.0	0.395	0.955	5.0	4.35	0.841
0.50	0.32	0.784	2.0	1.47	0.887	7.0	6.38	0.764
0.70	0.64	0.702	3.3	2.80	0.869	15.2	14.20	0.627
0.95	0.99	0.676	7.0	6.61	0.730	32.4	30.00	0.514
1.0	1.04	0.670	15.2	14.80	0.579	46.5	46.00	0.514
2.0	2.09	0.623	31.8	30.00	0.491	Streamline # 7		
3.3	3.42	0.610	46.5	46.40	0.491	2.0	0	1.
7.0	7.30	0.512	Streamline # 8			3.3	1.69	0.980
10.0	10.30	0.478	3.3	0	1.	5.0	3.42	0.901
15.2	15.50	0.420	7.0	5.46	0.822	15.2	14.00	0.675
28.5	30.00	0.345	15.2	14.00	0.675	33.1	30.00	0.553
46.5	47.00	0.345	46.5	45.10	0.553	Streamline # 9		
			7.0	0	1.	7.0	0	1.
			9.0	0.539	0.955	11.0	3.48	0.910
			15.2	8.01	0.821	20.0	13.00	0.784
			35.0	29.40	0.673	46.5	40.24	0.673

TABLE 7-3
STREAMTUBE PRESSURE AND ENTHALPY
AT SHOCK LAYER INTERCEPT

ψ Line No.	\bar{x}	P_0/P_{T0}	h/h_{T0}
Case # 1:	300 K-FT	$\alpha = 34^\circ$	$M_\infty = 30.2$
1	0.17	0.976	0.998
2	0.25	0.931	0.952
3	0.50	0.720	0.770
4	0.70	0.648	0.669
5	0.95	0.622	0.642
6	1.0	0.616	0.637
7	2.0	0.575	0.596
8	3.3	0.565	0.586
9	7.0	0.473	0.493
10	15.2	0.386	0.405
11	46.5	0.311	0.330
12	168.0	0.258	0.276
Case # 2:	254 K-FT	$\alpha = 34^\circ$	$M_\infty = 28$
1	0.17	0.9719	0.9968
2	0.25	0.881	0.907
3	0.50	0.715	0.739
4	0.70	0.644	0.667
5	0.95	0.615	0.639
6	1.0	0.613	0.636
7	2.0	0.571	0.594
8	3.3	0.5592	0.5826
9	7.0	0.4679	0.4909
10	15.2	0.3824	0.4047
11	46.5	0.3097	0.3279
12	168.0	0.2572	0.2754

ψ Line No.	\bar{x}	P_0/P_{T0}	h/h_{T0}
Case # 3:	238 K-FT	$\alpha = 33.3^\circ$	$M_\infty = 25.1$
1	0.17	0.9701	0.9960
2	0.25	0.9204	0.9545
3	0.50	0.7203	0.7463
4	0.70	0.6486	0.6745
5	0.95	0.6237	0.6496
6	1.0	0.6192	0.6452
7	2.0	0.5754	0.6011
8	3.3	0.5632	0.5891
9	7.0	0.4675	0.4927
10	15.2	0.3902	0.4133
11	46.5	0.3154	0.3364
12	168.0	0.2598	0.2793
Case # 4:	224 K-FT	$\alpha = 32.3^\circ$	$M_\infty = 22$
1	0.155	0.9675	0.9956
2	0.25	0.9257	0.9540
3	0.50	0.7137	0.7424
4	0.70	0.6254	0.6543
5	0.95	0.6092	0.6378
6	1.0	0.6044	0.6330
7	2.0	0.5680	0.5961
8	3.3	0.5573	0.5854
9	7.0	0.4720	0.4334
10	15.2	0.3837	0.4095
11	46.5	0.3141	0.3385
12	168.0	0.2619	0.2847

ψ Line No.	\bar{x}	P_0/P_{T0}	h/h_{T0}
Case # 5:	201 K-FT	$\alpha = 31.1^\circ$	$M_\infty = 17.9$
1	0.14	0.9609	0.9541
2	0.25	0.9217	0.9555
3	0.50	0.7170	0.7456
4	0.70	0.6197	0.6787
5	0.95	0.6117	0.6514
6	1.0	0.6071	0.6468
7	2.0	0.5588	0.5993
8	3.3	0.5452	0.5859
9	7.0	0.4676	0.5049
10	15.2	0.3896	0.4426
11	46.5	0.3122	0.3434
12	168.0	0.2572	0.2840
Case # 6:	181 K-FT	$\alpha = 30.2^\circ$	$M_\infty = 13.6$
1	0.14	0.9258	0.9916
2	0.25	0.9101	0.9475
3	0.50	0.7080	0.7429
4	0.70	0.6351	0.6696
5	0.95	0.6109	0.6457
6	1.0	0.6065	0.6412
7	2.0	0.5654	0.6006
8	3.3	0.5545	0.5896
9	7.0	0.4631	0.4332
10	15.2	0.3852	0.4224
11	46.5	0.3037	0.3417
12	168.0	0.2491	0.2872

7.4 CHEMICAL RELAXATION ALONG STREAMLINES

Using the pressure distributions given in Table 7-2, the initial conditions given in Table 7-3 and an initially undissociated gas; the streamtube code was used to determine the thermochemical state along the streamlines. The chemical reaction data given in Column 1 of Table 5.2 was used since the comparisons of Section 5 indicate this set to be the more reactive of the two examined, thus predicted heating rates should be conservatively high. Calculations were made for $t = 250, 400, 800,$ and 1400 seconds and typical results for $t = 800$ seconds are shown in Figures 7-13 through 7-17. The mass flow represented by each of the streamlines, was calculated from Table 7-1 and compared with the boundary layer flow rates shown in Figure 7-4. The 'match points' are shown in Figures 7-13 through 7-14 and therefore specify the boundary layer edge conditions at various locations on the body. Blending of these solutions with the viscous shock layer results (Section 7.2) was achieved by plotting shock layer entropy (at constant η) as a function of x and selecting the entropy which blended best with the predicted downstream boundary layer edge entropies. This is shown in Figure 7-13; then other variables enthalpy and mass fraction, are taken at this same value of η and compared with predicted downstream values. As shown in Figures 7-14 through 7-17, the transition from shock layer values to predicted downstream values is surprisingly good except in the case of NO mass fraction where due to an overshoot behavior, small changes in "matchpoint" location x can result in large changes in mass fraction. Similar results were obtained for the $t = 400$ and 1400 second cases; however a significant interpretation difficulty was noted in the $t = 250$ second case which is at a high altitude and therefore a low density. At these entry conditions, the shock layer is fully viscous so that the validity of a boundary layer analysis is questionable although shock layer solutions would still be valid. This question will be deferred to Section 7.6.

From the above procedure, edge values of entropy, enthalpy and specie mass fractions for $t = 400, 800$ and 1400 were obtained and are shown in Figures 7-18 through 7-22 as functions of the boundary layer coordinate, S . These were the distributions used in subsequent nonequilibrium boundary analyses.

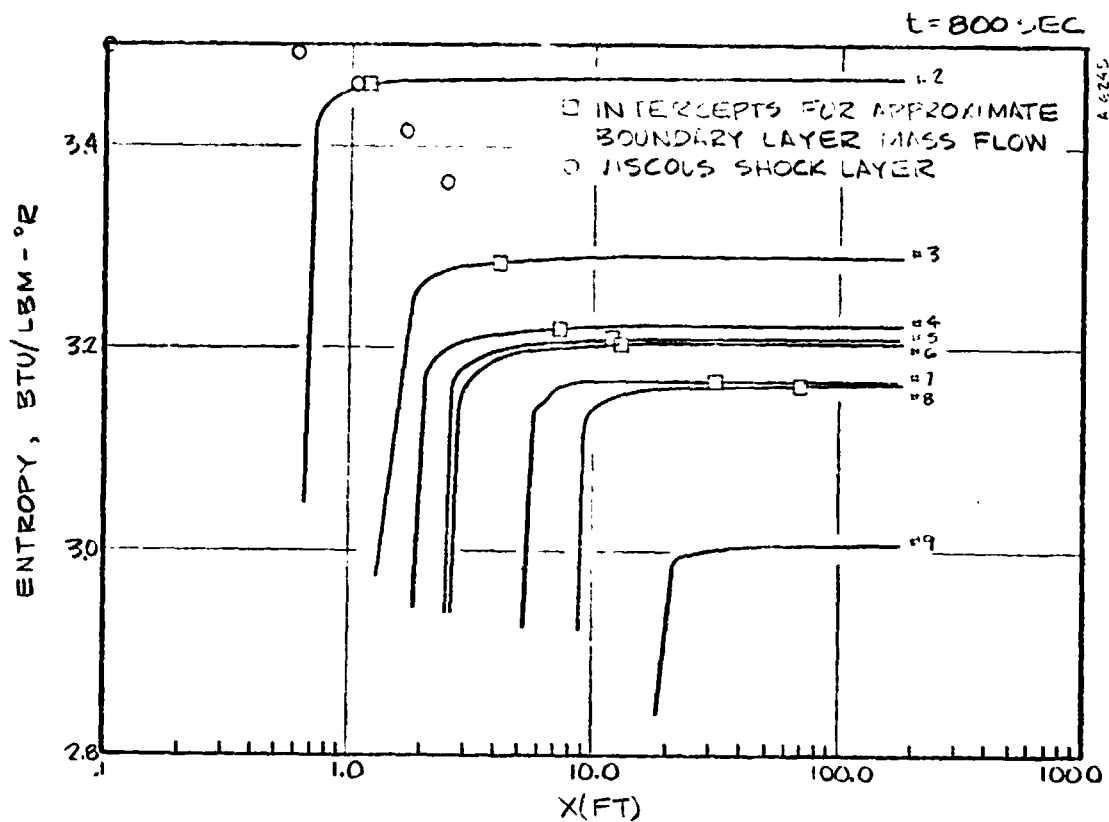


FIGURE 7-13 ESTIMATION OF EDGE ENTROPY, $t = 800 \text{ SEC}$

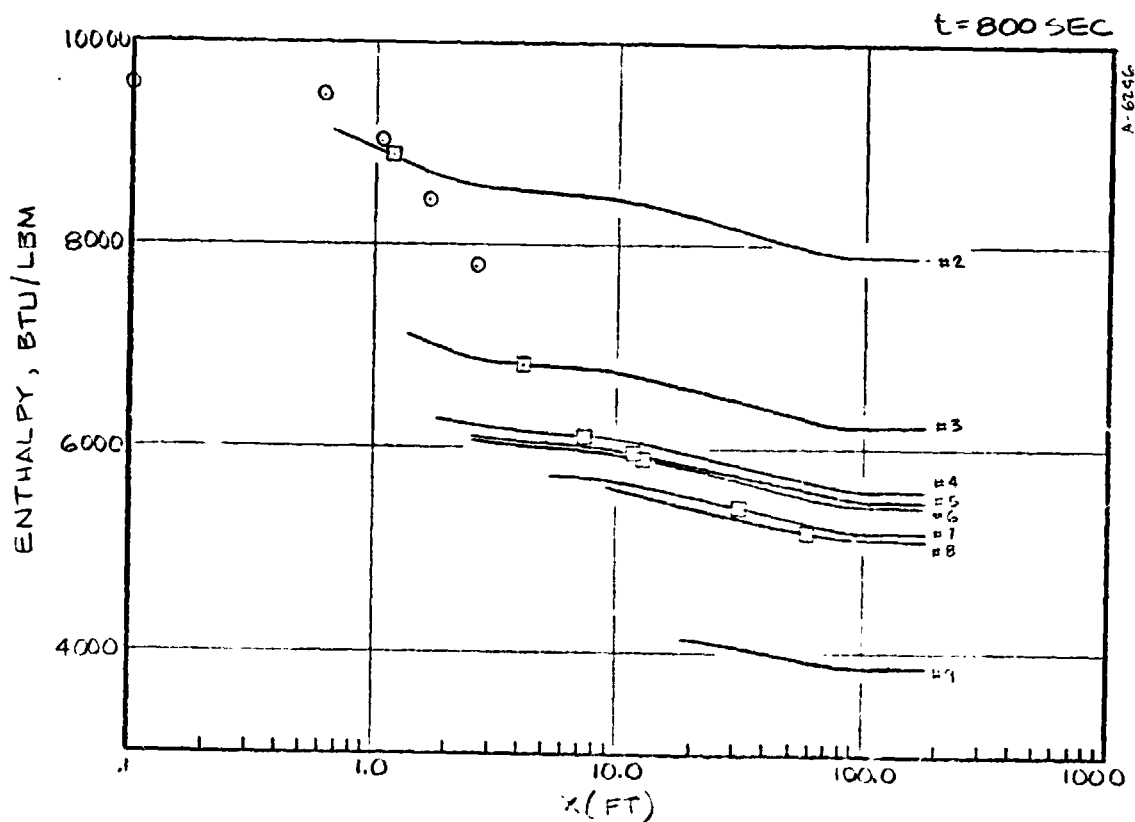


FIGURE 7-14 ESTIMATION OF EDGE ENTHALPY, $t = 800 \text{ SEC}$

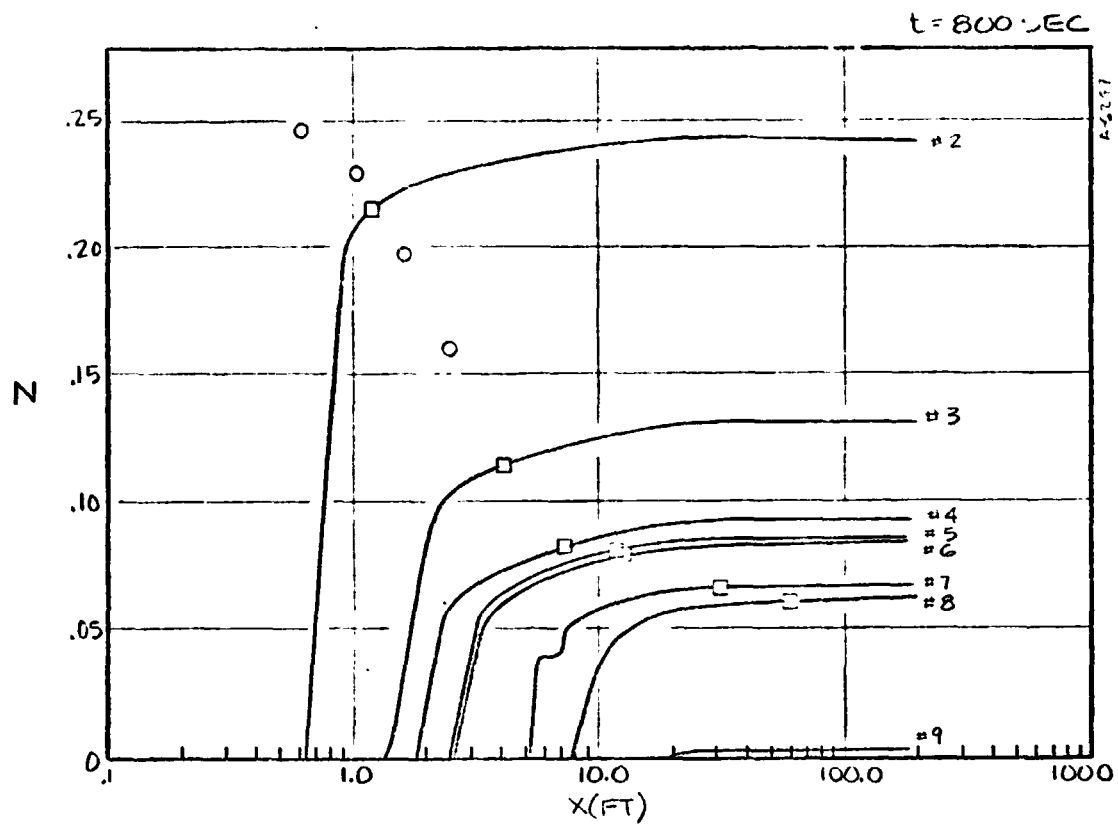


FIGURE 7-15 ESTIMATION OF EDGE N MASS FRACTION,
 $t = 800 \text{ SEC}$

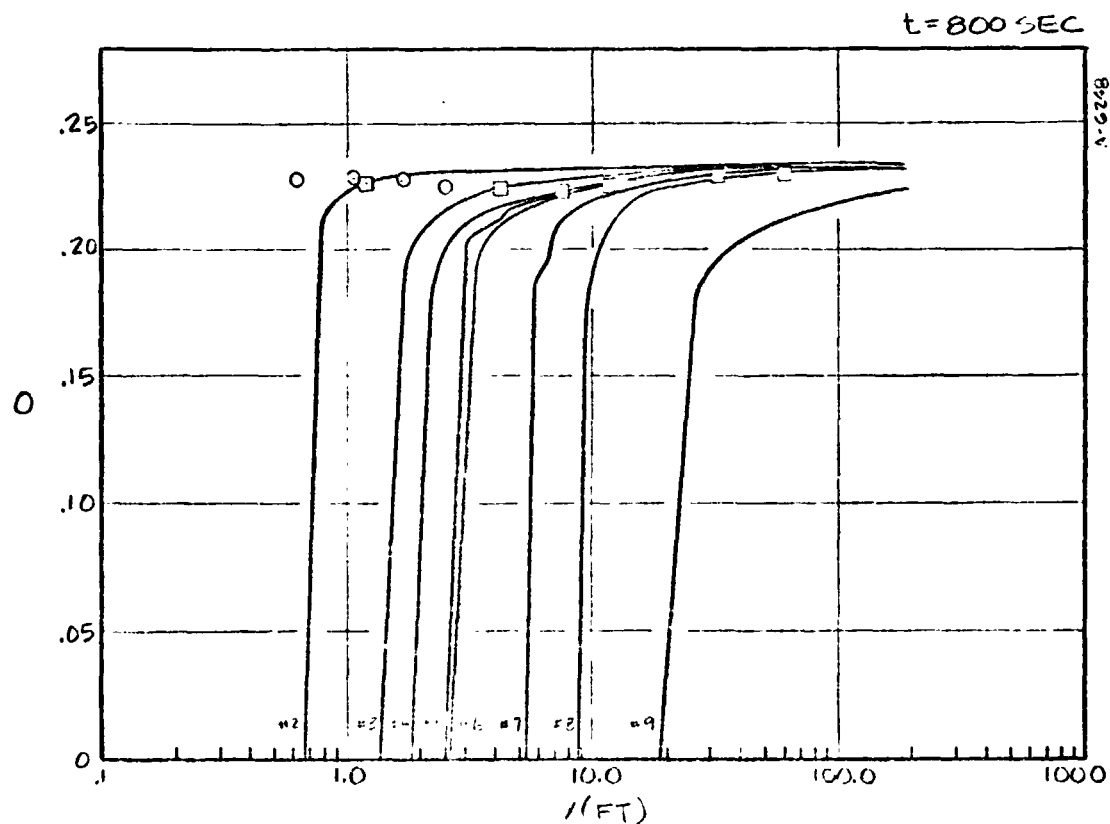


FIGURE 7-16 ESTIMATION OF EDGE O MASS FRACTION

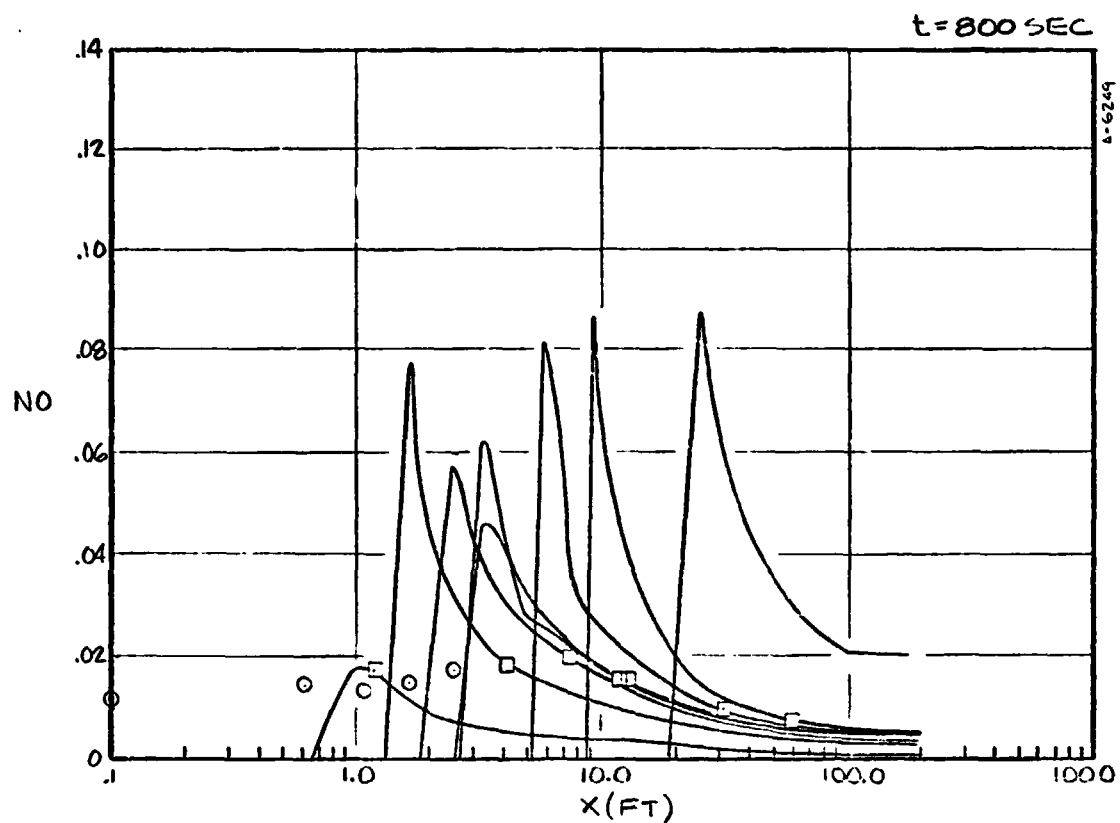


FIGURE 7-17 ESTIMATION OF EDGE NO MASS FRACTION,
 $t = 800 \text{ SEC}$

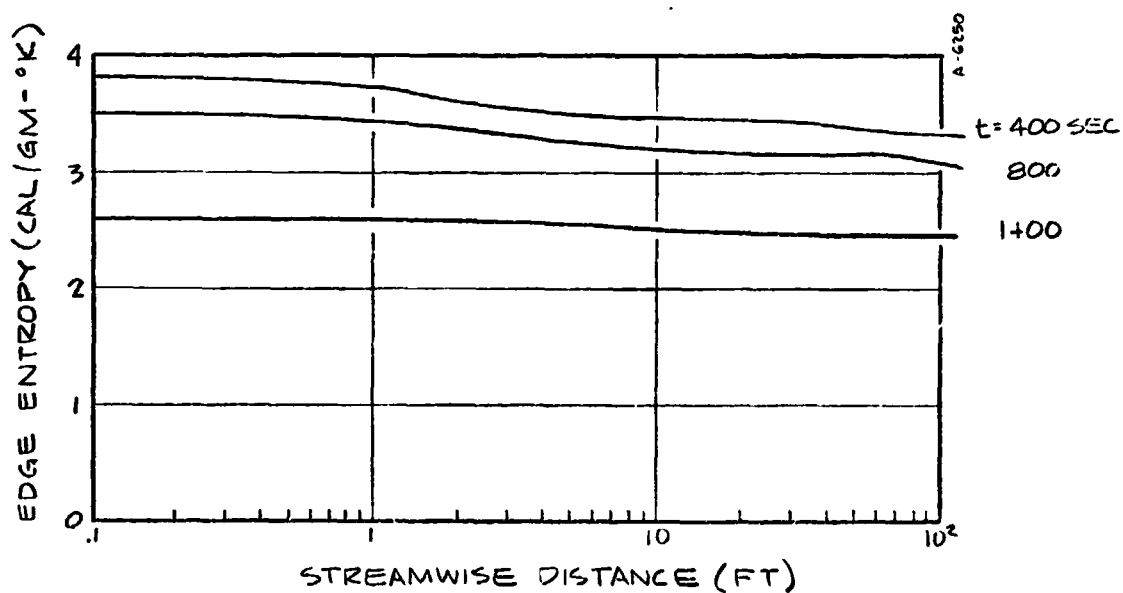


FIGURE 7-18 EDGE ENTROPY

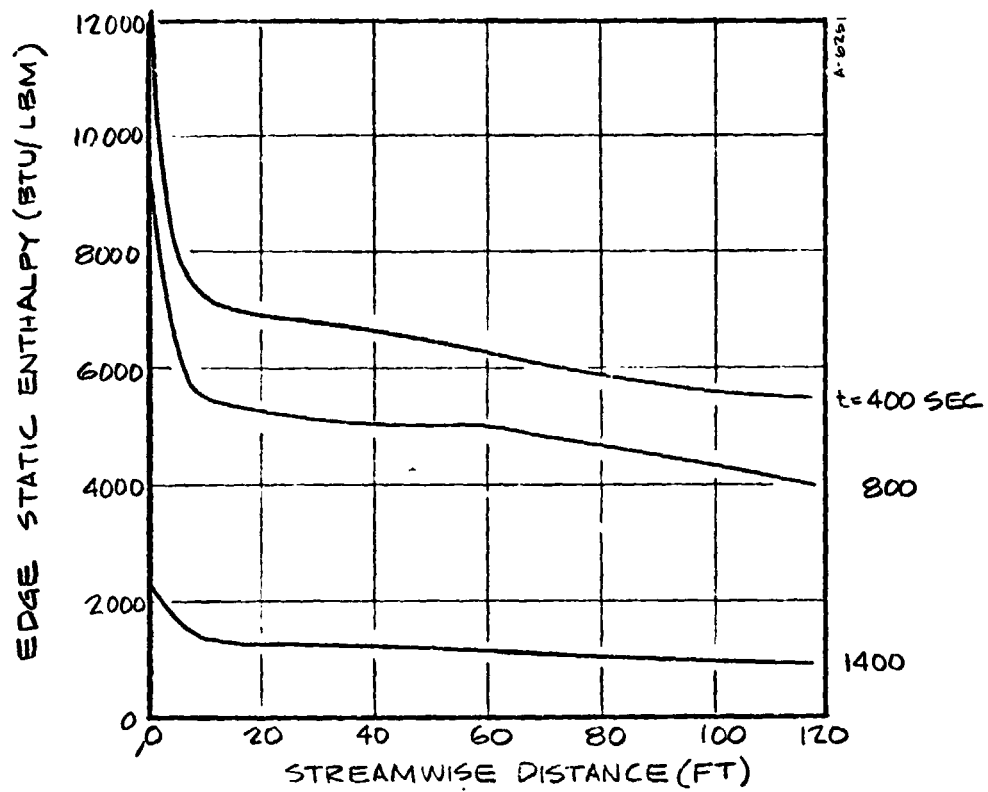


FIGURE 7-19 EDGE ENTHALPY

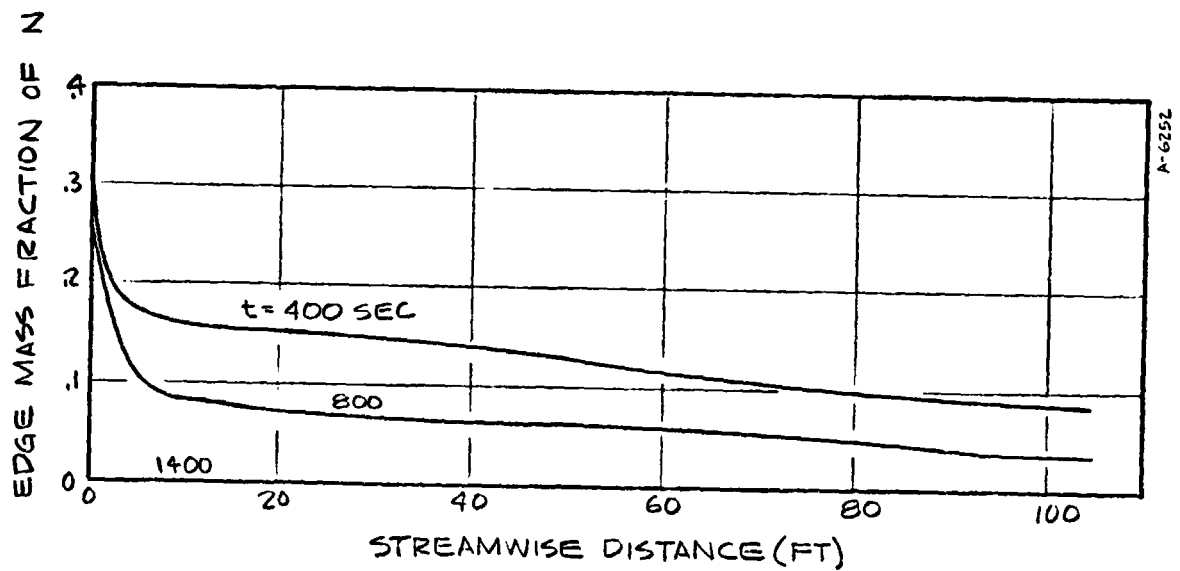


FIGURE 7-20 EDGE N MASS FRACTION

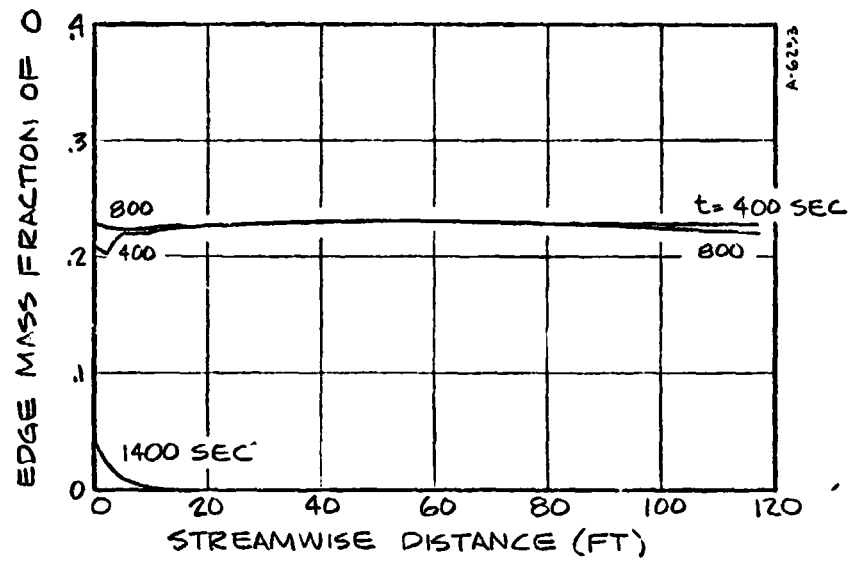


FIGURE 7-21 EDGE O MASS FRACTION

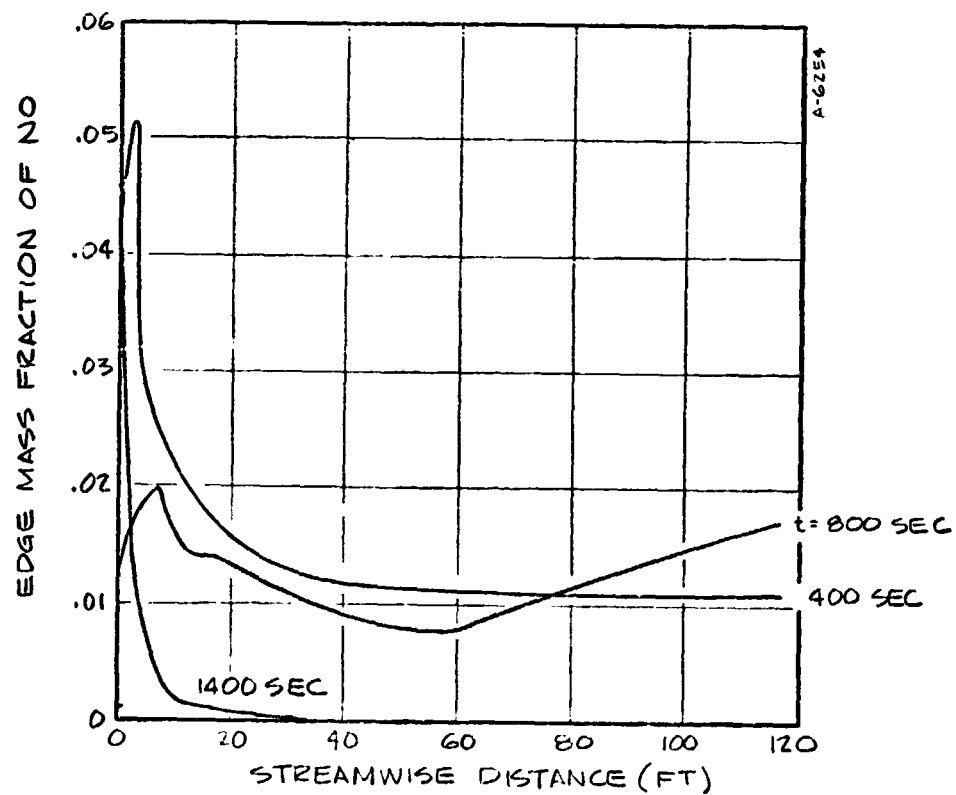


FIGURE 7-22 EDGE NO MASS FRACTION

7.5 HEAT TRANSFER ON SHUTTLE VEHICLE

Using the edge conditions given in Section 7.4 and the surface catalycities given in Section 5.6, nonequilibrium heat transfer rates to the pitch plane of the RI shuttle vehicle were calculated. The results are shown in Figure 7-23 along with the values predicted with equilibrium BLIMP and an isentropic edge expansion. Only the 400, 800 and 1200 second cases are shown since the question of the validity of boundary layer assumptions at the altitude corresponding to $t = 250$ seconds has not yet been resolved. The nonequilibrium assumptions are seen to reach a peak at a station slightly removed from the stagnation point whereas the equilibrium, isentropic edge solutions place peak heating at the stagnation point. This shift is due to entropy layer effects rather than chemistry effects as shown in Figure 7-24 where solutions using various assumptions are shown.

From Figure 7-23 it is seen that some small benefit is attained by the reduced catalycity at the stagnation point however there is an apparent penalty downstream. Again the discrepancy is due to entropy layer effects as shown in Figure 7-24 where nonequilibrium and equilibrium solutions with entropy layer are compared.

It appears from Figure 7-24 that the benefits of the slightly reduced catalycities derived in Section 5.6 have only small benefits however fully non-catalytic walls can reduce heating rates by 25 - 50% throughout the length of the vehicle.

One other possible anomaly appears in Figure 7-24. The semicatalytic and equilibrium entropy layer curves intersect at about $s = 45$ ft. and is mainly a chemistry effect. In the nonequilibrium case the boundary layer was close to frozen so that equilibrium assumptions would result in thicker boundary layers since homogeneous recombination behaves like a source. Thicker boundary layers result in reduced heat transfer which beyond $s \sim 45$ ft. is apparently greater than the effect of reduced surface recombination for the assumed surface catalycities.

The accuracy of the results shown in Figure 7-23 can be improved by iteration on the edge boundary conditions. The existing solution can be used as a better approximation to the boundary layer mass flow for matching to the inviscid solution. Note that, unless displacement effects are large (which would be the case at very high altitudes), the inviscid solutions do not change.

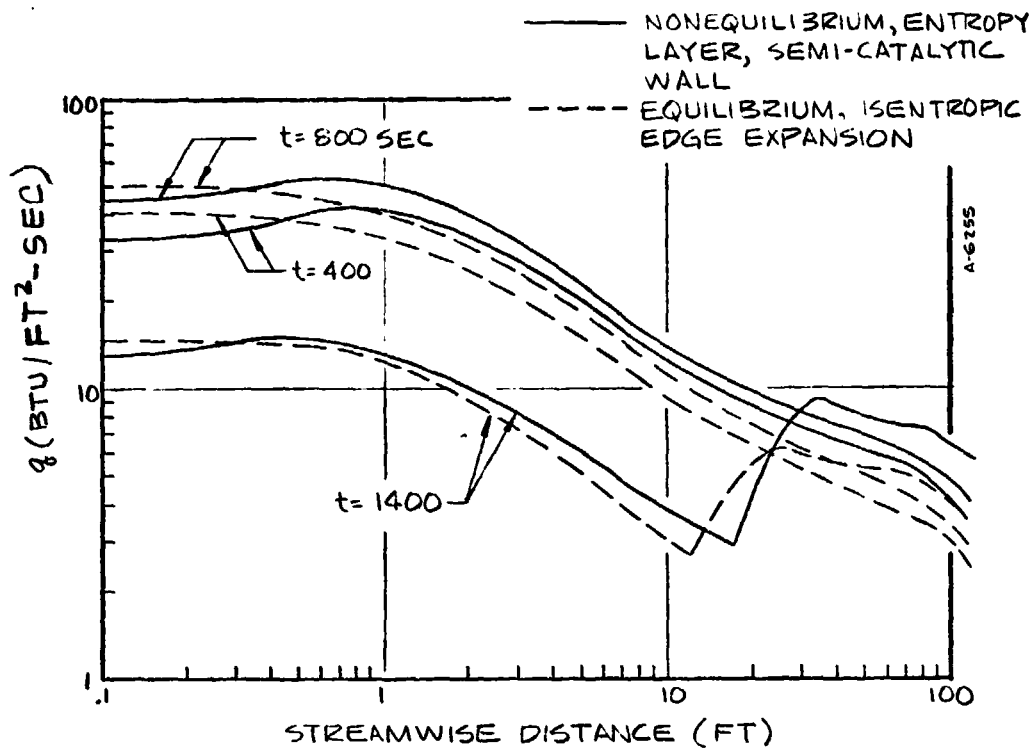


FIGURE 7-23 SHUTTLE HEATING RATES

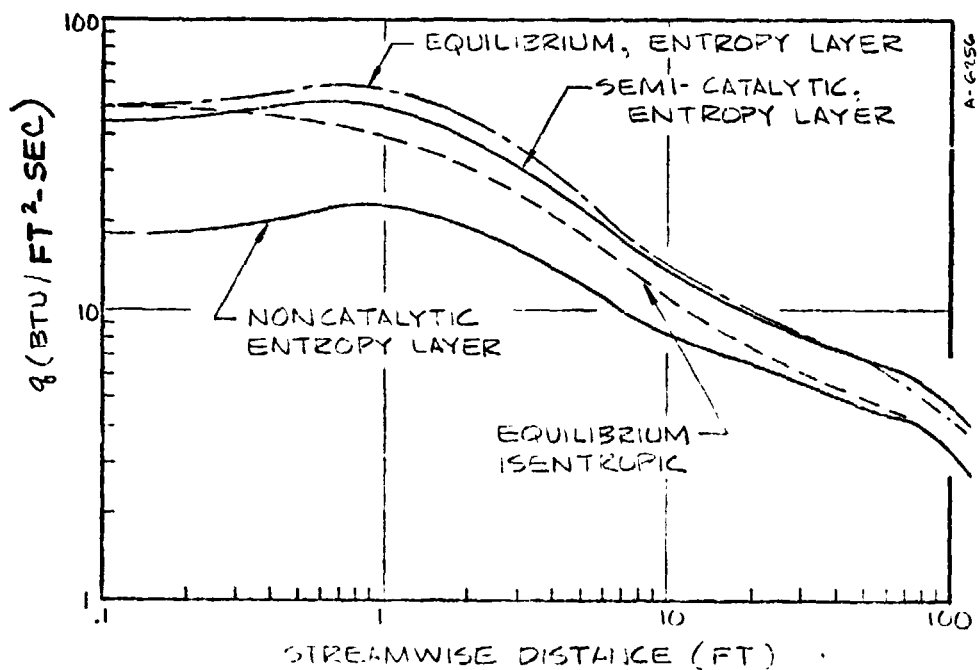


FIGURE 7-24 COMPARISON OF $t=800$ SECOND HEATING RATE PREDICTIONS

7.6 APPLICABILITY OF BOUNDARY LAYER ASSUMPTIONS AT LOW DENSITIES

The stagnation pressure for the $t = 250$ seconds case is an order of magnitude less than that at $t = 400$ seconds, namely 0.0014 compared to 0.018 atm. At $t = 400$ seconds a matching of shock layer and boundary layer solutions similar to that shown in Figure 7-13 through 7-17 was obtained even though the viscous zone occupied a significant portion of the shock layer. However, at $t = 250$ seconds, boundary layer predictions with BLIMP and BLIMP/KINET show a thickness greater than the predicted shock layer thickness. A comparison of shock layer and boundary layer solutions are shown in Figures 7-25, 7-26 and 7-27. Shock layer assumptions predict a stand-off distance of about 0.16 feet whereas various boundary conditions imposed on the boundary layer (see Figure 7-25) resulted in predicted boundary layer thicknesses between 0.2 and 0.45. Since this is not physically possible one must conclude that either the shock layer predictions or the boundary layer predictions are invalid. The latter is most likely since the predicted shock stand-off distances are in general agreement with the predictions of Reference 76 for a hypersonic density ratio of 1/10. Further, as shown in the shock layer curve in Figure 7-25, the influence of the wall extends throughout the shock layer; that is, there is no inviscid region. From Figure 7-27 it is apparent that the shock layer results cannot be approximated by frozen boundary layer edge conditions (curves A and D).

Although near the stagnation point, boundary layer assumptions are not valid, thin shock layer assumptions can lead to a better, though rigorously not completely valid, predictions. However downstream from this region the shock layer is not thin so that these predictions become invalid and still further downstream, conditions may be such that boundary layer assumptions are once again valid. Thus, although solutions can be obtained with boundary layer assumptions, one would be hesitant to place much confidence in them since initial conditions and boundary layer edge conditions cannot be adequately defined.

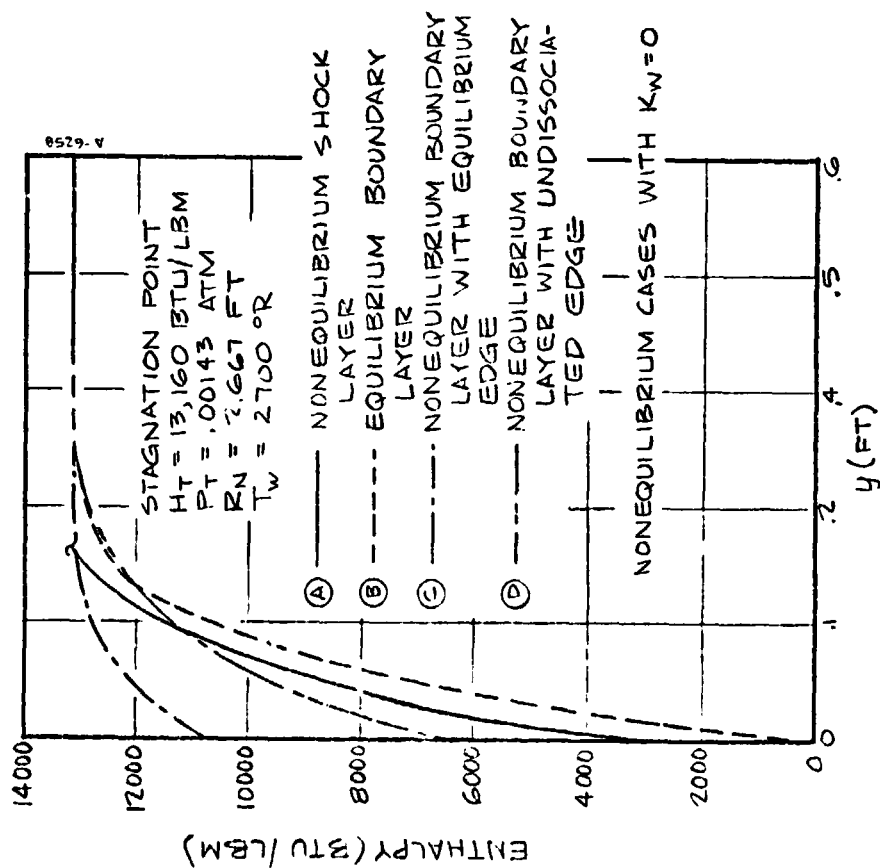


FIGURE 7-25 COMPARISON OF SHOCK AND BOUNDARY LAYER ENTHALPY FOR $t = 250 \text{ SEC}$

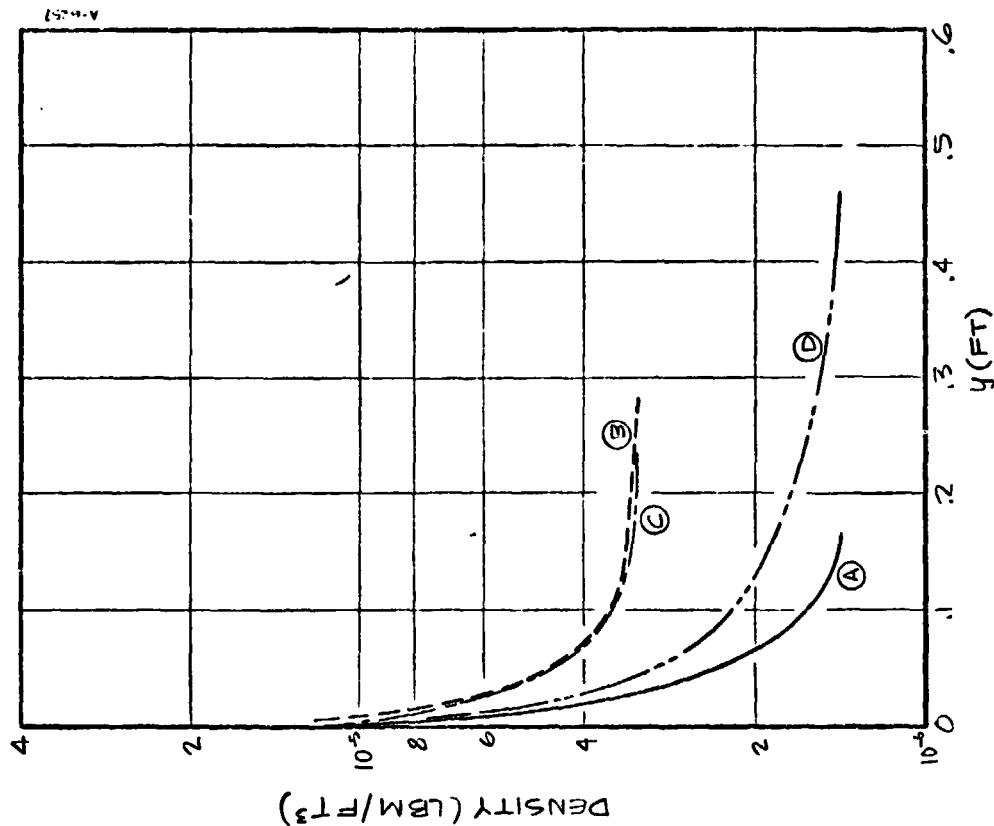


FIGURE 7-26 COMPARISON OF SHOCK AND BOUNDARY LAYER DENSITY FOR $t = 250 \text{ SEC}$

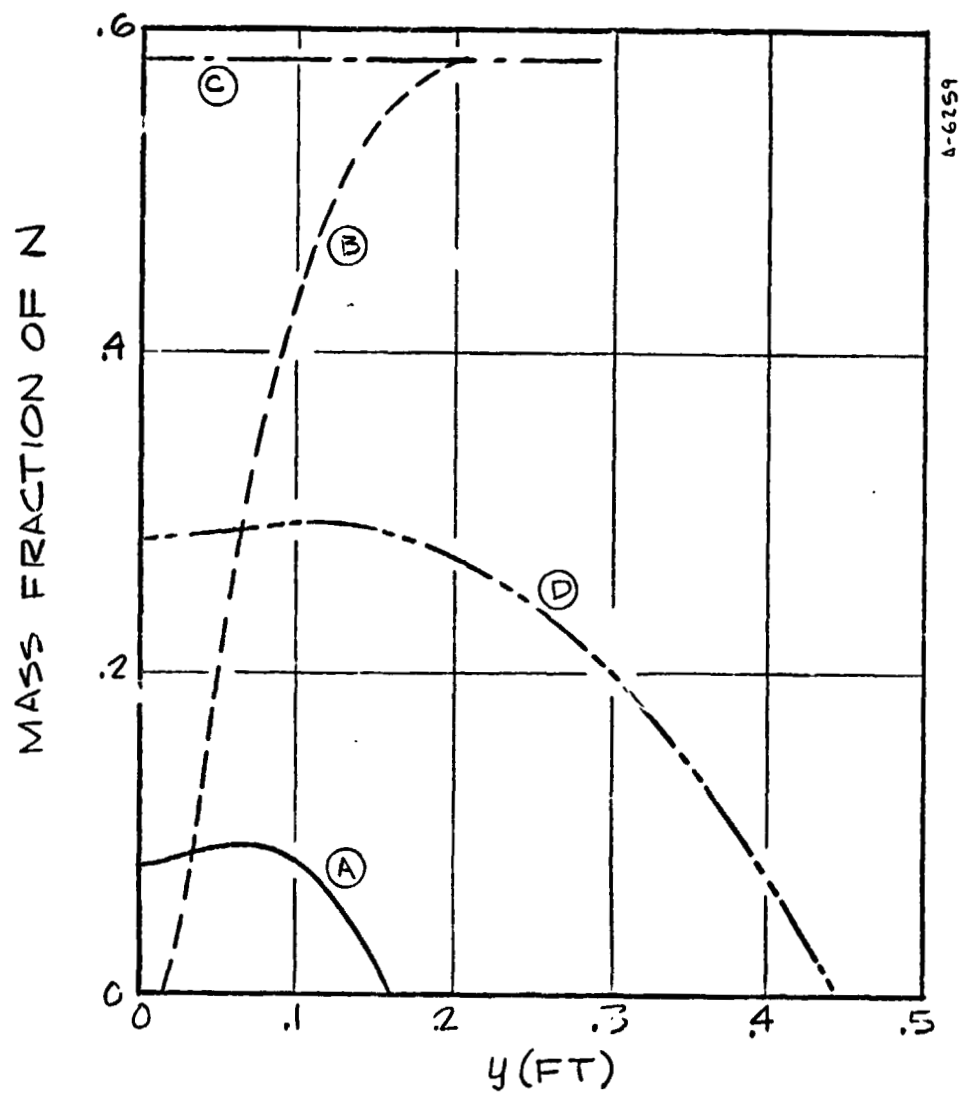


FIGURE 7-27 COMPARISON OF SHOCK AND BOUNDARY LAYER N MASS FRACTION FOR $t = 250$ SEC

SECTION 8

SUMMARY AND CONCLUSIONS

A nonequilibrium boundary layer code has been developed which retains all of the boundary condition generalities of the equilibrium BLIMP code. Both laminar and turbulent boundary layers are permitted however no attempts were made to resolve the question about the validity of standard chemical kinetics models in turbulent flows. The code BLIMP/KINET was used for extensive studies on the boundary layer and shock layer behavior in the stagnation region of both shuttle and RV size vehicles.

A procedure has been developed to approximate nonequilibrium and non-isentropic thermochemical states at the edge of a boundary layer on the pitch plane of typical shuttle vehicles.

The catalycity of typical shuttle TPS materials in dissociated air was estimated from a sampling of arc jet data. This data and the boundary layer edge conditions were used with the BLIMP/KINET code to calculate shuttle heating rates in laminar and turbulent flows. Some conclusions from this investigation are given below

- 1) The catalycity of typical TPS materials such as LI-900, LTV coated carbon-carbon and coated columbium is estimated to be about 1020 cm/second for O recombination and about 312 cm/second for N recombination at enthalpies between 2000 and 14000 Btu/lbm and pressure of about 0.01 atmospheres.
- 2) Entropy layer effects are essential whether equilibrium or nonequilibrium effects are considered.
- 3) Noncatalytic walls can reduce heating rates on the shuttle vehicle by 25 - 50% however, for the catalycities estimated from arc jet data only minimal nonequilibrium effects are predicted.

- 4) For the portion of the entry trajectory between $t = 250$ and $t = 1400$ seconds of pressure ratio, the distribution (P/P_∞) along streamlines is not sensitive to altitude, velocity and small angle of attack changes. These effects are implicit in the initial conditions behind the shock wave.
- 5) In most cases nonequilibrium chemistry calculations do not require any more nodal points than the comparable equilibrium calculations.

REFERENCES

1. Bartlett, E. P. and Kendall, R. M., "Nonsimilar Solution of the Multicomponent Laminar Boundary Layer by an Integral Matrix Method," Aerotherm Corporation Final Report 66-7, Part III, March 14, 1967 (also NASA CR 1062).
2. Anderson, L. W. and Kendall, R. M., "A Nonsimilar Solution For Multicomponent Reacting Laminar and Turbulent Boundary Layer Flows Including Transverse Curvature," AFWL TR-69-106, March 1970.
3. Bartlett, E. P., et al., "Further Studies of the Coupled Chemically Reacting Boundary Layer and Charring Ablator, Part I, Summary Report," Aerotherm Report No. 68-38, October 1968.
4. Kendall, R. M., "An Analysis of the Coupled Chemically Reacting Boundary Layer and Charring Ablator, Part V: A General Approach to the Thermochemical Solution of Mixed Equilibrium - Nonequilibrium, Homogeneous or Heterogeneous Systems," NASA CR-1064, June 1968; (also published as Aerotherm Report No. 66-7, Part V).
5. Bird, R. B.; Diffusion in Multicomponent Gas Mixtures. 25th Anniversary Congress Society of Chemical Engineers (Japan), Nov. 6-14, 1961. Published in abbreviated form in Kagaku Kogaku, Vol. 26, 1962, pp. 718-721.
6. Bartlett, E. P., Kendall, R. M., and Rindal, R. A., "A Unified Approximation for Mixture Transport Properties for Multicomponent Boundary Layer Applications," Aerotherm Corporation Final Report 66-7, Part IV, March 14, 1967 (also NASA CR 1063).
7. Reynolds, W. C., "A Morphology of the Prediction Methods," Proceedings of the 1968 AFSOR-IFP-Stanford Conference on Computation of Turbulent Boundary Layers, S. J. Kline, et al., editors, Stanford University, August, 1968.
8. Kendall, R. M., and Anderson, L. W., "Nonsimilar Solution of the Incompressible Turbulent Boundary Layer," Proceedings of the 1968 AFSOR-IFP-Stanford Conference on Computation of Turbulent Boundary Layers, S. J. Kline, et al., editors, Stanford University, August, 1968.
9. Clauser, F. H., "The Turbulent Boundary Layer," Advances in Applied Mechanics, IV, pp. 1-51, 1956.

REFERENCES (Continued)

10. Kendall, R. M., Rubesin, M. W., Dahm, T. J., and Mendenhall, M. R., Mass, Momentum, and Heat Transfer Within a Turbulent Boundary Layer With Foreign Gas Mass Transfer at the Surface, Part I - Constant Fluid Properties, Vidya Division, Itek Corporation, Final Report No. 111, 1964.
11. Mickley, H. S., Curl, R., Gessner, A., and Ginwala, K., Heat and Momentum Transfer for Flow Over a Flat Plate with Blowing and Main Stream Acceleration. MIT, Chemical Engineering Department, Report on Work Performed Under NACA Contract Naw 6228, February, 1955.
12. Kendall, R. M., Interaction of Mass and Momentum Transfer in the Turbulent Boundary Layer, Ph.D. Dissertation, M.I.T., 1959.
13. Adams, J. C. Jr., "Eddy Viscosity - Intermittency Factor Approach to Numerical Calculation of Transitional Heating on Sharp Cones in Hypersonic Flow," AEDC TR-70-210, November 1970.
14. Martellucci, A., Rie, H., and Sontowski, J. F., "Evaluation of Several Eddy Viscosity Models through Comparison with Measurements in Hypersonic Flows," AIAA Paper 69-688, June 1969.
15. Jaffe, N. A., Lind, R. C., and Smith, A. M. O., "Solution to the Binary Diffusion Laminar Boundary Layer Equations with Second Order Transverse Curvature," AIAA Journal, 5, pp. 1563-1569, September, 1967.
16. Bartlett, E. P., Abbett, M. J., Nicolet, W. E., and Moyer, C. B., Improved Heat-Shield Design Procedures for Manned Entry Systems, Part II, Application to Apollo, Aerotherm Corporation Final Report No. 70-15, Part II, June 22, 1970.
17. Denison, M. R., "Estimating Transient Temperature Distribution During Ablation," ARS Journal, 30, pp. 562-563, June, 1960.
18. Dorodnitsyn, A. A., "General Method of Integral Relations and Its Application to Boundary Layer Theory," Advances in Aeronautical Sciences, 3, Macmillan, New York, 1960.
19. Abramowitz, M., and Stegun, I., editors, Handbook of Mathematical Functions with Formulas, Graphs, and Mathematical Tables, National Bureau of Standards, Applied Mathematics Series, 55. U.S. Govt. Printing Office, Washington, 1964.
20. Garcia, F. Jr., Fowler, W. T. "Thermal Protection Optimization for the Space Shuttle," AIAA Paper No. 72-977.

REFERENCES (Continued)

21. Strouhal, G., and Curry, D. M., "TPS Trade Studies on Ablators and Reuseable Surface Insulation," NASA Space Shuttle Conference NASA-S-72-1388-S, April 1972.
22. Greenshields, D. H., Meyer, A. J., and Tillian, D. J., "Status of RSI TPS Technology Programs," NASA Space Shuttle Conference, NASA-S-72-1554-V, April 1972.
23. Pearce, B. E., "A Comparison of Simple Turbulent Heating Estimates and Boundary Layer Transition Criteria with Application to Large Lifting Entry Vehicles," NASA TMX 52876, Vol. 1 p. 484-507, July 1970.
24. Moore, J. D., "A Minimum Heating Flight Mode for High Lateral Range Space Shuttle Entries Including the Effects of Transition," NASA TM-X-52876, pp.531-546.
25. Young, C. H., Reda, D. C., and Roberge, A. M., "Hypersonic Transitional and Turbulent Flow Studies on a Lifting Entry Vehicle," AIAA Paper 71-100, January 1971, See also J. Spacecraft, Vol 9, No. 12 pp. 883-888, December 1972.
26. Masaki and Yakura, "Transitional Boundary Layer Considerations for the Heating Analyses of Lifting Reentry Vehicles, JSR Vol. 6 #9, September 1969, pp. 1048.
27. Hanner, O. M. Jr., and Schmitt, D. A., "A Review of Boundary Layer Transition with Emphasis Upon Space Shuttle Design Consideration," ASME paper 70-HT/SPT-18 June 1970.
28. Morkovin, M. V., "Critical Evaluation of Transition from Laminar to Turbulent Shear Layers with Emphasis on Hypersonic Traveling Bodies, AFFDL TR-68-149, March 1969.
29. Martellucci, A., Maguire, B. L., and Neff, R. S., "Analysis of Flight Test Transition and Turbulent Heating Data, Part I - Boundary Layer Transition Results," NASA CR 129045, November 1972.
30. Murphy, J. D., and Rubesin, M. D., "Re-evaluation of Heat Transfer Data Obtained in Flight Tests of Heat Sink Shielded Reentry Vehicle," Jour. Spacecrafts and Rockets, Vol. 3, p. 53-60 (1960).
31. Softley, E. J. Graber, B. C., and Zempel, R. E., "Experimental Observation of Transition of the Hypersonic Boundary Layer," AIAA 7, 2, p. 257-263, (February 1969).

REFERENCES (Continued)

32. Hamilton, H. H. and DeJarnette, F. R., "Inviscid Surface Streamline Program for Use in Predicting Shuttle Heating Rates," Space Shuttle Aerothermodynamics Technology Conference, December 1971.
33. Fischer, M. C., "An Experimental Investigation of Boundary Layer Transition on a 10° Half-Angle Cone at Mach 6.9, NASA TND-5766, April 1970.
34. Maddalon, D. V., and Henderson, A. Jr., "Boundary - Layer Transition on Sharp Cones at Hypersonic Mach Numbers," AIAA J. 6, 3, p. 424-431 (March 1968).
35. Masek, R. V., "Boundary Layer Transition on Lifting Entry Vehicle Configuration at High Angles of Attack," NASA TMX-52876 Vol. 1, p. 445-462, (July 1970).
36. "Definition of LORN Boundary Layer Transition Criterion," Philco-Ford Inc. DR-4517, Newport Beach, California.
37. Wood, B. J., and Wise, H., "The Kinetics of Hydrogen Atom Recombination on Pyrex Glass and Fused Quartz," SRI Squid Report.
38. Wise, H. and Wood, B. J. "Energy Transfer During Atom Recombination on Solid Surfaces," 3rd Symposium on Rarefied Gas Dynamics.
39. Gurney, J. P., "General Formulation of Surface Catalytic Reactions," AIAA Journal, Vol. 4, No. 7, pp. 1299-1300, July 1966.
40. Goulard, R., "On Catalytic Recombination Rates in Hypersonic Stagnation Heat Transfer," Jet Propulsion, Vol. 28, No. 11, pp. 737-745, November 1958.
41. Bortner, M. H., "Chemical Kinetics in a Reentry Flow Field," General Electric Report R-63-SD-63, August 1963.
42. Frey, H. M., Nickerson, G. R., and Tyson, T. J., "ODKS One-Dimensional Kinetic Reference Program," Dynamic Science, September 1970.
43. Bortner, M. H., "Suggested Standard Chemical Kinetics for Flow Field Calculations - A Consensus Opinion," AMRAC Proceedings, Vol. 14, Part 1, 1966.
44. Tunder, R., et al., "Compilation of Reaction Rate Data for Nonequilibrium Performance and Reentry Calculation Programs," Aerospace Corp. Report No. TR-1001 (9210-02)-1.
45. Dryer, F., et al., "Temperature Dependence of the Reaction $\text{CO} + \text{OH} \rightarrow \text{CO}_2 + \text{H}$," Combustion and Flame Vol. 17, pp. 270-272, 1971.
46. Newhall, H. K., "Kinetics of Engine - Generated Nitrogen Oxides and Carbon Monoxide," Combustion Institute 12th Symp (intl) on Combustion, pp. 603-613, 1969.

REFERENCES (Continued)

47. Wray, K. L., "Kinetics of O_2 Dissociation and Recombination," Combustion Institute, 10th Symp (Intl) on Combustion pp. 523-537, 1964.
48. Browne, W. G., White, D. R., and Smookler, G. R., "A Study of the Chemical Kinetics of Shock Heated $H_2/CO/C_2$ Mixtures," Combustion Inst. 12th Symp (Intl) on Combustion pp. 557-567, 1969.
49. Sulzmann, K. G. P., Leibowitz, L., and Penner, S. S., "Shock Tube Studies on Mixtures of NO, CO and Ar," Combustion Inst. 13th Symp (Intl) on Combustion pp. 137-145, 1970.
50. Shahed, S. M., and Newhall, H. K., "Kinetics of Nitric Oxide Formation in Propane - Air and Hydrogen - Air - Diluent Flames," Combustion and Flames Vol. 17, No. 2, pp. 131-137, October 1971.
51. Newhall, H. K., and Shahed, S. M., "Kinetics of Nitric Oxide Fomation in High Pressure Flames," Combustion Inst. 13th Symp (Intl.) pp. 381-389, 1970.
52. Wray, K. L., Feldman, E. V., and Lewis, P. F., "Shock Tube Study of the Effect of Vibrational Energy of N_2 on the Kinetics of the $O + N_2 \rightarrow NO + N$ Reaction," J. Chem. Phys. Vol. 53, p 4131, 1970.
53. Wray, K. L., and Teare, J. D., "Shock Tube Study of the Kinetics of Nitric Oxide at High Temperatures," J. Chem. Phys. Vol. 36, p. 2582, 1962.
54. Wray, K. L., "Chemical Kinetics in High Temperature Air," ARS Progress in Astronautics and Rocketry: Hypersonic Flow Research Ed. - F.R. Riddell, Vol. 7 pp. 181-204, Academic Press New York, 1962.
55. Lin, S. C., Teare, J. D., "Rate of Ionization Behind SHock Waves in Air II Theoretical Interpretations," Phys. Fluid Vol. 6, pp. 355 - 375, March 1963.
56. Clark, T. C. Garnett, S. H., and Kistiahowsky, G. B., "Reaction of Carbon Dioxide with Atomic Oxygen and the Dissociation of Carbon Dioxide in Shock Waves," J. Chem. Phys. Vol. 51, p 2885, 1969.
57. Brokaw, R. S., "Ignition Kinetics of the Carbon Monoxide - Oxygen Reaction," Combustion Inst. 11th Symp (Intl) on Combustion pp. 1063-1073, 1966.
58. Brabbs, T. A., Belles, F. E., and Brokaw, R. S., "Shock Tube Measurements of Specific Reaction Rates in the Branched - Chain $H_2 - CO - O_2$ System," Combustion Inst. 13th Symp (Intl) on Combustion pp. 129-136, 1970.
59. Bauer, S. H., et al., "Reaction Between CO and SO_2 at Elevated Temperatures A Shock - Tube Investigation," Combustion Inst. 13th Symp (Intl) on Combustion pp. 417-425, 1970.

REFERENCES (Continued)

60. Breen, B. P., et al., "Combustion Control for Elimination of Nitric Oxide Emissions from Fossil - Fuel Power Plants," Combustion Inst. 13th Symp (Intl) on Combustion pp. 391-401, 1970.
61. Blottner, F. G., Johnson, M., and Ellis, M., "Chemically Reacting Viscous Flow Program for Multicomponent Gas Mixtures," Sandia Laboratories Report SC-RR-70-754, December 1971.
62. Schaefer, J. W., "Thermal Screening of Shuttle Orbiter Vehicle TPS Materials Under Convective Heating Conditions," Aerotherm Division, Acurex Corporation, Final Report No. 72-56, Prepared for NASA Under Contract NAS2-6445, August 1972 (to be published as a NASA High Number CR). See also, Schaefer, J. W., et al., "Thermal Evaluation of Selected Shuttle Vehicle TPS Materials," Aerotherm Division, Acurex Corporation Final Report prepared for NASA under Contract NAS2-6600 (to be published as a NASA High Number CR).
63. Witliff, C. E., Curtiss, J. T., "Normal Shock Wave Parameters In Equilibrium Air," Cornell Aero Laboratory Report CAL-111, November 1961, (1959 ARDC Model Atmosphere).
64. Swigart, R. J., "Hypersonic Blunt Body Flow Fields at Angle of Attack," Lockheed Palo Alto Research Laboratory Report and Fluid Mechanics No. 5, May 1963.
65. Bartlett, E. P., Morse, H. L., Tong, H., "Investigation of Thermal Protection Systems Effects on Viscid and Inviscid Flow Fields for Manned Entry Systems," Aerotherm Report No. 71-38, September 22, 1971. (NASA Contract NAS9-9494).
66. Marvin, J. G., et al., "Surface Flow Patterns and Aerodynamic Heating on Space Shuttle Vehicles," J. Spacecraft (9) August 8, 1972.
67. Rakich, J. V., Kutler, P., "Comparison of Characteristics and Shock Capturing Methods with Application to the Space Shuttle Vehicle," AIAA 10th Aerospace Sciences Meeting, Paper No. 72-191, San Diego, California, January 17, 19, 1972.
68. Kaattari, G. E., "Shock Envelopes of Blunt Bodies at Large Angles of Attack," NASA TN D-1980, 1963.
69. Hoshizaki, H., "Convective and Radiative Heat Transfer to Blunt Bodies at Angle of Attack," Lockheed Palo Alto Research Laboratory Report 4-06-66-11, July 1966, (NASA Contract NAS 7-386).

REFERENCES (Concluded)

70. Buckingham, A. C., Hoshizaki, H., Lasher, L. E., "Study of Superorbital Heating Problems, Part 2," Lockheed Palo Alto Research Laboratory Interim Report, December, 1965 (NASA Contract NAS 7-386).
71. Webb, H. G., Dresser, H. S., Adler, B. K., Waiter, S. A., "Inverse Solution of Blunt Body Flow Fields at Large Angles of Attack," AIAA Journal (5) 6, June 1967.
72. Buckingham, A. C., Hoshizaki, H., "Coupled Convective and Radiative Heating to Superorbital Entry Vehicles," Lockheed Palo Alto Research Laboratory Report 4-43-65-1, October, 1965 (NASA Contract NAS 7-295).
73. Buckingham, A. C., "A Real Gas Method of Characteristics Program," Douglas Aircraft Co. Santa Monica Division Report SM 38078, December 15, 1960.
74. Maslen, S. H., Moeckel, W. E., "Inviscid Hypersonic Flow Past Blunt Bodies," IAS Journal (), 1957.
75. Hearne, L. F., Chinn, J., Woodruff, W., "Study of Aerothermodynamic Phenomena Associated with Reentry of Manned Spacecraft, Lockheed Missiles and Space Co. Report Y-78-66-1, May 1966, (NASA Contract NAS 9-3531).
76. Chester, W., "Supersonic Flow Past a Bluff Body with a Detached Shock, Part II, Axisymmetric Body," J. Fluid Mech., Vol. 1, pp. 353-365, 1956.

APPENDIX A

INPUT DATA FOR SURFACE CATALYZED REACTIONS

Surface reaction rates are calculated as if heterogeneous chemistry were of the same form as homogeneous chemistry, i.e., for the recombination of oxygen atoms, the net surface reaction is



The molar production rate is then

$$(\dot{M}_O) = k_f (p_O^2 - \frac{1}{K_p} p_{O_2}) \quad (A-2)$$

The term p_{O_2}/K_p will be small for nonequilibrium conditions so that

$$(\dot{M}_O) \approx k_f (p_O^2) \quad (A-3)$$

This relationship indicates that the catalysis reaction is second order due to the form of Equation (A-1). However there is some evidence that the reaction is first order or possibly something intermediate since catalysis is not really a one step reaction. Any reaction order can be approximated by rewriting Equation (A-1). For instance, to specify surface recombination as a first order reaction, one can write



Then Equation (A-3) becomes

$$(\dot{M}_O) \approx k_f (p_O) \left(\frac{\text{lb-moles}}{\text{ft}^2 \text{sec}} \right) \quad (A-5)$$

In order to express k_f in terms of surface catalycity, one can write

$$\frac{\rho_w k_w (SP_i)_w}{\bar{m}_i} = \frac{\dot{m}_w}{\bar{m}_i} = (\dot{M}_i) \left(\frac{\text{lb-moles}}{\text{ft}^2 \text{sec}} \right) \quad (\text{A-6})$$

For perfect gases

$$\rho_w (SP_i)_w = \frac{p_i \bar{m}_i}{RT} \quad (\text{A-7})$$

so that

$$k_f \frac{\rho_w (SP_i)_w RT}{\bar{m}_i} = \frac{\rho_w k_w (SP_i)_w}{\bar{m}_i}$$

$$k_f = \frac{k_w}{RT} \frac{\text{lb-moles}}{\text{ft}^2 \text{sec-atm}} \quad (\text{A-8})$$

Thus for the first order reaction (A-4), k_w and k_f are related by

$$k_f = (0.025 k_w) \frac{1}{T}$$

where T ($^{\circ}\text{K}$) and k_w (cm/sec). In terms of input variable

$$\text{FKF} = 0.025 k_w$$

$$\text{POW} = -1.0$$

$$\text{EAK} = 0.0$$

Similar relationships could be obtained for other reaction orders. Note that in the above formulation a dependence of k_w on temperature could be accounted for in the form of

$$\frac{k_w}{k_{w_{\text{ref}}}} = T^n e^{(-E/RT)}$$

where $k_{w_{\text{ref}}}$ is some reference value. Then

$$\text{FKF} = 0.025 k_{w_{\text{ref}}}$$

$$\text{POW} = -1.0 + n$$

$$\text{EAK} = E$$